

ALMA MATER STUDIORUM  
UNIVERSITÀ DEGLI STUDI DI BOLOGNA  
Facoltà di Scienze Matematiche Fisiche e Naturali  
Dottorato di Ricerca Geofisica XXII Ciclo  
Settore Scientifico-Disciplinare GEO/10

# Velocity structure and seismic anisotropy in the crust and upper mantle from Receiver Function analysis: three case studies in Italy.

PhD Thesis of:

**Dott. Irene Bianchi**

Tutor:

**Dott. F. P. Lucente**

Coordinator:

**Prof. M. Dragoni**

---

---

# CONTENTS

<b>1</b>	<b>Introduction</b>	<b>1</b>
<b>2</b>	<b>Deep Structure of the Colli Albani volcanic district (central Italy) from Receiver Functions analysis.</b>	<b>5</b>
2.1	Introduction . . . . .	5
2.2	Crustal structure . . . . .	7
2.3	Data & Method . . . . .	8
2.3.1	Dipping layer vs anisotropy with a dipping symmetry axis	9
2.4	Inversion Method . . . . .	9
2.4.1	Parameter space . . . . .	11
2.4.2	Sensitivity to 3D parameters . . . . .	13
2.4.3	Errors on layer thickness . . . . .	17
2.5	Results . . . . .	17
2.6	Discussion . . . . .	28
2.7	Conclusions . . . . .	32
<b>3</b>	<b>Mapping seismic anisotropy using harmonic decomposition of Receiver Functions: an application to Northern Apennines, Italy.</b>	<b>33</b>
3.1	Introduction . . . . .	34
3.2	Data & Method . . . . .	36
3.2.1	CCP and Migration . . . . .	38
3.2.2	Harmonic analysis . . . . .	39
3.2.3	Symmetry directions . . . . .	40
3.2.4	Modeling . . . . .	42
3.3	Results . . . . .	42
3.3.1	Harmonic analysis . . . . .	42
3.3.2	Symmetry direction . . . . .	49
3.3.3	Modeling . . . . .	51
3.4	Discussion . . . . .	52
3.5	Conclusion . . . . .	56
3.6	Supporting material . . . . .	57

---

3.6.1	Migration . . . . .	57
3.6.2	Decomposition of the seismic signal . . . . .	57
<b>4</b>	<b>Custal thickness variations and seismic anisotropy in Southern Apennines (Italy) from receiver functions.</b>	<b>61</b>
4.1	Introduction . . . . .	61
4.2	Data and method . . . . .	62
4.3	Forward modeling . . . . .	64
4.4	Results . . . . .	65
4.5	Discussions . . . . .	70
4.6	Conclusions . . . . .	74
<b>5</b>	<b>The 2009 L'Aquila (central Italy) earthquake rupture controlled by a high Vs barrier: a Receiver Function application</b>	<b>79</b>
5.1	Introduction . . . . .	79
5.2	Data & Method . . . . .	80
5.3	Results . . . . .	84
5.3.1	AQU . . . . .	84
5.3.2	FAGN . . . . .	88
5.4	Discussions . . . . .	91
5.4.1	Regional structure of the crust . . . . .	92
5.4.2	Seismogenetic layer . . . . .	92
5.5	Conclusions . . . . .	95

## Introduction

The most heterogeneous layer of the Earth is the outer one, the crust. Here, chemical composition, rocks texture and physical properties can be highly variable in all directions, making the one-dimensional approximations, as function of depth only, extremely rough. The high grade of heterogeneity of the Earth's crust makes the determination of its principal characteristic (composition, structure, geometry) a difficult task to achieve. This is especially true for the deeper part of the crust, which is not directly accessible, and whose characteristics should be investigated through indirect information. Seismology is possibly the main source of information on the deep Earth, hence on the Earth's crust. In the last years, the developing of new techniques of analysis and the growing amount of seismological data and studies allowed to gain a better knowledge of the Earth's interior. These studies revealed that the Earth is highly three-dimensional and mainly anisotropic, and these complexities heighten in the crust. In this PhD Thesis we aim to study the crustal structure in various tectonic environments in Italy by means a seismological approach. The Italian territory is shaped by the geodynamic evolution of the Apennines-Tyrrhenian subduction system. Evidence of lithosphere subduction during the Neogene formation of the Apenninic belt comes from geological, petrologic, and seismological studies (*Faccenna et al.*, 2001, and references therein). The present-day geologic setting of the Italian peninsula is complex due to the interaction of different geodynamic processes still acting. Italy is located between the African and the European plates, which are presently converging approximately in a NS direction at a rate of less than 1 cm/year (*Argus et al.*, 1989; *Dewey et al.*, 1989). The present configuration of the Apennines consists of two major arcs, the northern Apennines and the Calabrian arc, separated, in central-southern Apennines, by a NS trending fault zone that, according to some authors is related to deep lithospheric discontinuity (*Patacca & Scandone*, 1989; *Amato et al.*, 1993; *Lucente et al.*, 1999). It is widely accepted that the southern Tyrrhenian Sea formed as a back-arc basin related to the subduction of the Ionian lithosphere beneath the Calabrian arc (*Malinverno & Ryan*, 1986). The

northern Apenninic arc developed with a series of thrusting episodes over the Adriatic continental plate, which flexed below the foredeep for as much as 8 km since Pliocene (*Royden et al.*, 1987). The presence of subcrustal seismicity down to 90 km depth (*Selvaggi & Amato*, 1992) suggests that the arc has developed due to westward subduction of the Adriatic plate. In the northern Apennines, from Upper Miocene to Quaternary the coexistence of extension in the internal domain toward the Tyrrhenian, and compression along the external part of the arc, toward the Adriatic, is observed (*Patacca & Scandone*, 1989; *Frepoli & Amato*, 1997). Quaternary caldera complexes grown in the back-arc region of the northern Apennines and central Italy. The Central and Southern Apennines developed in a transition area linking the Northern Apennines and the Calabrian subduction arcs; together they made up the whole Apennine fold-and-thrust belt. From north to south, the Apennines are made of sedimentary rocks mainly derived from the Mesozoic deposits of the southern passive margin of the Tethys Ocean, characterized by extensive outcrops of Apenninic Platform carbonate rocks and related transitional facies of pelagic Basin to the north and east. Being locus of very active tectonic processes, the internal structure of the crust in the Italian region is extremely complex. We focus our study on the determination of the main geometric and structural characteristic of some of these crustal complexities. To do it we apply a well know geophysical technique developed to identify the main impedance contrasts in the structure under the seismic station, which uses the analysis of the Receiver Functions (*Langston*, 1979). These are time series obtained by the teleseismic recordings under a three component seismic station, and recovered thanks to two simple assumptions: that energy from a P-wave which crosses a seismic discontinuity is partially converted into a S-wave, and that for teleseismic P-waves, source and path effects are recorded on the vertical component. Through the deconvolution of the horizontal components from the vertical one of the seismic record, we obtain two times series, Radial and Transverse, which contain the P-to-S phases converted at the interfaces under the receiver. In a receiver function the local structure response is separated by all other factors which interact to compose a seismogram, the information is then translated into a simple model of local velocity structure. We analyzed and modeled the computed receiver functions to generate S-velocity models of the crust and upper mantle in various study regions, in Italy. We often find and model not only one-dimensional structures below the stations, but more often our results evidence the presence of crustal complexities, such as dipping interfaces and anisotropic layers. In particular, the determination of the anisotropic properties of rocks both in the crust and in the mantle can be highly informative on their tectonic history and on the stress regime acting. The tectonic processes that we observe in nature impose stresses and shear on the Earth outermost layers, these forces deform the crust and mantle, modifying their internal structure, and reorganizing the texture of rocks. This can cause differential propagation of the seismic waves inside the Earth's interior, i.e. the seismic anisotropy. The mechanisms that are used to explain anisotropy in the crust and the mantle are usually classified in two main groups: shape-preferred orientation (SPO) and lattice-preferred orientation (LPO) of Earth materials (e.g. *Fouch & Rondenay*, 2006). In the

---

Earth's crust the development of anisotropy is generally ascribed to SPO related to structural features as faults, regularly oriented cracks or layering, or due to elongated or flat minerals alignment, that provide a preferential fast and slow direction of seismic wave propagation. In the upper mantle, seismic anisotropy is usually caused by LPO of crystallographic axes of olivine, which is the main constituent of the Earth's mantle, and which fast symmetry axis aligns roughly parallel to the direction of maximum extension or is controlled by the flow direction. Therefore, seismic anisotropy can be highly informative on the past (inherited) and present tectonics. In this PhD Thesis we retrieve the crustal model in three different regions in Italy: 1) the Colli Albani volcanic district. This is a geographically limited area SE of Rome, which has been interested by recent (Quaternary) magmatic activity. The Colli Albani Volcano is one of the several volcanoes and caldera complexes developed starting from Pliocene along the Tyrrhenian coast and forming the Roman Magmatic Province. 2) The Northern Apennines. The northern Apenninic arc is the surface expression of the subduction process of the northernmost segment of the Adria lithosphere beneath the Tyrrhenian basin. The growth of the mountain chain is related to the emergence of the accretionary prism that developed within the subduction zone. At present the subduction process here has slowed or perhaps terminated due to the exhaustion of the oceanic or thinned continental crust available for subduction, even if the signature of subduction is preserved. 3) The Southern Apennines. Southern Apennines is characterized by extensive outcropping of carbonate platform rock. It has been theatre of large and destructive earthquakes in the past, and is locus of the main hydrocarbon reservoir on land in Italy. Despite of the extensive oil exploration, the deeper portion of the crust here is largely unknown.

As additional case of study, since the exceptional nature of the event, we explore the crustal structure in the epicentral area of the earthquake, which struck L'Aquila in the 2009.

In the following chapters crustal structure and properties of the above different regions will be discussed in detail.



## Deep Structure of the Colli Albani volcanic district (central Italy) from Receiver Functions analysis.

The Colli Albani is a Quaternary quiescent volcano, located a few kilometers southeast of Rome (Italy). During the past decade, seismic swarms, ground deformation and gas emissions occurred in the southwestern part of the volcano, where the last phreatomagmatic eruptions (27 ky) developed, building up several coalescent craters. In the frame of a DPC-INGV project aimed at the definition and mitigation of volcanic hazard, a temporary array of seismic stations has been deployed on the volcano and surrounding areas. We present results obtained using Receiver Functions (RF) analysis for 8 stations, located upon and around the volcanic edifice, and revealing how the built of the volcanic edifice influenced the pre-volcanic structures. The stations show some common features: the Moho is almost flat and located at 23 kilometers, in agreement with the thinning of the Tyrrhenian crust. Also the presence of a shallow limestone layer is a stable feature under every station, with a variable thickness between 4 and 5 km. However, some features change from station to station, indicating a local complexity of the crustal structure: a shallow discontinuity dividing the Plio-Pleistocenic sediments by the Meso-Cenozoic limestones, and a localized anisotropic layer, in the central part of the old structure, which points of the deformation of the limestones. Other two strongly anisotropic layers are detected under the stations in lower crust and upper mantle, with symmetry axis directions related to the evolution of the volcano complex.

### 2.1 Introduction

The Colli Albani volcanic district, is one of the several Quaternary caldera complexes developed in the back-arc region of the northern Apennines (*Faccenna et al.*, 1997, 2001) (see Figure 2.1). It is characterized by hyper-potassic magma originated during the wide extensional processes by partial melting of a K-metasomatised mantle source (*Sartori*, 1990; *Conticelli & Peccerillo*, 1992; *Faccenna et al.*, 2001).

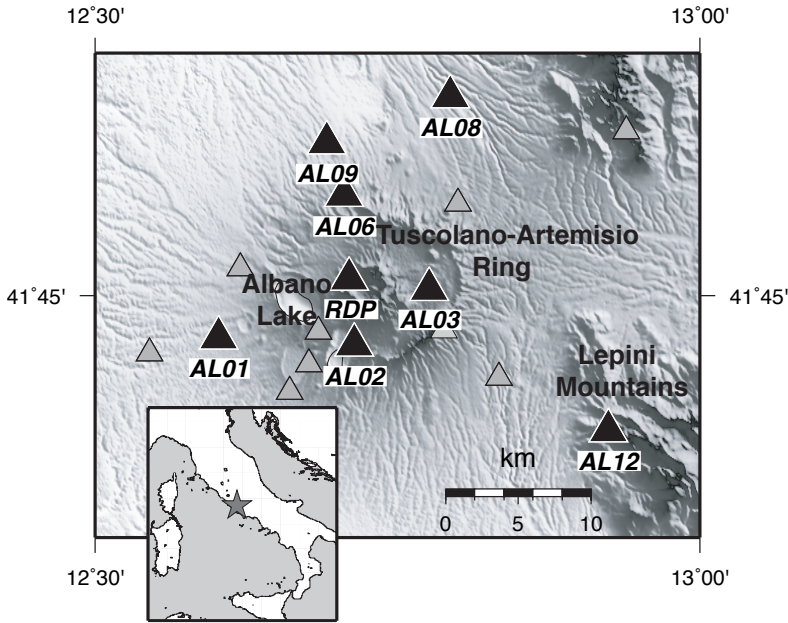


Figure 2.1: Map of the study area showing temporary seismic network distribution (triangles). Locations are selected to focus on the volcano and monitor the surroundings. Black triangles indicate stations used in this study.

The recurrence time between eruptions (in the order of  $10^4$  years) is comparable with the time elapsed since the last eruption (27 ka, (Fornaseri, 1985)), indicating that this volcano is classifiable as quiescent (De Rita et al., 1995; Giordano et al., 2006). Frequent episodes of unrest with seismic swarms (Amato et al., 1994), local ground uplift (Amato & Chiarabba, 1995), hydrothermal circulation and gas emissions (Quattrocchi & Calcara, 1995) are documented. The source of ground uplift has been interpreted as a magma inflation at 5-6 km depth beneath the phreato magmatic craters (Chiarabba et al., 1997), the location of the most recent volcanic activity (Giordano et al., 2006). Although geophysical data revealed the first order structure of the upper crust, clear information on the location of the crustal magma chamber is lacking. In this chapter we provide new evidences for the understanding of the crustal and upper mantle seismic structure beneath the volcanic area. We compute 3D S-wave velocity models for the volcano and surrounding region by analysing the Receiver Function (RF) of teleseismic data recorded at a temporary seismic network (Figure 2.1). The RF technique allows us to separate the effects of the structure under the observation point from the source function and the near source velocity structure, creating velocity models for the crust and upper mantle (Burdick & Langston, 1977). Although receiver functions are widely used to map crustal and mantle discontinuities (Ferris et al., 2003; Lucente et al., 2005), their use and potential on active volcanoes are still not fully explored (Nakamichi et al., 2002, and references therein). Recently, RF provided information on the anisotropic

properties of the crust (i.e. *Sherrington et al.*, 2004; *Ozacar & Zandt*, 2004) and mantle (*Vinnik et al.*, 2007; *Piana Agostinetti et al.*, 008a), opening new and original evidence for the flow of rocks at depth. In this study, we use RFs to define both S-wave velocity model and anisotropic fabric coupling harmonics analysis (*Farra & Vinnik*, 2000) and global inversion method (*Frederiksen et al.*, 2003) of RF data-set. Results show the presence of strong local heterogeneity, related to the growth of the volcano and the evolution on the magma supply system.

## 2.2 Previous information on the crustal structure

The Colli Albani volcano developed on the Tyrrhenian margin of the Italian peninsula (*Conticelli & Peccerillo*, 1992) at the intersection of regional trans-tensional faults which operated as *preferential* pathway for magma upwelling (*Funiciello & Parotto*, 1978). During the Quaternary, the pervasive extension of the Apennines back arc region produced the thinning of the Tyrrhenian crust and the development of volcanism on a broadly NW- trending belt (*Funiciello & Parotto*, 1978; *De Rita et al.*, 1995). The depth of the thinned Tyrrhenian crust ranges between 20 and 25 km, as revealed by previous RF studies and deep seismic profiles (*Pauselli et al.*, 2006; *Steckler et al.*, 2008; *Piana Agostinetti et al.*, 008a). In the Colli Albani, information on the crustal structure comes from the analysis of seismological data collected during the last 1989-1990 seismic swarm (*Amato et al.*, 1994), local earthquake and teleseismic tomography (*Chiarabba et al.*, 1994; *Cimini et al.*, 1994; *Chiarabba et al.*, 1997) and surface geology (*Funiciello & Parotto*, 1978; *Faccenna et al.*, 1994; *Giordano et al.*, 2006). Gravimetric surveys show the presence of NW-trending structural highs and lows of the Meso-Cenozoic carbonatic layer which constitutes the basement of the volcanic cover (*Toro*, 1978; *Di Filippo & Toro*, 1980). The top of the carbonates is located between 0.5 and 2.5 km depth, by geologic data (*Amato & Valensise*, 1986) consistent with seismic tomography (*Chiarabba et al.*, 1994) and gravimetric anomalies (*Di Filippo & Toro*, 1980). The last magmatic episode is documented by the intense seismic swarm and ground uplift of 30 cm observed in the western region of the volcano, where the more recent phreato-magmatic activity took place (*Amato & Chiarabba*, 1995; *Chiarabba et al.*, 1997). The uplift is consistent with the process of magma injection beneath the phreato-magmatic craters. Geodetic modelling indicates that the injection is at 5-6 km depth, just within a high  $V_p$  body interpreted as the top of solidified material (*Feuillet et al.*, 2004). Earthquakes have occurred within the overburden carbonate layer, above the inflating source. At present, seismic tomography has failed to identify a low  $V_p$  and low  $V_s$  anomaly attributable to a crustal magma chamber. A dike-like structure is hypothesized on the basis of the high P-wave velocity anomalies observed in the uppermost crust (*Feuillet et al.*, 2004). Partial evidence for the existence of a low velocity zone in the lower crust underneath the south-western part of the volcano came from teleseismic tomography (*Cimini et al.*, 1994).

## 2.3 Teleseismic data-set & Methods of data processing

We use teleseismic data collected by a DPC-INGV project whose aim is the understanding of active volcano-related processes in the Colli Albani. During the project, 23 seismic stations were deployed and operated for 1-2 years. Digital seismic stations were continuously recording and equipped with Lennartz 5s and Trillium 40s sensors (Figure 2.1). In this analysis, we use  $M_w \geq 5.5$  teleseismic events with epicentral distance between  $30^\circ$  and  $105^\circ$ , recorded at 8 seismic stations (Figure 2.1), selected to achieve the best coverage of the volcano structure at depth. Those stations have a good back-azimuthal distribution and a high signal to noise ratio. We obtain RFs deconvolving the vertical from the radial (R) and transverse (T) horizontal components (see *Langston, 1979*). RFs are calculated through a frequency domain deconvolution (*Di Bona, 1998*) using a Gaussian filter (a=4) to limit the final frequency band at about 2 Hz. A better signal-to-noise ratio is achieved by stacking the RFs coming from the same backazimuth direction ( $\Phi$ ) and epicentral distance ( $\Delta$ ). RFs are binned in areas  $10^\circ$  and  $20^\circ$  wide in  $\Phi$  and  $\Delta$  respectively, to optimize the signal to noise ratio, (*Park et al., 2004*) the number of RFs composing each bin varies between 1 and 35. If seismic rays pass through isotropic media, Ps converted phases are independent of backazimuth and no energy on the T component is seen. Conversely, if the amplitude of the converted Ps phases on the T component is not null, and varies with the backazimuth angle, complex heterogeneities exist. Widely known phenomena that produce such feature are seismic anisotropy and dipping discontinuities (*Levin & Park, 1998*). We can discriminate a dipping interface from some forms of anisotropy by using an azimuthal filtering. In the case of hexagonal anisotropy with a horizontal axis of symmetry, R and T vary in the azimuth domain with a periodicity of  $180^\circ$ . Instead in the case of a dipping interface or anisotropy with a dipping axis of symmetry, the related effects vary in the azimuth domain with a period of  $360^\circ$  (*Savage, 1998; Maupin & Park, 2007*). Harmonic angular stacking has been introduced to isolate out the different periodicity of Ps converted phases (i.e. *Girardin & Farra, 1998*). While the K0 harmonic (simple stacking) is the sum of all the RFs and contains information on the isotropic structure underneath the station, the k-th harmonics reveal those features that have a periodicity equal to  $2\pi/k$ . Since a preliminary analysis of our data set revealed that the energy on the T component is considerable, we investigated the amplitude variations of the converted  $P_s$  phases on the T component with respect to  $\Phi$  variation. We applied an azimuthal filter to our RF data-set, for both first and second harmonics, to eliminate the effects of noise and point out the presence of hexagonally anisotropy and dipping planar discontinuities. We extracted the k-th harmonics from the R (and T) data-set by summation of the components of individual RFs with weight  $W_i^R$  (and  $W_i^T$ ), dependent on the azimuth (*Farra & Vinnik, 2000*, see for details). If the RF contains energy in the k-th harmonics, the weighted sum of the R and T should present some homogeneity in the distribution of the signal. We stacked the R and T distribution (R+T) and amplified the signal, in case of similarity

between R and T (Vinnik *et al.*, 2007). The analysis of R+T diagram is useful to highlight the axis of three-dimensional features.

### 2.3.1 Dipping layer vs anisotropy with a dipping symmetry axis

The presence of dipping layers or anisotropy with a dipping symmetry axis results in a rotation of the energy out of the ray-propagation plane. Both structures generate  $Ps$  converted phases on R and T that show a  $360^\circ$  periodicity with  $\Phi$ . Lateral heterogeneity other than these would likely produce rougher patterns of amplitude variation with  $\Phi$ . Distinguishing between dipping and anisotropic layer is challenging (Savage, 1998; Maupin & Park, 2007). In Figure 2.2, we show RF synthetic data from three models which have: two parallel dipping interfaces at depth (Model A, Figure 2.2a), an anisotropic layer with dipping fast symmetry axis (Model B, Figure 2.2d) and an anisotropic layer with dipping slow symmetry axis (Model C, Figure 2.2g). Model A consists of two N-striking,  $30^\circ$  E-dipping interfaces. Model B has a E-trending  $30^\circ$  plunging fast axis, while model C has a W-trending  $60^\circ$  plunging slow axis. The pattern on the R and T components is similar for the three models, suggesting that only *a priori* information can help identify the right model. The similarity due to the anisotropy merits a deeper discussion. To reproduce the same pattern, fast and slow anisotropy axes should trend in opposite direction and plunge with a complementary angle (Sherrington *et al.*, 2004). A small velocity jump is required for one of the two models. Also the peak amplitude of the converted phases varies slightly, but such variation is not easily detected in real dataset. Hypothesized anisotropy is hexagonal and, whereas other symmetries can be present in the Earth, this is the simplest geometry able to reproduce the major observable effects (Becker *et al.*, 2006). Uniform seismic anisotropy at large (teleseismic) scale could be present in several geological settings. While mantle anisotropy is widely accepted to be due to the physical properties of the aligned olivine crystals, there are many potential causes for crustal anisotropy. Among these, the main factors are the presence of non-hydrostatic stresses inducing aligned micro-cracks in the shallow crust, the layering of sedimentary piles, and the alignment of anisotropic mineral grains in deeper portion of the crust, i.e. lamination of the lower crust (Meissner *et al.*, 2006). All these causes can be approximated using hexagonally anisotropy with a unique slow or fast symmetry axis, respectively. As previously demonstrated, to discriminate between the two kind of anisotropy could be difficult. In this study, forward modelling test and available geological information have been used to constrain *a-priori* the nature of the heterogeneities, selecting either the slow or fast axes based on which is the most likely cause for anisotropy.

## 2.4 Inversion Method

RF modeling is a strongly non-linear and non-unique inverse problem since there is still a trade off between thickness and seismic velocity inside layers. However

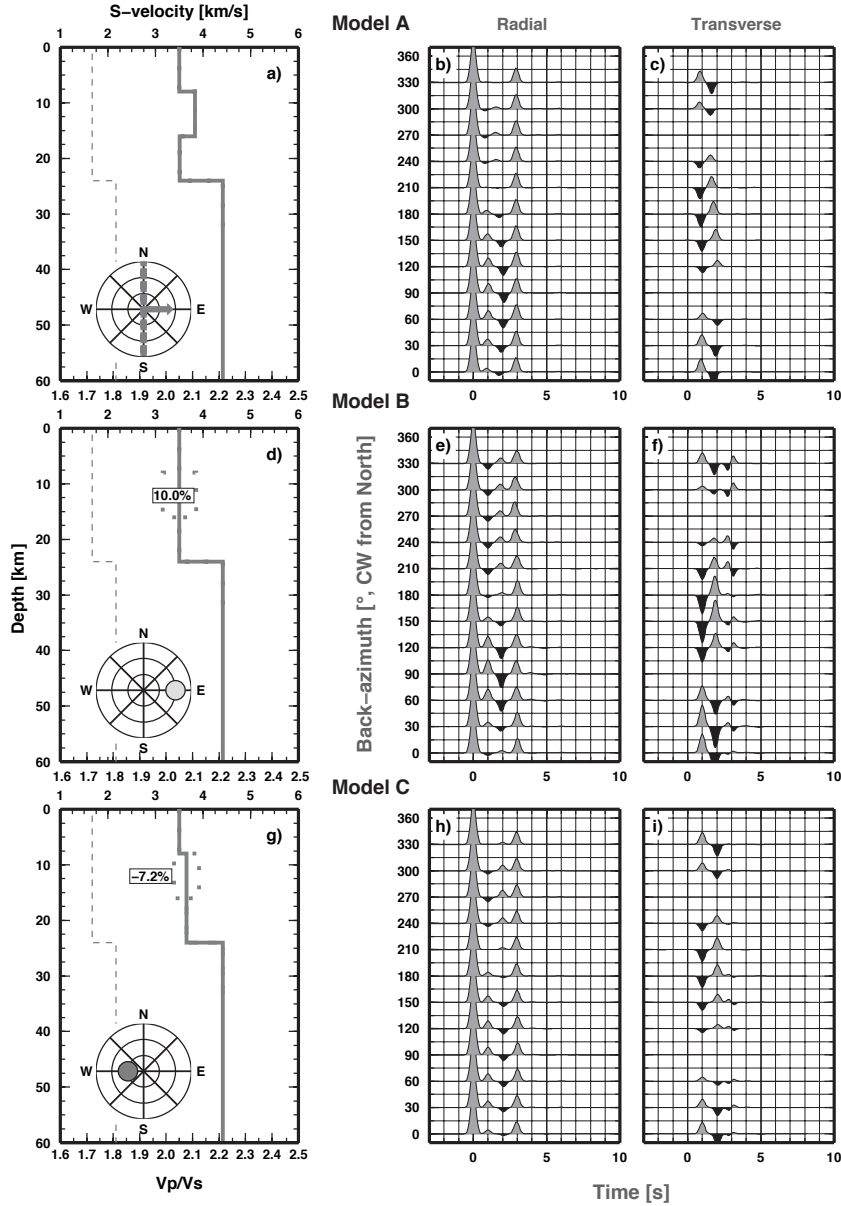


Figure 2.2: S-velocity Model, and Radial and Transverse synthetic RF for Model A (panels a-c), Model B (panels d-f), and Model C (panels g-i). In panels (a), (d) and (g), grey lines indicate the S-wave velocity profile. Heavy and light dashed line show the anisotropy and the  $V_p/V_s$  with depth. In the right bottom corner, southern emispheric projection of the 3D parameter of each model is reported. Light and heavy grey circles indicate the direction of the symmetry axis in fast and slow anisotropic layers, respectively. A grey dashed line coupled with a grey vector displays the strike and the dip of a dipping discontinuity, respectively. Synthetics RF are plotted as a function of the back-azimuth of the incoming wave, keeping fixed the ray parameter. Positive and negative amplitudes are shown in grey and black, respectively. Zero-time is the direct-P arrival.

geological and geophysical information could be used to guide the global search, thus reducing the dimensionally large parameter space.

In this study, we use a Neighbourhood Algorithm (NA) to iteratively sample good data-fitting region of our parameter space and to extract information on the 3D crustal structure (*Sambridge, 1999, 1999b*, see for details). NA has been extensively used to solve RF inverse problems (*Piana Agostinetti et al., 2002; Frederiksen et al., 2003; Bannister et al., 2004; Nicholson et al., 2005*) Following the original implementation of the NA, we initially generated 1000 samples from the parameter space. From the neighbourhood of the best fit models, 40 new samples are iteratively resampled. After 500 iterations we obtained an ensemble of 21,000 models. Synthetic seismograms are computed using the RAYSUM code, which models the propagation of a plane-wave in dipping and/or anisotropic structure (*Frederiksen & Bostock, 2000*). We calculated the multiples only for the first layer, since they can be very large due to the great impedance contrast between sediments and bedrock. Multiples for deeper discontinuities have a smaller impact on the waveform (*Sherrington et al., 2004*, see for a discussion). Then, we proceed to the model uncertainties by applying the second step of the NA (*Sambridge, 1999b*). The method allows us to calculate the mean model and the posterior probability density (PPD) function through the Bayesian inference. The Bayesian solution to an inverse problem is the PPD, so Bayesian integrals are calculated from the PPD, by using a Monte Carlo method, in the model space such that their distribution follows the PPD. Here we generated 90,000 points for Monte Carlo integration.

### 2.4.1 Parameter space

To avoid geologically unreasonable structures, the parameter space has been restricted based on the available geological and geophysical information on rocks and velocities for the Colli Albani and the surrounding regions (*Feuillet et al., 2004*). Our parameterization is composed by: (1) a layer of volcanics and sedimentary deposits with thickness varying between 0 and 1.5 km, and  $V_s$  ranges between 1.2 and 2.8 km/s; (2) a limestone layer with variable thickness (between 3 to 5 km), with  $V_s$  between 3.2 and 3.6 km/s, and  $V_p/V_s$  between 1.85 and 1.95; (3) a mid crust layer, and a lower crust layer, each 5 to 15 km thick, with  $V_s$  between 3.2 and 3.8 km/s; (4) an upper mantle layer with  $V_s$  ranging between 4.1 and 4.5 km/s; (5) an half space with mantle  $V_s$  velocities.

The 1D parameter space is summarized in Figure 2.3. In the inversion, we use information from the harmonics analysis to restrict the search on the 3D parameters in two ways. First, time delay of the main pulses on R+T diagram broadly constrains the presence of local heterogeneities at depth (*Vinnik et al., 2007*). Second, the direction of the polarity inversion on the K1 diagram suggests us a range for the strike of dipping interfaces or the trend of anisotropy symmetry axes.

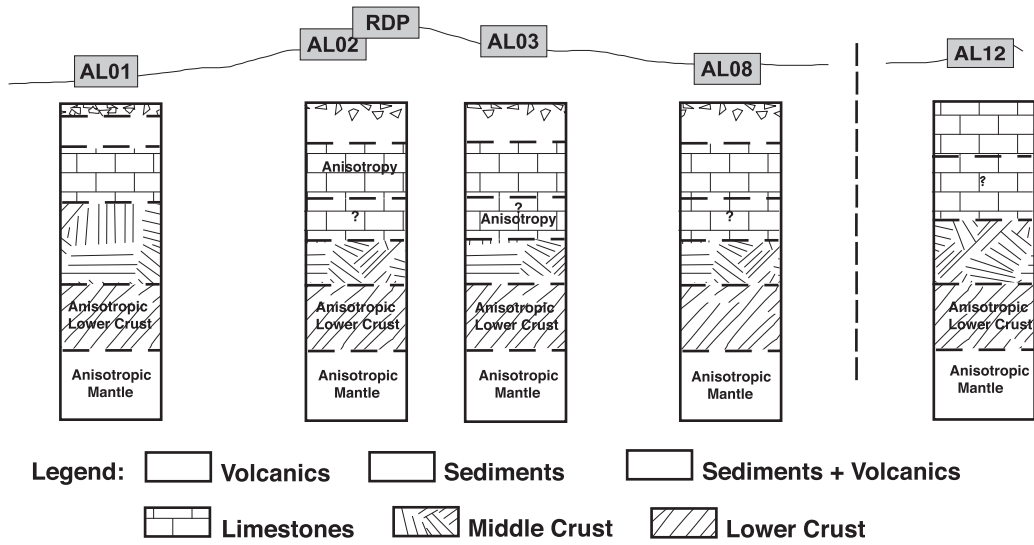


Figure 2.3: Schematic initial parameter space for indicated stations. Stations AL06 and AL09 have the same initial parameter space as AL08 with anisotropy in the lower crust too. Vertical axis is not in scale.

### 2.4.2 Sensitivity to 3D parameters

In this section, we present the inversion method applied to RDP data-set to show how the inversion can discriminate the number of anisotropic layers and the amount of anisotropic percentage. We choose RDP seismic station because of the large and clear data-set available. The station is located on the central cone of the ancient structure of the volcano.

#### Number of anisotropic layers

Figure 2.4a displays the mean S-velocity model retrieved at the end of the inversion process. In Figure 2.4b, we show the harmonics components of both observed RF data set and synthetic RFs computed using the mean model (the 3D parameters are shown in Figure 2.4c). The fit between observed and synthetic traces is fairly good. RDP data-set shows two strong features on the K0 diagram (black line in Figure 2.4a): the top of the limestones, Ps converted phase at about 1 s, and the Moho converted phase at about 3.5 s. Both these phases are well reproduced by the synthetic K0 diagram. The necessity of introducing anisotropic layers is explained by the presence of 5 phases on the K1 diagram located at about 0.5, 1.0, 2.0, 3.5 and 4.0 s. We choose to introduce 3 anisotropic layers after some trials on models with less anisotropic layers. In Figure 2.5, we show how the progressive increase of anisotropic layers improves the fit. Results from a simple 1D inversion, i.e. without anisotropic layers, although achieving a very good fit to the radial signal, obviously fail to reproduce the K1 signal, due to the absence of 3D parameters (Figure 2.5d). The introduction of an anisotropic layer in the upper crust is useful to fit the K1 signal between 0 and 1 s, while the sub-Moho anisotropic layer gives a strong signal between 3 and 4 s similar to the signal in Figure 2.5f gather. A third anisotropic layer (in the lower crust) is necessary to fit the arrival at about 2 s (Figure 2.4b, K1 gather). The comparison of these four models (Figures 2.4a and 2.5a) gives additional consistence to the 1D model, displaying a thin layer of sediments over the limestones and a low velocity lower crust. The Moho depth is confined between 21 and 26 km.

#### Anisotropy amount

Seismic anisotropy in the upper mantle is known to be theoretically as large as 20%. However, no percentage of anisotropy larger than 5% is usually observed at upper mantle depths (e.g. *Tommasi et al. (1999)*). In this study our percentage of anisotropy vary between 8 and 12%, stronger than expected, but necessary to fit the pattern described by data. A conservative value for mantle anisotropy (5%) is not enough to produce the right phase amplitude (left panel of Figure 2.6). Conversely 10% of anisotropy gives a better fit to the waveform. Such high value is consistent with recent studies (*Levin et al., 002b; Savage et al., 2007; Vinnik et al., 2007; Piana Agostinetti et al., 008a*) and theoretical predictions (*Blackman & Kendall, 2002*).

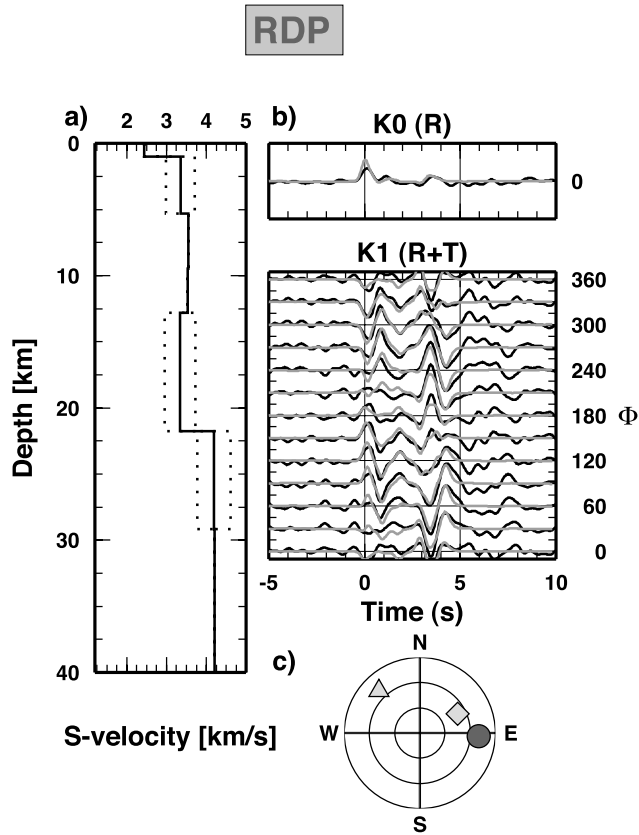


Figure 2.4: (a) Mean S-velocity model for station RDP. Solid line indicates S-velocity profile, while dotted lines enclose anisotropic layers. (b) K0 and K1 harmonic coefficient expansion (HCE) for station RDP. Observed HCE (black lines) are overplotted by synthetic HCE (grey). (c) Southern emispheric projection of the 3D parameters for RDP model. Circle indicates trend and plunge of the symmetry axis in the upper crust anisotropic layer, triangle shows trend and plunge for the anisotropic layer in the lower crust, diamond shows trend and plunge of the upper mantle anisotropic layer.

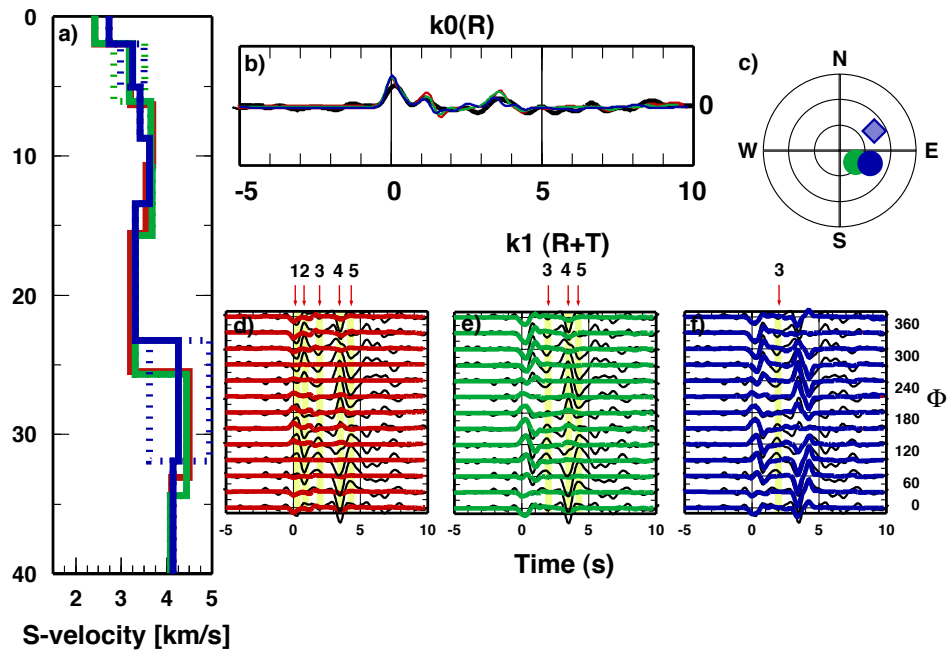


Figure 2.5: (a) S-velocity models for station RDP, red model has no anisotropic layers, green model has only the upper crust anisotropic layer, blue model has the upper crust and the upper mantle anisotropic layers. (b) K0 diagram comparing data and synthetics for the three models in panel (a): red, green and blue wiggles correspond to the the relative color model. (c) Southern emispheric projection of the 3D parameters: circles indicate trend and plunge of the symmetry axis in the upper crust anisotropic layer, diamond shows trend and plunge of the upper mantle anisotropic layer. In panels (d), (e) and (f), K1 gathers comparing data (black) and synthetics (color) for the three models in panel (a).

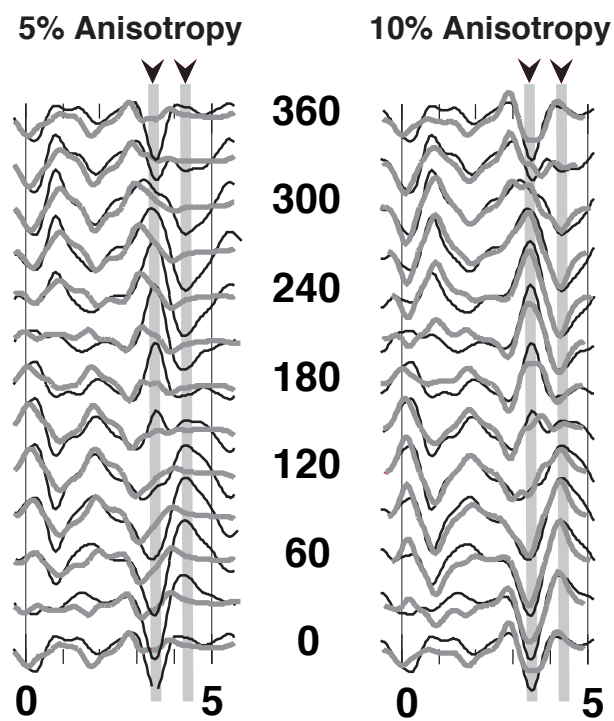


Figure 2.6: Comparison for upper mantle anisotropy values. On the left, observed RF (black lines) and synthetic RF (grey) computed from a model with 5% of upper crustal anisotropy. On the right, the same but for a model with 10% of upper mantle anisotropy.

### 2.4.3 Errors on layer thickness

We estimate the errors on the thickness of the layers by adding random noise to a synthetic RF data-set and comparing the resulting models with the input model (Figure 2.7) (Vinnik *et al.*, 2004). In this case, both the input and the resulting models are performed for a 1D structure which is similar to the 1D S-velocity model computed for RDP. We assume a white gaussian noise in the RFs with a standard deviation of 0.25. We run the inversion in the same way of the real data; at the end of the search stage, we set a misfit threshold, i.e. 1.25 times the best-fit model misfit, and select all models in the ensemble which have the misfit lower than the threshold. We compute the variability of each inverted parameter as the min/max interval of the parameter in the selected family. We estimate the errors on the inverted parameters as the half-width of the intervals of variability of the parameters. This test allow us to define errors on thickness and depth: about 0.5 km for the shallow sediments thickness, 1 km for the limestones thickness, and 1.5 km for the Moho depth.

## 2.5 Results

We show and discuss the results of the 3D model inversion, with the aim of understanding the effects generated by the building of the volcanic edifice on undeformed crustal structure. To do that, we looked at results station by station focusing progressively on the volcano edifice, and we analysed the symmetry axes for each data-set. Also, trend and plunge of the symmetry axis detected in each anisotropic layer encountered are studied using the Bayesian approach and their PPD as shown in Figure 2.15.

Station AL08 is a reference for the regional structure surrounding the volcano, since it is located about 10 km to the NE of the caldera (see Figure 2.1) and close to the carbonate outcrops of the Apennines. For this station, the isotropic component of the harmonic analysis (K0) reveals a strong conversion at about 3.2 s, related to the Moho. The first harmonics (K1) shows two derivative pulses at about 0.5 and 3.5 s, with a polarity flip at about  $60^\circ$  of  $\Phi$  ( $\phi=150$  in Figure 2.8). The first feature indicates the existence of a shallow dipping interface. Since the Moho conversion occurs at 3.2s, the second feature is consistent with the presence of an anisotropic layer in the upper mantle. Consequently, our *a priori* information consists of a dipping interface between the first and second layers and a fast anisotropic layer underneath the Moho. The computed 3D model shows a thin sedimentary cover,  $\sim 1$  km thick, lying above a 5 km thick carbonate sequence ( $V_s$  3.3 km/s). Underneath the limestone layer, we observe very high S-wave velocities (3.6 km/s between 6 and 13 km depth), and a  $V_s$  reduction in the lower crust. The Moho is modelled at 22 km depth, and the sub-Moho anisotropic layer shows an axis trending  $N64^\circ$ , plunging  $35^\circ$ .

Station AL01 is located on the western side of the volcano, about 6 km from the Albano lake. The K0 component presents a negative pulse at 1.5 s, followed by a positive pulse at 2.5 s, related to the conversion at the Moho. The K1 component shows a derivative pulse in the first second, with a polarity that reverses at  $\phi=150^\circ$  and a second couple of pulses between 2.5 and 4 s. While the

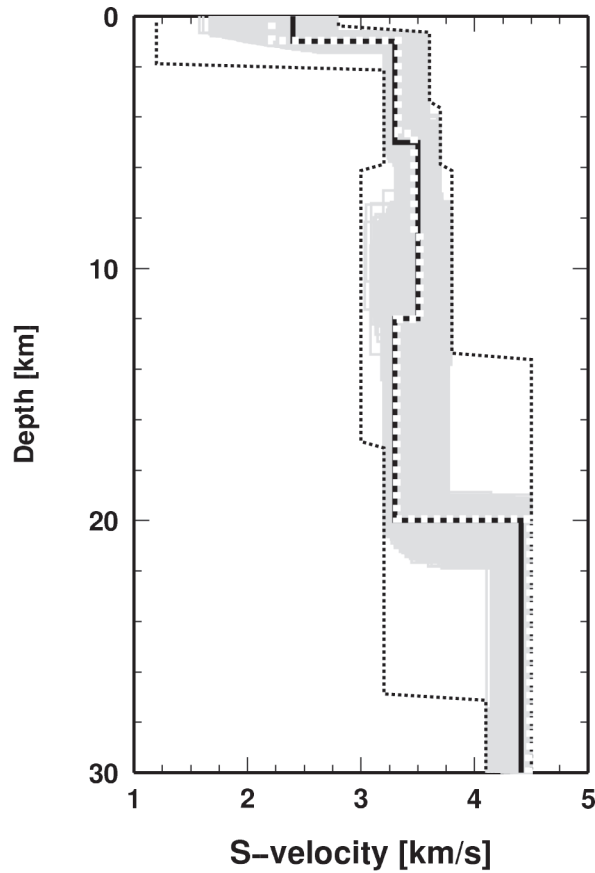


Figure 2.7: Estimating the standard error of inversion by numerical experiment. Solid black line indicates the "true" model, used to generate the "observed" dataset. The grey area is composed of all the best-fit models selected from the entire sampled ensemble. The bounds for velocity are shown by thin dashed line, while a white dashed line indicates the best-fit model.

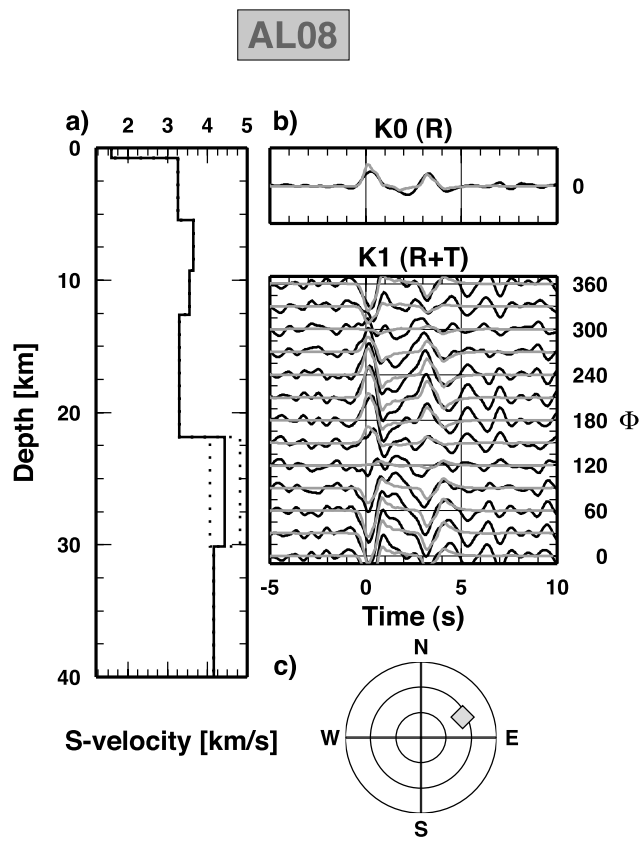


Figure 2.8: As in fig 2.4 for station AL08.

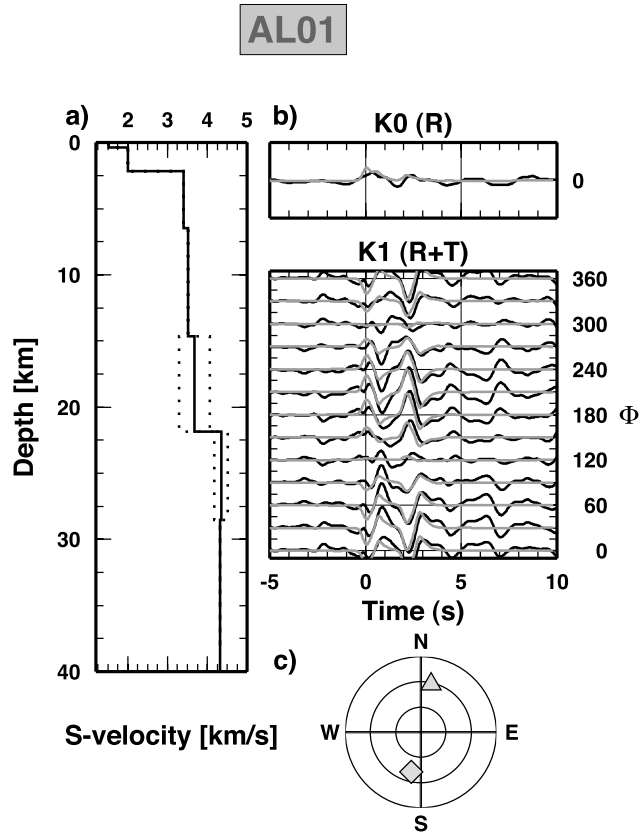


Figure 2.9: As in Figure 2.4, for station AL01.

former can be related to a shallow dipping discontinuity, the latter requires two anisotropic layers, in the lower crust and in the mantle. The anisotropic layer in the lower crust is needed to fit the data. In the uppermost crust, the 3D model shows a 0.5 km thick volcanic cover overlaying a  $\sim 2$  km thick Plio-Pleistocene sediment layer and a 4 km thick carbonate layer. Underneath the limestone, we find a small S-wave velocity jump between 7 and 15 km depth, consistent with the Pre-Mesozoic basement. In the lower crust, we find a 7 km thick anisotropic layer with high S-wave velocity, its axis trends  $N12^\circ$  with a  $32^\circ$  plunge. In the uppermost mantle, beneath the Moho modelled at 22 km depth, a layer with a small anisotropy (3.9%) is observed oriented  $N194^\circ$  plunging  $41^\circ$  (Figure 2.9).

Station AL12 (Figure 2.10) is located to the south of the volcano on the carbonate units of the Lepini mountains. On the K0 component, we observe a clear pulse at 3 s, related to the Moho. The K1 component shows a couple of pulses flipping at about  $120^\circ$  (at 0.5-1 s), and two broad pulses at 3-4.5 s, flipping at the same direction, interpreted by a shallow interface and two deep

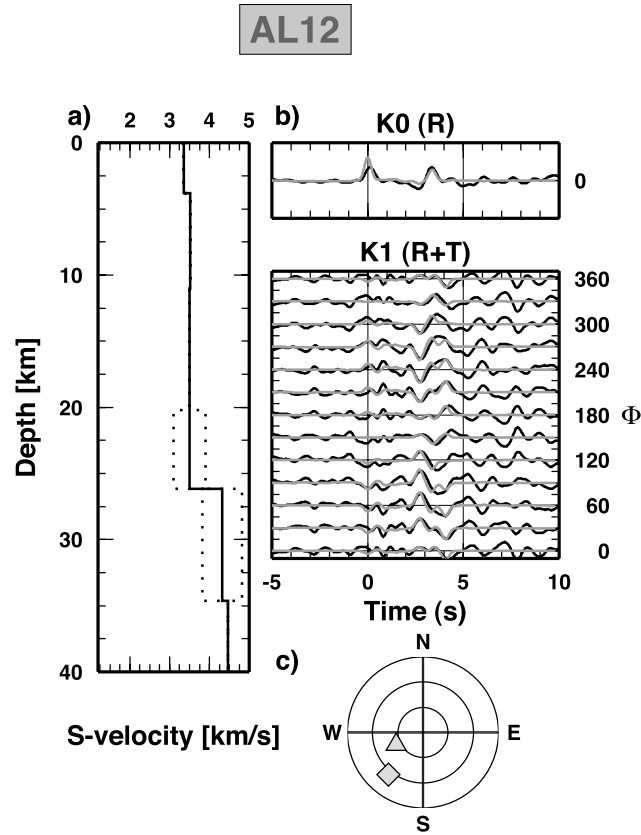


Figure 2.10: As in Figure 2.4, for station AL12.

anisotropic layers. The obtained crustal structure is simple: a 26 km thick crust with an almost constant S-wave velocity. The shallow interface coincides with the base of the carbonate layer, and shows a gentle dip towards SW. In the lower crust and uppermost mantle, we find two highly anisotropic layers, the first is oriented N245°, plunging 55° the latter trends N219°, plunging 25°. These two layers are separated by the Moho modelled at 26 km depth.

Station AL06 is located on the northern edge of the Tuscolano-Artemisio caldera ring (see Figure 2.1). The K0 component shows the Moho related pulse at 3.3 s. The K1 diagram shows three main couple of derivative pulses at 1, 2 s and between 3.5 and 5 s (Figure 2.11). We attribute the first couple to a shallow dipping layer and the two later pulses to anisotropic layers located above and below the Moho. The sharp pulses at 2 and 3.5 s strongly require the anisotropic layer in the lower crust. The 3D velocity model reveals a thick (2 km) layer of volcanic rocks overlaying a 5 km thick carbonate sequence, separated by a 340°-striking and 17° E-dipping interface probably indicating the top of the

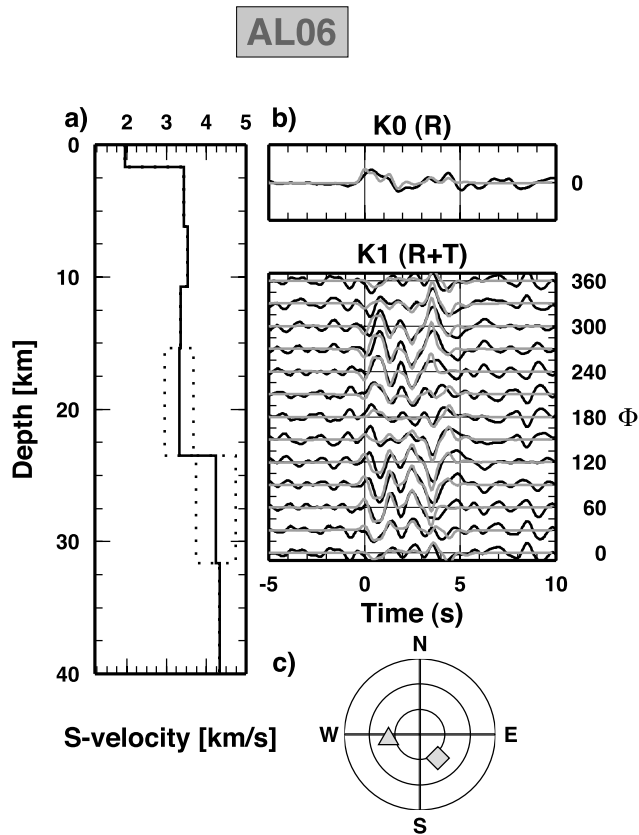


Figure 2.11: As in Figure 2.4, for station AL06.

limestone. Anisotropy is revealed in the lower crust with  $N254^\circ$  trending axis, plunging  $65^\circ$ , and an uppermost mantle with a  $N144^\circ$  oriented axis, plunging  $39^\circ$ . The Moho is modelled at 25 km depth.

Station AL09 is located a few kms to the north of station AL06 and similarly is featuring a shallow dipping interface and two deep anisotropic layers. Anyway, the trending of interfaces and anisotropy axes deduced by the harmonics analysis are different. In the K1 diagram (Figure 2.12), we observe two pulses at 1-1.5 s (flipping at  $N330^\circ$ ) due to the shallow dipping layer, and two pulses between 2.5 and 4 s, due to two anisotropic layers with the fast axes trending between  $N200^\circ$  and  $N300^\circ$ . The computed model shows a  $\sim 1$  km thick sediment layer lying above a 5 km thick limestone layer. The base of the limestone coincides with the  $N128^\circ$ -striking,  $35^\circ$  W-dipping discontinuity. The lower crust has a  $N240^\circ$ -trending  $55^\circ$  plunging anisotropy fast axis. The Moho is modelled at 23 km depth, and the fast axis of anisotropy in the uppermost mantle is  $N256^\circ$ -trending and  $54^\circ$  plunging.

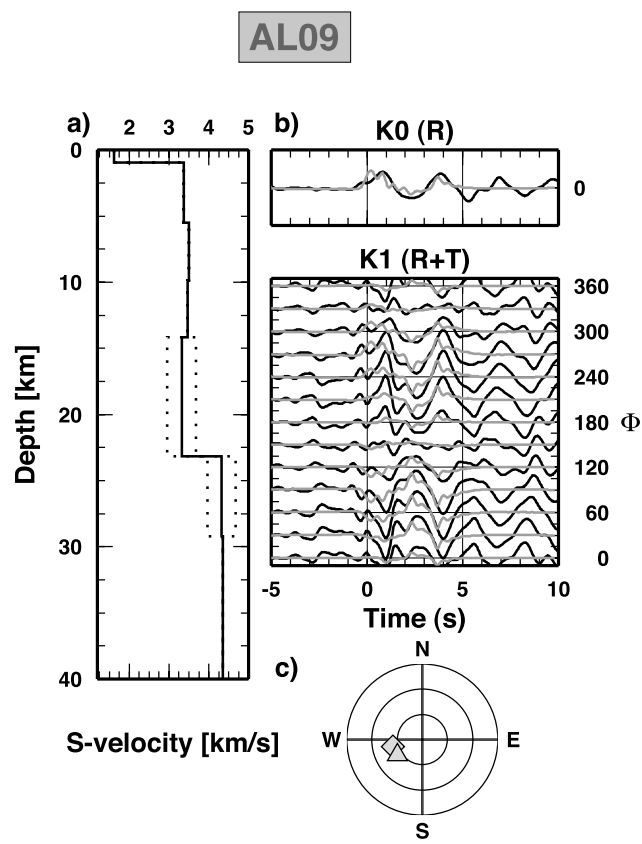


Figure 2.12: As in Figure 2.4, for station AL09.

The three stations AL02, AL03 and RDP are located inside the Tuscolano Artemisio caldera, over the volcanic products related to the second and the final volcanic activity (see *De Rita et al.*, 1995)

On K1 diagrams, stations AL02 and RDP show similar couple of pulses with the same arrival time, but with different directions of polarity inversion (Figures 2.13 and 2.4). We observe two coupled pulses in the first second, a single phase at 2 s, and two coupled pulses between the 3 and 4 s. The coupled pulse in the first second is only revealed at the stations inside the caldera and is due to a very shallow feature. In the uppermost few kms, the deep structure of the volcano is composed by volcanic rocks and Meso-Cenozoic limestone units (see *Chiarabba et al.*, 1994). Therefore, we associate the coupled pulse to a shallow anisotropy derived from the layering of sedimentary rocks, preferential sites for magmatic intrusions. In this case, the anisotropy axis would be slow and perpendicular to the layering. While arrival times of the first couple are exactly the same for both stations, the polarity change occurs at N270° and N30° for AL02 and RDP, respectively. This sharp variation at very close stations suggests that both axes are pointing roughly towards the center of the volcano. The two other features are the lower crust and uppermost mantle anisotropic layers, features already observed for the other stations. Velocity models obtained for these two stations are similar. In AL02, we find two shallow layers related to the volcanic rocks and sediments (2 km thick) and to the limestones (4 km thick). The slow anisotropic axis trends N21° and plunges 54°. The lower crust anisotropy fast axis is oriented N234° and plunges 57°. The Moho is located at 23 km, and the upper mantle anisotropic fast direction is N35°, with a plunge of 29°. In RDP, the sediment and volcanic layer is 1 km thick, the carbonate layer is 4 km thick and the slow anisotropic axis is oriented N93°, with a plunge of 20°. The lower crust anisotropic axis is N316° with a plunge of 20°. The Moho is located at 21 km depth and the upper mantle fast anisotropy direction is N63°, with a plunge of 40°. Station AL03 is located 5-6 km to the southeast of AL02 and RDP. The harmonics analysis shows 5 pulses within the first and the fourth seconds. We associate the first couple of pulses to the shallow anisotropy already observed at AL02 and RDP. In AL03, its arrival time is slightly delayed (1 s) suggesting that the anisotropic layer is a few km deeper than for the two other stations. The *a priori* information for the modeling consists of three anisotropic layers, similarly to AL02 and RDP. The velocity model shows a 1 km thick sediment layer overlying 4 km thick limestones. The slow anisotropy axis, located at the base of the limestone layer, is N225° trending and 51° plunging. The fast axes have N336° and N194° with plunges of 30° and 47°, for the lower crustal and uppermost mantle anisotropic layers, separated by the Moho located at 22 km.

Figure 2.15 shows the Posterior Probability Distribution (PPD) for the anisotropic parameters estimated for each station. Well constrained parameters have a sharp Gaussian distribution. We observe that while the plunges of anisotropic axes have a broadened gaussian distribution, trends of anisotropic axes are generally well constrained; however some trend parameters are not well resolved, as for the lower layer of station AL01, AL02 and AL09. This happens because the shallowest layers, displaying a sharp gaussian, badly influence the resolution of the directions of deeper layers.

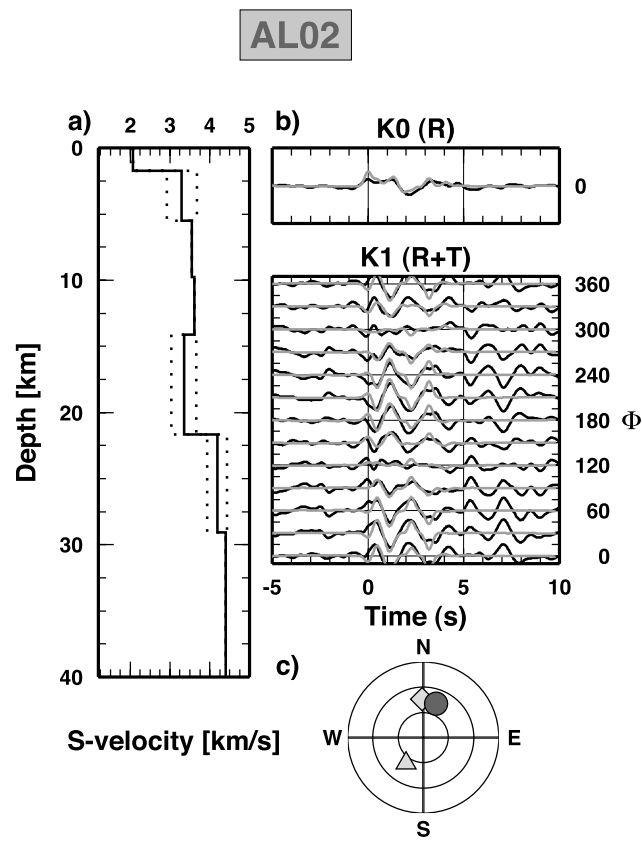


Figure 2.13: As in Figure 2.4, for station AL02.

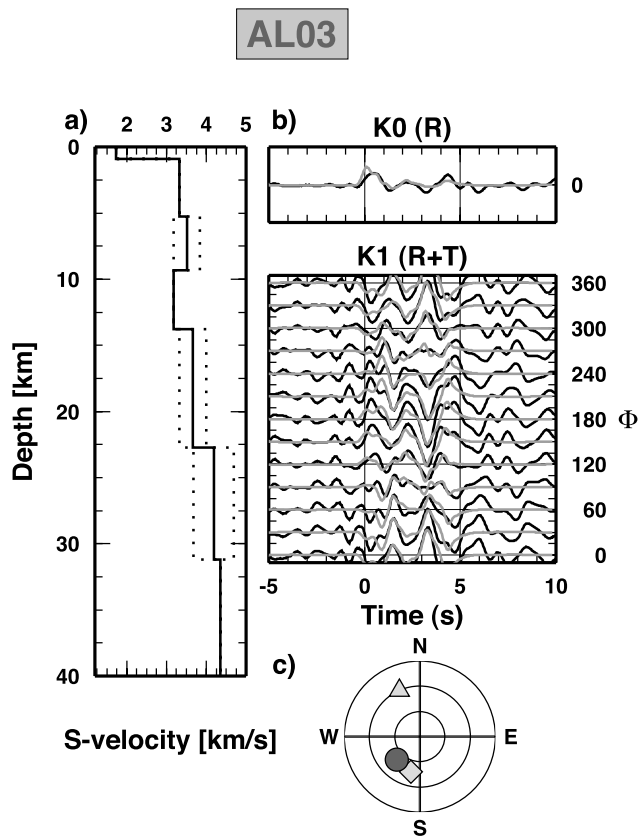


Figure 2.14: As in Figure 2.4, for station AL03.

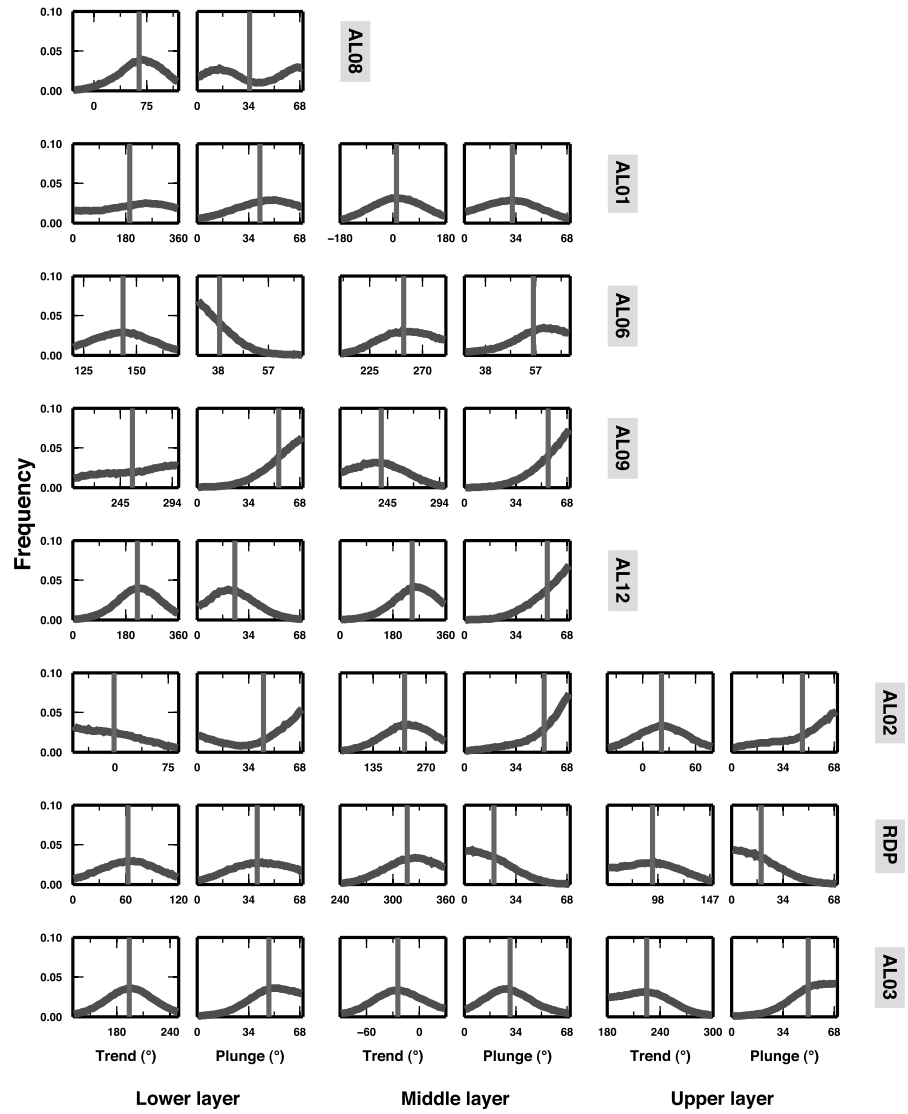


Figure 2.15: 1D *posteriori* probability density (PPD) function from Bayesian resampling. Here, only anisotropic parameters are reported (trend and plunge) for every anisotropic layer in the S-velocity profiles. Grey vertical lines indicate the mean of each distribution.

## 2.6 Discussion

Seismic wave velocity depends on several factors, including lithology, temperature, stress, fabric, mineralogy, fluid inclusions, and pore properties and pressure (O'Connell & Budiansky, 1977; Kern, 1982; Mavko, 1980; Sato *et al.*, 1989). In Quaternary volcanoes, the repeated accumulation of magma produces sharp and abrupt horizontal and vertical variations of P- and S-wave velocities. Seismological techniques help to indirectly trace the location and geometry of magma conduits, solidified intrusions and magma chambers (Lees, 1992; Mori *et al.*, 1996; Okubo *et al.*, 1997; Chiarabba *et al.*, 2004). In the Colli Albani, great effort was spent in recovering the uppermost crustal structure with tomographic techniques (Chiarabba *et al.*, 1994; Feuillet *et al.*, 2004). High P-wave velocity anomalies are identified and related to the presence of shallow solidified magmatic bodies nested within the limestone layer at 4-5 km depth. Since the last volcanic activity at the Colli Albani is older than 25 ka, and is volumetrically small, the crustal structure more likely reflects the older volcano activity, which was elevated between 600-200 ka (De Rita *et al.*, 1995).

The inversion of RFs adds significant new information on the crustal structure of the volcano and surrounding regions down to the uppermost mantle. The harmonics analysis points out that dipping discontinuities and anisotropy in the crust and upper mantle largely affect the RFs at the Colli Albani. Neglecting such 3D heterogeneities, the computation of an isotropic 1D S-wave velocity model may be severely biased (Christensen, 2004). Therefore, we computed 3D velocity models, inserting *a priori* the existence and the reasonable range for anisotropic parameters, and modelled contemporaneously the isotropic and anisotropic structure. The caveat is that 1D and 3D features are coupled on the RF and the modeling may be unbalanced towards either the isotropic or anisotropic parameters. We prefer to model at the best the 3D heterogeneities, leaving some small spurious discontinuities on the isotropic velocity profiles. Anyway, the robust isotropic features, i.e. the Moho and the top of the limestone layer, are well resolved and stable for all the stations. The existence of this coupling, undoubtedly present in complex tectonic structures, is rapidly emerging in RFs modeling, but still not completely addressed (Savage, 1998). We believe that our study provides new information for a more general use of RF in complex media. Our results shows that the  $V_s$  models define coherently the regional structure, featuring a thinned crust (21 to 26 km depth), shallow carbonate layers in the upper 6-8 km depth, and a general low  $V_s$  in the lower crust. In the shallow structure of the volcano (5-10 km depth), we do not observe a  $V_s$  reduction ascribable to a crustal magma chamber or melt (Nakamichi *et al.*, 2002). Conversely, we find a high  $V_s$  body located underneath the limestone layer, probably referable to an old intrusion and cold solidified material of the former volcano activity (Lees, 1992). Such body may be the intrusive root of the high  $V_p$  body revealed by local earthquake tomography at shallower depth (Feuillet *et al.*, 2004). Since the complexity of the shallow 3D features, we are not able to resolve the presence of tiny low  $V_s$  volumes in the upper 15 km beneath the resurging area. If new magma was emplaced in the shallow crust during the unrest episodes, the last of which occurred in 1989-1990, the

dimension of such bodies, nested within the high  $V_s$  old intrusion, should be small enough to be undetected by RF.

The most intriguing and innovative result is the recovering of strong anisotropic layers in the crust and uppermost mantle. The presence of seismic anisotropy is necessary to model the pulse variations on the R and T components observed in the RFs (Figures 2.8 to 2.14). Beneath the study region, we recognize three anisotropic layers (Figure 3.12). The shallow anisotropic layer changes in orientation even at close stations. It is present only at the three stations located within the caldera and became shallower moving towards the centre of the volcano. We attribute this feature to the layering of the sedimentary limestone pile, possibly alternated with intruded magma. For sedimentary rocks, the slow axis of anisotropy is perpendicular to the stratification (*Sherrington et al.*, 2004). The conic-like pattern, radial to the volcano, suggests that the limestone layer was deformed by the up-welling of magma in the central cone. Remains of the solidified magma are traced between 5 and 10 km depth by the high  $V_s$  at the three stations. Alternatively, the 3D feature observed on the RF can be explained by two dipping interfaces coinciding with top and bottom of the limestone layer. Since the resulting geometry of the carbonate layer is inconsistent with the available geologic data (*De Rita et al.*, 1988), we prefer the former interpretation. The second anisotropic layer is located in the lower crust (14-26 km depth) and is visible at almost all the stations. In the lower crust, seismic anisotropy is due to the alignment of minerals grains, metamorphism, ductile deformation or crustal flow during tectonic events (*Savage*, 1999; *Meissner et al.*, 2006). The percentage of anisotropy varies between 8 and 15% and the fast axis is sub-vertical (see Figures from 2.8 to 2.14), while the slow axis is almost sub-horizontal. Since the two different symmetry axes (fast and slow) generate the same feature on RF if oriented in opposite direction and plunging with a complementary angle, the choice of one or the other is absolutely arbitrary, as we show in section 3.1, and depends on crustal composition. In our results, we got direction for fast axes, but as showed in Figure 3.12 the slow associated axes for lower crust seems to fit better into the whole structure, arranging almost parallel to the fast axes detected in the upper mantle. This last anisotropic layer, located in the uppermost mantle below 25 km depth has a percentage of anisotropy of about 8-12% and is present at all the stations.

Although seismic anisotropy in the lower crust and uppermost mantle should be expected in case of a robust flux that aligns anisotropic minerals (biotite, amphibolite, granulite, olivine), evidence and measurements from seismological data are still poor. Recently, RF modelling showed the existence of several anisotropic layers in the lower crust in the Tibet region (see *Sherrington et al.*, 2004). The presence of such high anisotropy percentage in the mantle is striking, but reliable as demonstrated in section 4.2.2).

In Figure 2.17 we show a comprehensive sketch of our results. Sediments cover the entire area burying the limestones layer. The high velocities under the limestones are interpreted (where present) as the Triassic andyrites constituting the basement of the Mesozoic sequence. These two latter layers probably are locally deformed by the magma intrusion, and their tilt is the cause of the observed seismic anisotropy. This is in agreement with previous studies in

Deep Structure of the Colli Albani volcanic district (central Italy)  
 30 from Receiver Functions analysis.

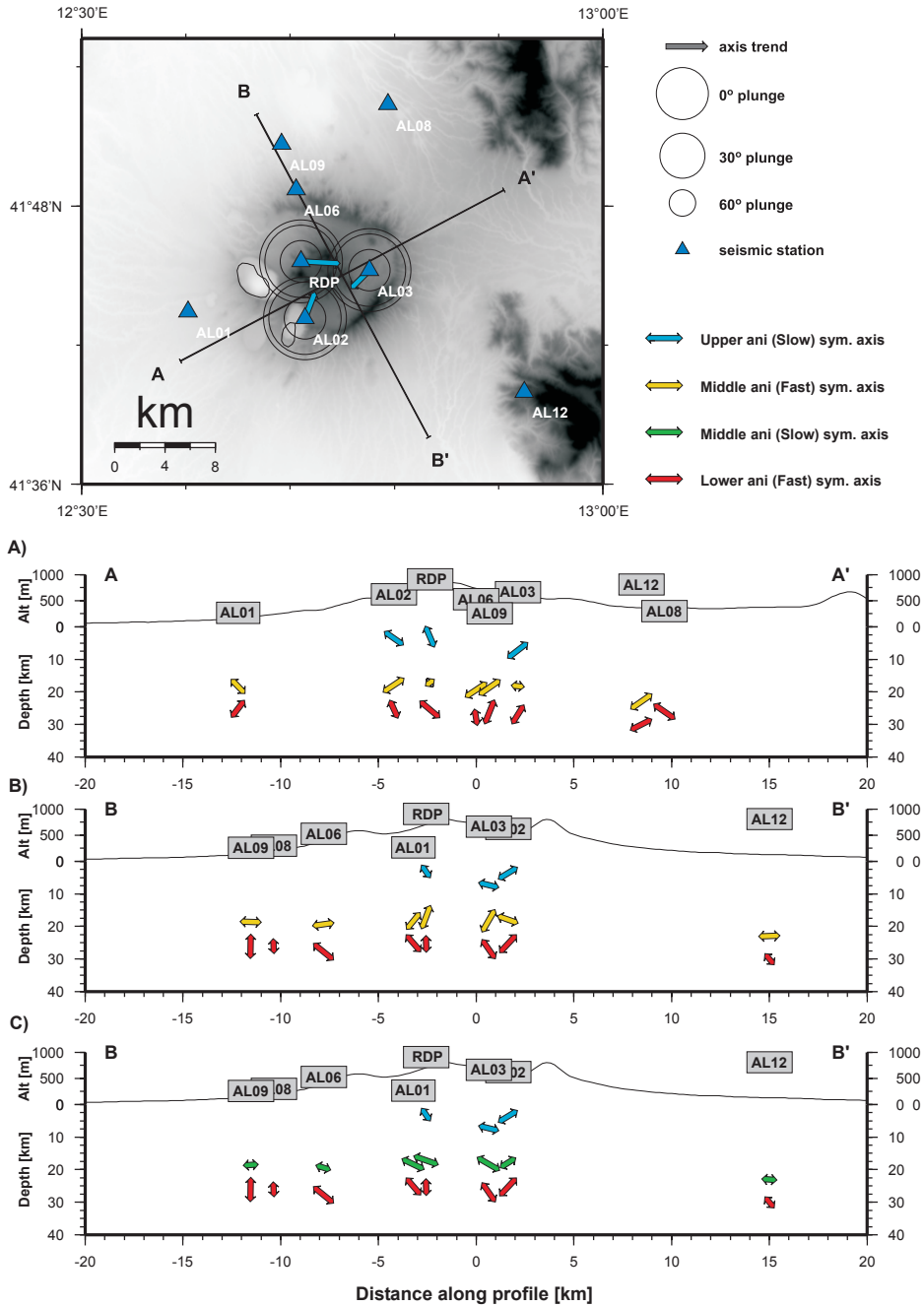


Figure 2.16: Map of the studied region, showing anisotropy axes direction (blue arrows) for the upper crust, and profiles AA' and BB' traces. (A) AA' and (B) BB' profiles showing distribution of symmetry axes in each anisotropic layer; color coding is: blue for the upper crust, yellow for the lower crust, and red for the upper mantle. (C) BB' profile, as for BB' in (B), but the green arrows indicate slow-axis in lower crust anisotropic layers.

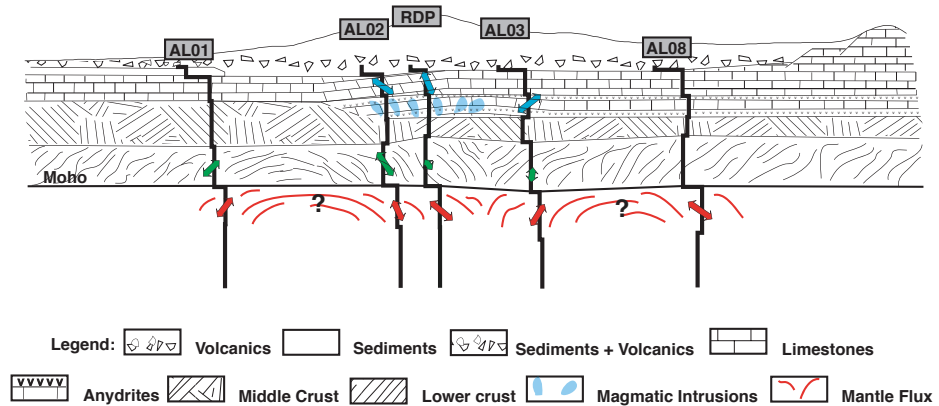


Figure 2.17: Summary sketch of results. Stations are projected on the AA' profile of Figure 3.12. Seismic anisotropy with negative slow symmetry axis is considered in lower crust, as in Figure 3.12c.

which the magmatic chamber was identified as a high  $V_p$  body at 5-6 km depth (*Chiarabba et al.*, 1997; *Feuillet et al.*, 2004).

The middle crust does not show any particular characteristic, while the lower crust and the upper mantle are characterised by strong anisotropy in which the symmetry axes distribution suggest that it is generated by localized deformation manifested in fossil fabrics. Three main tectonic events can reasonably have produced such fossil fabric: the Mesozoic extension related to the opening of the Tethys ocean, the Cenozoic compression that build up the Apennines and the more recent extension of the Tyrrhenian back arc region. During this last event, the pervasive extension in the Tyrrhenian plate, induced by the Apennines slab rollback (*Gueguen et al.*, 1998), re-organized the flow in the mantle wedge. In such case, a consistent sub-horizontal direction perpendicular to the slab edge should be expected, except in the corner flow region, and we do not observe a defined horizontal alignment of symmetry axes. We favour the interpretation of a sub-vertical flux in the mantle coherent with the magma up-rise from a mantle source located below 30 km depth. This flux, vigorous in the past 1-2 Ma, aligned the direction of mineral crystallographic axes in the mantle and in the lower crust. More speculatively, the variation of the plunge of fast axes, moving away from the volcano, suggests that the flux of magma followed local small-sized convective cells. At a local scale, the magma upraise beneath this volcano is mirroring the mantle flow of plate tectonics.

## 2.7 Conclusions

The analysis and modeling of teleseismic receiver functions helps to understand the crustal and upper mantle structure beneath the Colli Albani Quaternary volcano in central Italy. The 3D S-velocity models are consistent with the regional structure of the Tyrrhenian. Most robust features are: (1) limestones are present as remnants of the Mesozoic platform, they have thickness between 4 and 5 km. Their structure is plane, and for the stations under the calderic edifice they present a clear and well defined anisotropic pattern as on Figure 3.12; the slow anisotropic axes evidence a volcanic-related structure; (2) a high  $V_s$  value for the under-carbonates layer is recognised, this can be due to cold intrusive accumulated material. (3) a shallow Moho, present at depths between 21 and 26 km, as evidence of a thinned crust. (4) lower crust and an uppermost mantle in all the stations considered in this study show distinct anisotropic patterns. These are generated probably by the local flux of the ascended magma. This area is also involved in tectonic processes of back-arc extension, so fossil or active structures are deeply conditioned by both processes generating anisotropy.

Mapping seismic anisotropy using harmonic decomposition of Receiver Functions: an application to Northern Apennines, Italy.

Isotropic and anisotropic seismic structures across Northern Apennines (Italy) subduction zone are imaged using a new method for the analysis of teleseismic receiver functions (RFs). More than 13,000 P-wave coda of teleseismic records from the 2003-2007 RETREAT experiment are able to reveal new insights into a peculiar subduction zone which develops at the convergent margin of two continental plates and is considered a focal point inside the Mediterranean evolution. A new methodology for the analysis of receiver function is developed, which combines both migration and harmonic decomposition of the receiver function data-set. While migration technique follows a classical “Common Conversion Point” scheme and helps to focus on a crucial depth range (20-70 km) where mantle wedge develops, harmonic decomposition of a receiver function data-set is a novel and less explored approach to the analysis of *P*-to-*S* converted phases. The separation of the back-azimuth harmonics is achieved through a numerical regression of the stacked radial and transverse receiver function from which we obtain independent constraints on both isotropic and anisotropic seismic structures. The application of our new method to RETREAT data-set succeeds both to confirm previous knowledge about seismic structure in the area and to highlight new structures beneath the Northern Apennines chain, where previous studies failed to clearly retrieve the geometry of the subducted interfaces. We present our results in closely spaced profiles across and along the Northern Apennines chain to highlight the presence of the Tyrrhenian and the Adriatic side which differ in the thickness of the crust (about 25 km the first one, and about 40 km the second one). These two plates converge in the central zone where the Adriatic plate subducts beneath the Tyrrhenian. A signature of the dipping Adriatic Moho is clearly observed beneath the Tyrrhenian Moho in a large portion of the forearc region. In the area where the two Mohos overlap, our new analysis reveals the presence of an anisotropic body above the subducted Moho. There is a strong Ps converted phase with anisotropic characteristics

## Mapping seismic anisotropy using harmonic decomposition of 34 Receiver Functions: an application to Northern Apennines, Italy.

from the top of the Adriatic plate to a depth of at least 80 km. Because the Ps conversion occurs much deeper than similar Ps phases in Cascadia and Japan, dehydration of oceanic crust seems unlikely as a causative factor. Rather, the existence of this body trapped between the two interfaces supports the hypothesis of lower crustal delamination in a post-subduction tectonic setting.

### 3.1 Introduction

Developed between the European plate and the continental Adriatic microplate, the Northern Apennines (NA) are characterized by an active accretionary wedge that is actually below sea-level in central Adriatic but contains active thrust faults at the southern border of the Po River Valley (*Picotti & Pazzaglia, 2008; Wilson et al., 2009*) and the elevated area is both in uplift and extension (Figure 3.1). Deep earthquakes occur along some portions of the NA chain, reaching maximum depths of about 90 km (*De Luca et al., 2009*). Tomographic studies reveal the presence of a westward dipping fast anomaly beneath the NA area, suggesting the sinking of a cold body into the mantle (*Lucente et al., 1999*). Regional tomographic results suggest thinner crust in the Tyrrhenian side than in the Adriatic one, associated with a small velocity jump at the Moho (*Di Stefano et al., 2009*). Low-seismic velocity in the uppermost mantle under Tuscany has also been suggested from surface wave studies (*Levin & Park, 2009*). Measures of SKS splitting in the area highlight a complex link between mantle flow under the NA and orogenic evolution (*Salimbeni et al., 2008*). An eastward retreating slab has been invoked as principal driving process in this area (*Malinverno & Ryan, 1986*), able also to describe the present position of the orogen, but hypotheses have been argued where this motion is a steady-state (*Faccenna et al., 2004*), or ongoing process (*Doglioni, 1991*).

Receiver Function (RF) analysis is a widely applied technique that uses *P*-to-*S* converted waves, generated at sub-surface seismic discontinuities, to map sharp lithologic contrasts at depth. Receiver functions are based on two simple assumptions. First, a plane P-wave which crosses a planar seismic discontinuity is (partially) converted to an S-wave. Second, for teleseismic P waves, source and path effects are recorded on the vertical Z component of the seismograms. Thus, a simple deconvolution of the horizontal components from the vertical gives rise to two time-series, a radial (Q-RF) and a transverse (T-RF), which contains the *P*-to-*S* converted waves beneath the receiver (*Vinnik, 1977; Langston, 1979; Levin & Park, 1998; Savage, 1998*). The Q-RF contains energy mainly from the isotropic seismic structure beneath the receiver, while TRF carries information primarily from the anisotropic and/or dipping subsurface structure. Q-RF analysis has been widely used to create images of subduction zones (*Ferris et al., 2003; Bannister et al., 2007; Kawakatsu & Watada, 2007; Piana Agostinetti et al., 2009*). Analysis of the energy on the TRF data-set is far less common. A large TRF data-set from a single seismic station has been used to image both anisotropic and dipping structures beneath the receiver (*Savage, 1998; Park et al., 2004; Piana Agostinetti et al., 2008c*). Harmonics coefficient analysis, involving both Q- and T- RF, has been developed for the analysis of

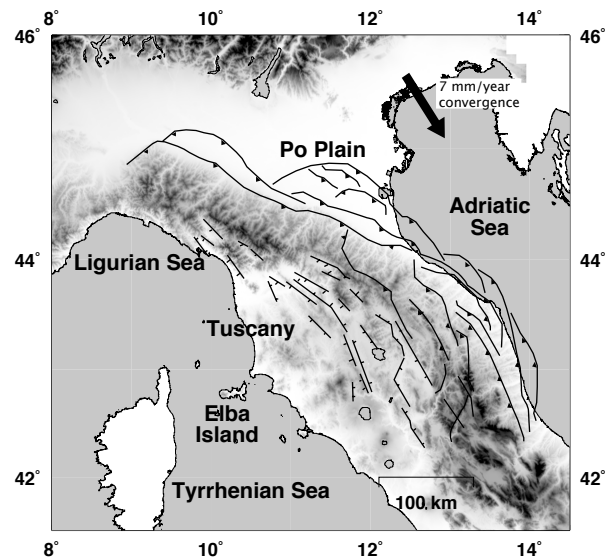


Figure 3.1: Tectonic sketch for the study area. Main tectonic boundaries are displayed outlining areas affected by compression and extension. The arrow indicates the convergence direction between Eurasia and Africa plate, almost parallel to the development of the compression/extension area.

## Mapping seismic anisotropy using harmonic decomposition of 36 Receiver Functions: an application to Northern Apennines, Italy.

subsurface anisotropy (*Girardin & Farra, 1998; Bianchi et al., 2008*) under isolated seismic stations. However, few imaging techniques, which use data from several seismic stations, join the analysis of the Q- and T- RF data-set (*Tibi et al., 2008; Mercier et al., 2008; Tonegawa et al., 2008*).

RF techniques have been applied to study the NA area. Moho depth in NA region has been estimated using both temporary (*Piana Agostinetti et al., 2002*) and permanent (*Piana Agostinetti & Amato, 2009*) seismic stations. A selection of the RETREAT data-set has been employed to estimate crustal properties, i.e. thickness and  $V_P/V_S$ , across the NA chain, using a simple grid-search approach (*Piana Agostinetti et al., 008a*). The anisotropic seismic structure of the forearc Adriatic crust has been studied in *Levin et al. (002a)*, while *Roselli et al. (2010)* investigated both isotropic and anisotropic structure of the Tyrrhenian crust in the fore-arc. Strong evidence of heterogeneity in the crust and upper mantle has been detected (*Piana Agostinetti et al., 008a*) under the NA chain, where the previous studies failed to clearly reveal the geometry of the subducted interfaces.

In this study, we apply a new technique for RF analysis which allows the separation of the back-azimuth harmonics of the Q- and T- receiver-function data-set as a function of the incoming wave-field direction. Energy due to anisotropic and/or dipping subsurface structures is separated from the isotropic signals, and partitioned in 2-lobed back-azimuth harmonics,  $\cos \phi$  and  $\sin \phi$ , which become the principal tool for the understanding of subsurface geometries. Data are stacked along profiles which image both isotropic and anisotropic structures. The input data for the profiles are obtained by a Common Conversion Point (*Dueker & Sheehan, 1998*) stack technique to focus our analysis between 20 and 70 km depth. In this chapter, we first describe the harmonic decomposition and the migration methods. Then, we present results from the analysis of the RETREAT data-set, and we discuss our method and the geodynamics implications of the results.

### 3.2 Data & Method

We use a dataset composed of about 13,000 RFs obtained from teleseismic records occurred at epicentral distance between  $30^\circ$  and  $100^\circ$ , and with  $M > 5.5$ , and selected by their high signal-to-noise ratio. Teleseismic events were recorded at 51 broadband, 3-component stations, deployed along peninsular Italy, between  $42^\circ\text{N}$  and  $46^\circ\text{N}$  (Figure 3.2). Forty stations were operating by RETREAT experiment for three years (10/2003 to 09/2006) (*Margheriti et al., 2006*). Ten stations are permanent seismic observatories of the Italian National Seismic network; and one station (VLC) belongs to the Mediterranean Network (MedNET). All stations recorded continuously between 2003 and 2006. Due to the long working period of the RETREAT array, we obtain a good back-azimuth coverage (Figure 3.3).

Seismic records are rotated into the LQT reference system to enhance the converted  $P_s$  phases. L is the direction of the hypothetical incoming P wave (computed using IASPEI91 model) and Q is perpendicular to L in the vertical-radial plane, i.e. the plane that contains source and receiver. T is normal to

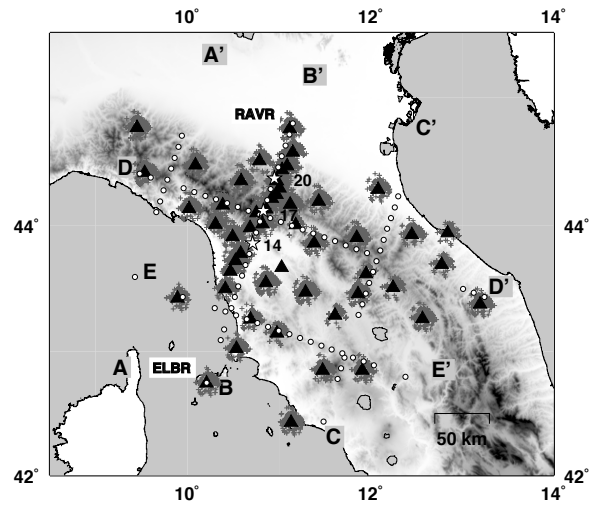


Figure 3.2: Map displaying stations (black triangles); piercing points (grey crosses) at 40 km depths for the events recorded at stations and used in this study. The map shows also the locations of 5 profiles, white dots represent the spots for which we estimated a Rf along profile directions. Spots 14, 17 and 20 in profile  $BB'$  are represented by stars. ELBR and RAVR stations (at the beginning and end of  $BB'$ ) are displayed.

**Mapping seismic anisotropy using harmonic decomposition of 38 Receiver Functions: an application to Northern Apennines, Italy.**

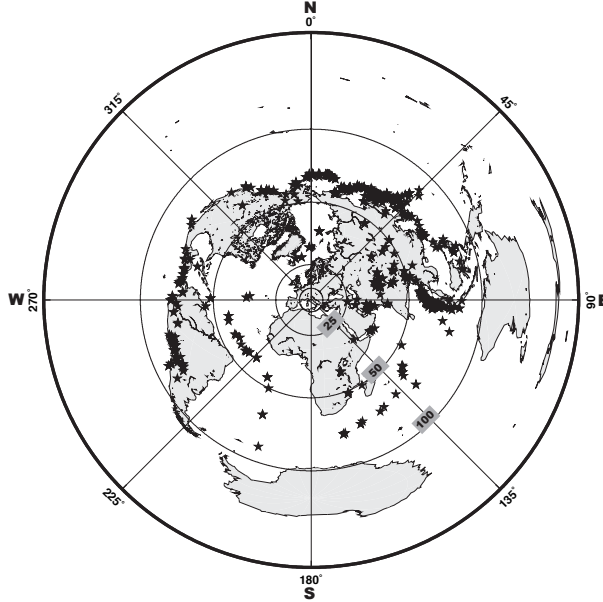


Figure 3.3: Black stars represent the location of teleseismic events recorded at Spot 17 in profile  $BB'$ . Numbers indicate back-azimuth  $\phi$  (rays) and epicentral distance  $\Delta$  (circles).

the L-Q plane. Receiver functions are calculated by frequency-domain inversion algorithm using multi-taper correlation estimate (*Park & Levin, 2000*). We use a frequency cut-off of 0.5 Hz, which gives us a vertical resolution of approximately 3 – 5km.

### 3.2.1 CCP and Migration

To enhance the continuity of the structures in the study area, we implemented a Common Conversion Point technique (*Dueker & Sheehan, 1998; Wilson et al., 2004*) (see also Supporting Material). We select five main profiles across Northern Apennines (Figure 3.2). Three profiles ( $AA'$ ,  $BB'$  and  $CC'$ ) share the same direction  $N18^\circ E$  approximately orthogonal to the strike of the Apennines orogen (in its northern part, between  $9^\circ E$  and  $13^\circ E$  longitude). Two profiles ( $DD'$  and  $EE'$ ) are orogen-parallel. For each profile, we divide the area within 40 km of the profile into rectangular boxes 20 km wide, with a 50% overlapping scheme (i.e. each area shares 50% of its surface with the adjacent areas). For each rectangular area, we select the ensemble of RFs (both Q and T) for which the surface projections of their conversion points at a fixed migration depth fall inside the rectangular area. We associate the RF with the center of the rectangular area (the 'spot', hereinafter). For our purpose, we migrate each RF using IASPEI91 model to 40 km depth (Figure S1). For each spot, we obtain an ensemble of Q-RF and T-RF which can be used to image the seismic

discontinuities at 20–70-km depth.

### 3.2.2 Harmonic analysis

Both Q and T components contain useful information about the subsurface structure. The isotropic part of the seismic velocity profile at depth mainly affects the Q-RF component, while anisotropy and dipping structures produce *P*-to-*S* conversion recorded on the T-RF component (Levin & Park, 1998; Savage, 1998). Here, we implemented a technique that allows analyzing both Q- and T-RF simultaneously. This characteristic is fundamental in complex tectonic settings, e.g. subduction zones, where both anisotropy and dipping layer have been observed, together with strong isotropic seismic velocity jumps. Our method is based on the extraction of the back-azimuth harmonics of a RF data-set as a function of the incoming P-wavefield direction. Here, we assume that an ensemble of RF can be expressed as a sum of  $\cos k\phi$  and  $\sin k\phi$ , where  $k$  is the harmonics degree and order, and  $\phi$  is the back azimuth. We limit our analysis to the first three degrees and orders, i.e.  $k = 0, 1, 2$ . Degree and order  $k = 0$  represents the bulk isotropic variation of the seismic velocities with depth (the ‘constant’ back-azimuth harmonic, hereinafter). For flat interfaces in isotropic media, the T-RF contribution vanishes and the signals are expressed on the  $k = 0$  back-azimuth harmonic of the RF data-set (i.e. a simple stack of the Q-RF components). The first and second harmonics,  $k = 1, 2$  contain the energy which displays a periodicity of  $2\pi/k$  with the back azimuth  $\phi$  of the incoming P wave. The 2-lobed periodicity is expected if a dipping interface or an anisotropic layer with a plunging symmetry axis is present at depth, while a 4-lobed periodicity is observed when the subsurface structure includes an anisotropic layer with horizontal symmetry axis (Maupin & Park, 2007). As clearly shown in Shiomi & Park (2008), for both periodicities, the Q- and T-RF back-azimuth harmonics display amplitude variability with the back azimuth  $\phi$  of the incoming P-wave, with a  $\pi/2k$  shift. Here, we give a brief description of the harmonic decomposition and we refer to the Supplementary Material (at the end of this chapter) for details. For  $k = 1, 2$ , we sum the Q- and T-RF back-azimuth harmonics with a phase shift of  $+\pi/2k$  to enhance the effect due to anisotropy or dipping interfaces (this combination is called Q+iT, hereinafter), while we sum the Q- and T-RF back-azimuth harmonics with a reverse shift (i.e.  $-\pi/2k$ ) to highlight the unmodelled component of our data-set, i.e. energy due to scatters or complex 3D heterogeneities. This component is called Q-iT, hereinafter. Then, the combined Q+iT and Q-iT back-azimuth harmonics are decomposed in their back-azimuth harmonics along two normal axes, N-S and E-W. For the 2-lobed patterns, the  $\cos \phi$  back-azimuth harmonic of Q+iT and Q-iT combinations has maximum absolute amplitudes for the Q-RF along a N-S axis, maximum absolute amplitudes for the T-RF along an E-W axis, in presence of a N-S dipping interface or anisotropic symmetry axis trending N-S. For the  $\sin \phi$  back-azimuth harmonic, the maximal directions of the Q-RF and T-RF are E-W and N-S, respectively for E-W oriented structures. This procedure allows to easily recognize both the presence and the orientation of anisotropic materials and planar dipping seismic discontinuity at depth. A similar approach has

## Mapping seismic anisotropy using harmonic decomposition of 40 Receiver Functions: an application to Northern Apennines, Italy.

been developed in *Girardin & Farra* (1998) and has been successfully applied to mantle wedge investigation (*Vinnik et al.*, 2007; *Piana Agostinetti et al.*, 008a).

Figure 3.4 shows the decomposition of the RF data-set for one spot, i.e. the 17-th spot along profile  $BB'$ , as an example. Top rows display the back-azimuth harmonics for 17-th spot that are constant with back azimuth  $\phi$ . Large pulses are present on the Q+iT plot, at about 3 and 6 s time delay, while the Q-iT part, which should be zero, displays limited energy, consistent with the imperfect back-azimuth coverage of the RF ensemble. Other rows in the figure contain the first and second harmonics. On the left, the second and third rows show the summation of the Q- and T- back-azimuth harmonics, with a  $+\pi/2k$  phase shift, for two normal directions (N-S and E-W, respectively). As explained above, this summation enhances  $P$ -to- $S$  conversions which display a  $2\pi/k$  periodicity as a function of back azimuth. Both  $\cos \phi$  and  $\sin \phi$  RF traces show energy in this harmonic, but  $\cos \phi$  signal seems everywhere stronger than  $\sin \phi$  suggesting a more N-S orientation of the symmetry axis of the underlying structure. On the right, the same second and third rows display the summation of the Q- and T- back-azimuth harmonic with a reverse phase shift, i.e.  $-\pi/2k$ , displaying signals given by structural lateral variations or scatter. Energy on the Q-iT plot is limited to the very shallow crust, while almost no energy is present at 0 – 4-s time delays, i.e. at mantle wedge depths. This demonstrates that the  $Ps$  scattering from mantle-wedge depths follows the predictions of simple models. (Scattering by structures in the uppermost crust, on the other hand, may be more complicated.) In the fourth and fifth rows, the  $k = 2$  back-azimuth harmonics are useful to understand if an anisotropic layer with horizontal axis is present (*Levin & Park*, 1997). In this study, we find limited energy on the  $k = 2$  back-azimuth harmonics at the frequencies used, therefore, we do not consider it further.

To assess the variance of the decomposed RF traces, we adopt a bootstrap approach, in which the full data set is resampled multiple times ( $> 100$  iterations) to determine the natural variability of parameters estimated from the full data set. The standard deviation of the stacked RFs are indicated by the light-green envelopes around the plotted RFs.

### 3.2.3 Symmetry directions

Comparing the signals in  $\cos \phi$  and  $\sin \phi$  back-azimuth harmonics for each spot, we extract information about the symmetry directions of the main features. Plotting the particle motion implied by the  $\cos \phi$  and  $\sin \phi$  back-azimuth harmonics of the RFs for selected time-windows gives the trend of apparent symmetry axes at depth. In Figure 3.5, we plot the particle motion for the 17-th spot along profile  $BB'$ , computed in the time-window between 0 and 5 s. The arrow direction represents the linear trend of the particle motion, estimated by a least-squares fit. Arrow length is proportional to maximum elongation in the particle motion plot in Figure 3.5. Here, we clearly observe a NNE direction, which could define both the trend of the symmetry axis of anisotropic materials at depth or the dip direction of a plunging seismic discontinuity.

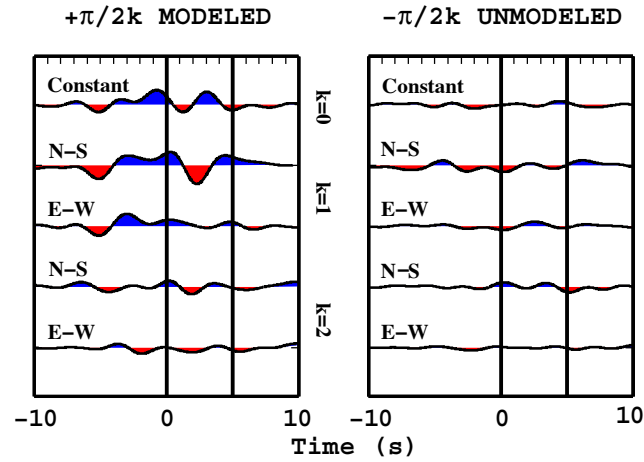


Figure 3.4: Example of back-azimuth harmonics decomposition for Spot 17 in profile  $BB'$ . Left panel for the “ $Q+iT$ ” component, right panel for the “ $Q-iT$ ” component. Constant term is the stack for all the events recorded at the spot. N-S and E-W labels indicate the  $\cos \phi$  and  $\sin \phi$  harmonics terms, respectively. The labels  $k = 0, 1, 2$  indicate the harmonics degree and order.

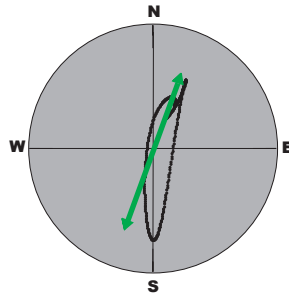


Figure 3.5: Particle motion obtained for the 0–5 s time-window, relative to the 40-km target migration delth, at spot 17 (black line). The green arrow displays the linear trend of the particle motion.

### 3.2.4 Modeling

To interpret the observed RFs along the different profiles, we produced a set of synthetic RF traces using simple models. We created synthetic records using the RAYSUM code (*Frederiksen & Bostock, 2000*) which models the propagation of a teleseismic wave through a stack of anisotropic layers separated by planar dipping interfaces. For each spot, the procedure previously described for the computation of the observed RF traces is applied to a distribution of teleseismic rays similar to the observed one, to produce the synthetic RF traces. Synthetic and observed RF traces are compared to retrieve the gross seismic structure along a profile. While qualitative information about subsurface geometry are easily deduced from the raw comparison of observed and synthetic RF traces, a more sophisticated inversion scheme would be needed to estimate the elastic properties along the profile.

## 3.3 Results

### 3.3.1 Harmonic analysis

We apply the procedure for the decomposition described above to each profile (Figure 3.2), to reconstruct the subsurface features across the study area. For each profile, we plot three sweeps which contain the constant, the  $\cos \phi$  (N-S) and the  $\sin \phi$  (E-W) parts of the decomposition. Positive/negative amplitudes are shown as blue/red pulses in the RF traces. Due to the overlapping scheme adopted here, the trace at each geographical spot shares data only with its immediate-neighbour spots, and the RF traces are migrated in the depth-domain (Figures 3.6-3.10) using the CCP computation and migration model (Figure S1). However, as previously stated, our strategy focuses the RF in the 20–70-km depth interval.

We analyze profile  $BB'$  which crosses the Apennines along a dense line of seismic stations, so that its spots are estimated from a larger number of RFs than the other profiles. Later, we extend our observation to the other profiles, to find correspondences and variations of the main features across the study area.

Profile  $BB'$  (Figure 3.7) is 270 km long and comprises data from ELBR station (Isola d'Elba, Tyrrhenian sea) to RAVR (Ravarino, Po Plain). RF traces at individual spots are estimated from at least 120 distinct event-receiver combinations, i.e. teleseismic records. Large amplitudes are present both on the constant and  $\cos \phi$  back-azimuth harmonics, while the  $\sin \phi$  back-azimuth harmonic displays lower amplitude than the other two. The delay time in the plots is referenced to the migration target at 40-km depth, so that pulses at negative delay time correspond to interfaces shallower than 40 km. Two main features are present in the constant harmonic. A positive phase starts at  $-2$  s in the westernmost part of the profile and ends at  $-1$  sec at  $X = 170$  km, i.e. under the crest of the chain. Another well defined positive phase shows up in the Adriatic side displaying a dipping behavior towards SW direction, i.e. its arrival time changes from 0 s in the easternmost side ( $X = 240$  km) to 6 s at

about  $X = 130$  km. On the  $\cos \phi$  plot, we observe that strong energy, displayed as a double negative/positive pulse, is present where the two pulses described above overlap. Arrival time of this double pulse grows toward SW. Profile  $AA'$  starts from the Ligurian Sea, and ends at the (suggested) trench (Figure 3.6). It displays the same features described for profile  $BB'$ , with the exception that here the signal looks cleaner and less noisy. We recognize a well-defined pulse present in the SW part of the profile at about  $-1.5$  s, and disappearing under the crest at about  $X = 100$  km. A pulse, which displays an increasing delay time toward S-W, appears in the NE side at  $1.5$  s, and it is present along the profile until the Tyrrhennian coast. Also, the  $\cos \phi$  back-azimuth harmonic displays features similar to profile  $BB'$ , i.e. the double dipping phase.

Profile  $CC'$  runs parallel to profile  $AA'$  and  $BB'$ , but does not cross normal to the trench due to the local curvature of the chain (Figure 3.8). We highlight a positive pulse shallowing from  $-0.5$  s on the Tyrrhennian coast line, to  $-1.5$  s at about  $X = 130$  km, on the constant back-azimuth harmonic. On the Adriatic side, a dipping positive pulse appears from  $3.5$  s (at  $100$  km) to  $0.5$  s at roughly  $X = 140$  km and then flattens until  $X = 210$  km. For this profile the segment where the two pulses overlap is shorter ( $< 50$  km) and suggests a NE orientation, because the amplitude is roughly equal on the  $\cos \phi$  and  $\sin \phi$  back-azimuth harmonics.

Profiles  $DD'$  and  $EE'$  parallel the orogen in its northern part, departing from it at the southern end (Figures 3.9 and 3.10). Due to their geometry, we expect complex patterns in the pulses identified on the orogen-normal transects. For profile  $DD'$ , we observe two pulses almost along all its length, on the constant back-azimuth harmonic. Because the Apennines deflect to the south and this profile aligns N108°W direction, the earlier pulse at  $-1.5$  s is lost near  $X = 120$  km, and see the later phases which seems to shallow. The  $\cos \phi$  back-azimuth harmonic exhibits the double pulse highlighted in the previous profiles near the Apennines crest, but the  $\sin \phi$  back-azimuth harmonic displays some energy from  $X = 0$  to about  $X = 210$  km. Variation in the anisotropic orientation would be consistent with this behavior. Profile  $EE'$  runs along the Tyrrhennian side and ends near the orogens. We only observe a sharp pulse at  $-1$  s, and no energy appears in our targeted time window between  $0$  and  $4$  s on the  $\cos \phi$  and  $\sin \phi$  back-azimuth harmonics.

We summarize our observations. The constant back-azimuth harmonic is influenced mainly by the isotropic seismic structure. Relative to our targeted  $Ps$  conversion depth of  $40$  km, we find an earlier positive pulse in all profiles between  $-1.5$  and  $0.5$  s, mainly along the Tyrrhennian side but displaying variable expression toward the mountain chain. We associate this arrival with a positive velocity jump (i.e. a seismic discontinuity where velocity increases with depth) at relatively shallow depth. Tyrrhennian Moho has been previously imaged as a shallow discontinuity in *Piana Agostinetti et al.* (008a). Our results confirm this hypothesis. The low amplitude of this  $Ps$  conversion along all the profiles suggests the presence of a small impedance contrast between the crust and the upper mantle in this area. We observe another positive phase, recognizable along all profiles which run into the Adriatic domain, in the  $0-6$  s time-window. This phase arrives progressively later from roughly E to W, dipping under the

Mapping seismic anisotropy using harmonic decomposition of  
44 Receiver Functions: an application to Northern Apennines, Italy.

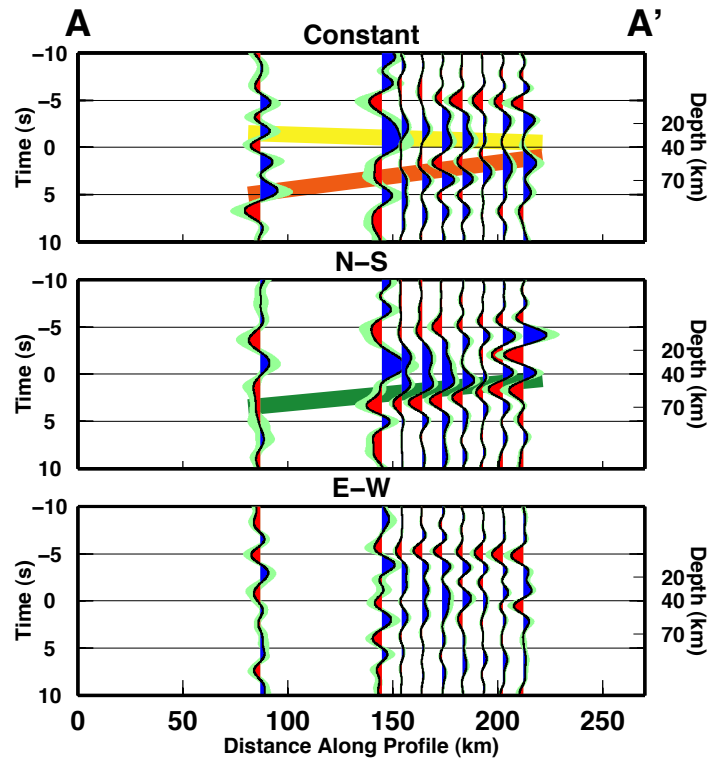


Figure 3.6: RF data-set along profile  $AA'$ , displayed as Constant,  $\cos \phi$  (N-S) and  $\sin \phi$  (E-W) back-azimuth harmonics. Blue and red pulses indicate positive and negative amplitudes, respectively. Colored stripes highlight the main features: yellow for the Tyrrhenian moho, orange for Adriatic moho and green for the 3D feature. X-axis shows distance along profile in km, Y-axis for the time (depth), in s (km).

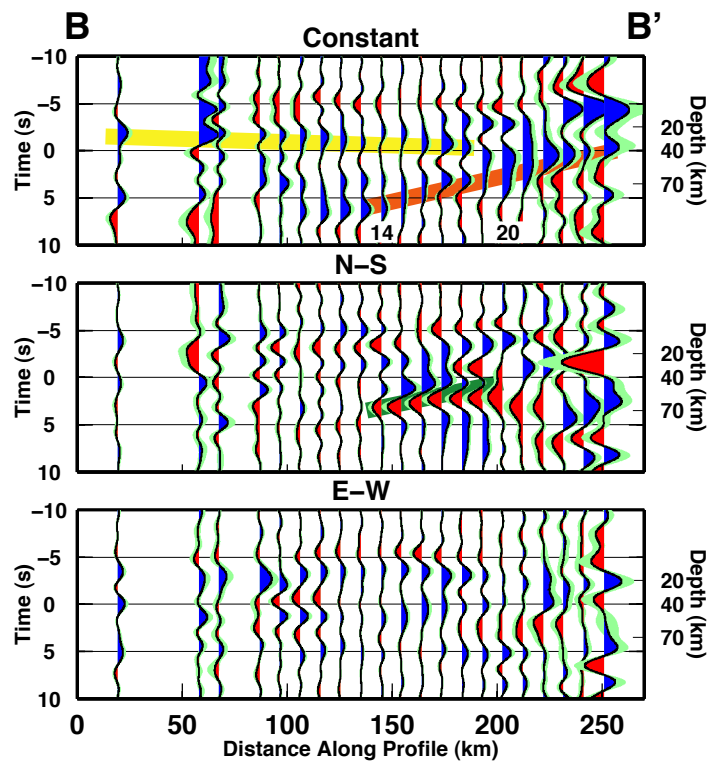


Figure 3.7: As in Figure 3.6, for profile  $BB'$ . Numbers below the traces indicate the spot numbers.

Mapping seismic anisotropy using harmonic decomposition of  
46 Receiver Functions: an application to Northern Apennines, Italy.

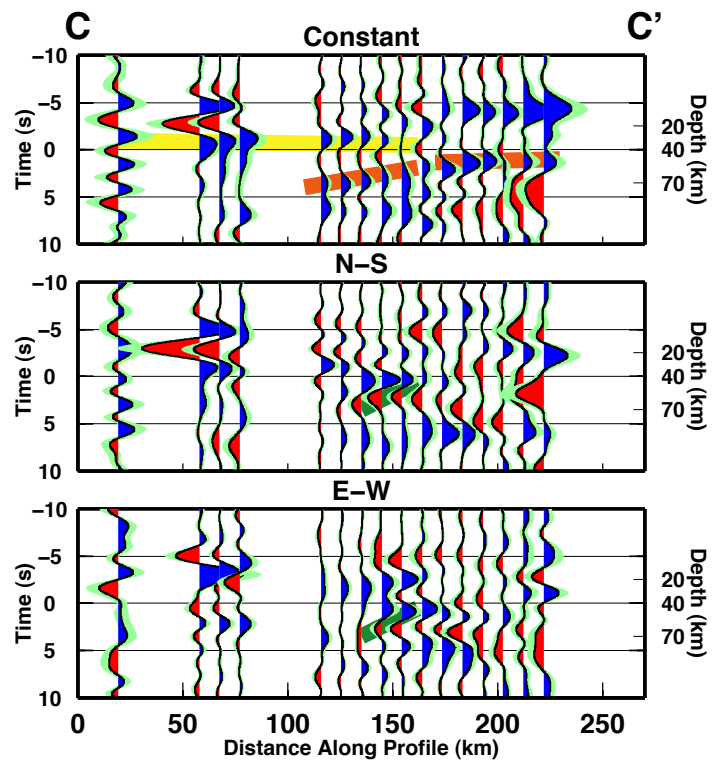


Figure 3.8: As in Figure 3.6, for profile  $CC'$ .

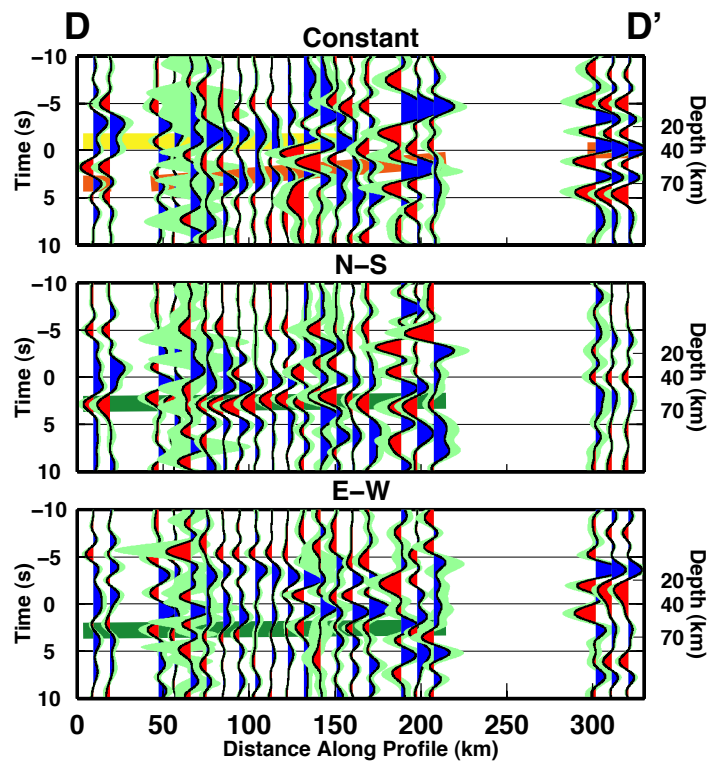


Figure 3.9: As in Figure 3.6, for profile  $DD'$ .

Mapping seismic anisotropy using harmonic decomposition of  
48 Receiver Functions: an application to Northern Apennines, Italy.

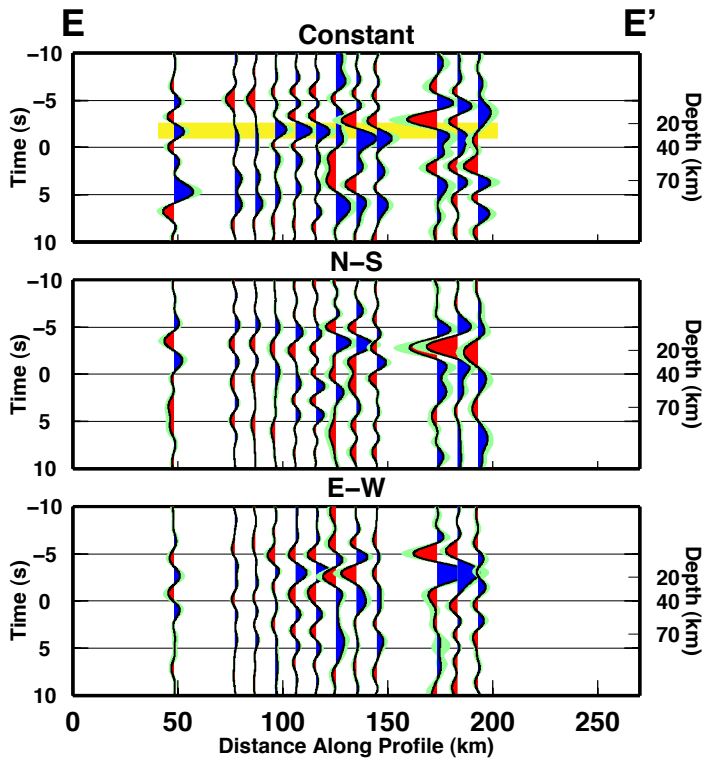


Figure 3.10: As in Figure 3.6, for profile  $EE'$ .

chain where it meets the earlier arrival from the Tyrrhenian Moho. We interpret this arrival as the  $P$ -to- $S$  converted phase from the Adriatic Moho. Adriatic Moho has been detected at 35 – 40 km, and in some cases as deep as 54 km depth, across the Apennines, in a neighbouring area (Roselli *et al.*, 2008). In the Adriatic foredeep, the depth of this interface is debated (Piana Agostinetti *et al.*, 2002; Levin *et al.*, 2002a). So we recognize the presence of the two domains Tyrrhenian and Adriatic already identified by (Pialli *et al.*, 1998) and (Pauselli *et al.*, 2006) .

Looking at the  $\cos \phi$  and  $\sin \phi$  plots gives us constraints on the 3D structure under this area. In general, the Tyrrhenian domain displays smaller amplitude in the  $k = 1$  harmonics  $\cos \phi$  and  $\sin \phi$  at our migration depth (40 km). A strong double phase is seen along all the chain where the two positive pulses overlap for the constant back-azimuth harmonic. This double phase seems to dip under the chain from the Adriatic toward the Tyrrhenian sea. While the above observations on the constant harmonic mainly confirm previous estimates of the crust-mantle boundary across the study area, the presence of the double-pulse  $Ps$  phase, suggesting a layer trapped between two discontinuities, represents a new feature. We interpret this feature as defining a third structural zone along the Apennines, between the Tyrrhenian and the Adriatic, and here identified as Overlapping domain. Using this definition, we map the three areas in Figure 3.12. Moreover an additional analysis for profile  $BB'$  (Figure 3.11), where the focus of the migration is at 80 km depth, clearly shows that the double phase on the  $\cos \phi$  plot disappears at about 80 km depth (at  $X = 120$  km along profile  $BB'$ ). A double phase dipping toward SW on the  $\cos \phi$  and  $\sin \phi$  plots could be related to two main features: (1) two parallel dipping interfaces; or (2) a single anisotropic dipping layer. In the first case, the observation of the double phases needs the presence of two strong seismic discontinuities both at the top and bottom interfaces. This model would also generate a dipping double phase on the constant back-azimuth harmonic, where we only find one positive pulse. On the other hand, the second case does not produce a double phase on the constant harmonic, if a weak seismic contrast is associated with the top interface. So, we interpret the double phase in the  $\cos \phi$  and  $\sin \phi$  harmonics as an anisotropic layer which dips into the upper mantle toward the SW, roughly beneath the Apennines crest.

### 3.3.2 Symmetry direction

Following the approach described in the previous section, we obtain a symmetry direction for almost all the spots of each profile, corresponding to the major subcrustal  $Ps$  conversions at our target depth. To highlight continuity of the pattern across all the study area, we recompute four more profiles, which run in-between the other profiles, with a 50% overlapping scheme. In Figure 3.12, we plot all the directions found, together with the extension of the three zones defined above: Tyrrhenian, overlapping and Adriatic. The length of the arrow is proportional to the amplitudes of the pulses on the  $\cos \phi$  and  $\sin \phi$  plots. Well-defined patterns are present in the map, e.g. from the 14-th to 20-th spot along profile  $BB'$ , that allow us to draw interesting observations. First,

Mapping seismic anisotropy using harmonic decomposition of  
50 Receiver Functions: an application to Northern Apennines, Italy.

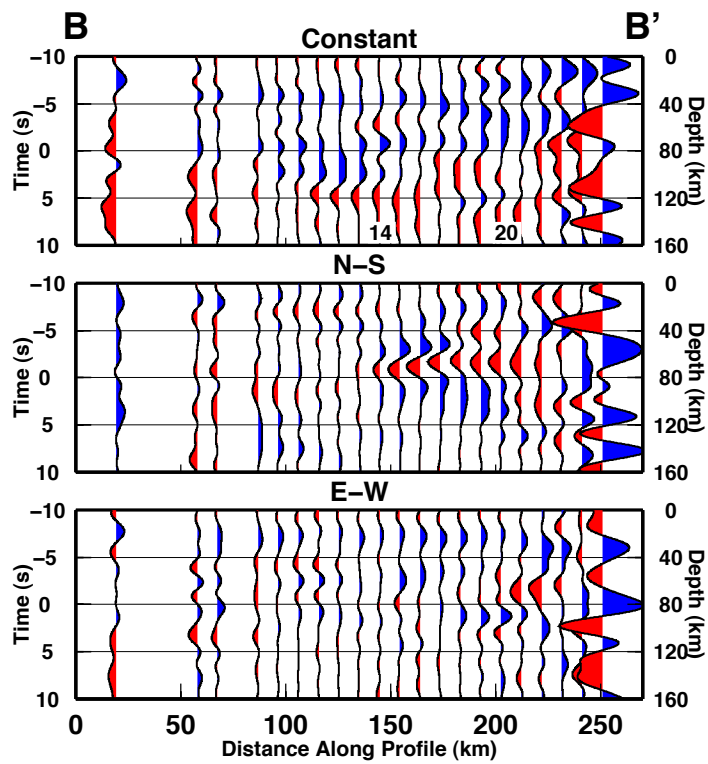


Figure 3.11: As in Figure 3.7, RF are migrated to 80 km depth.

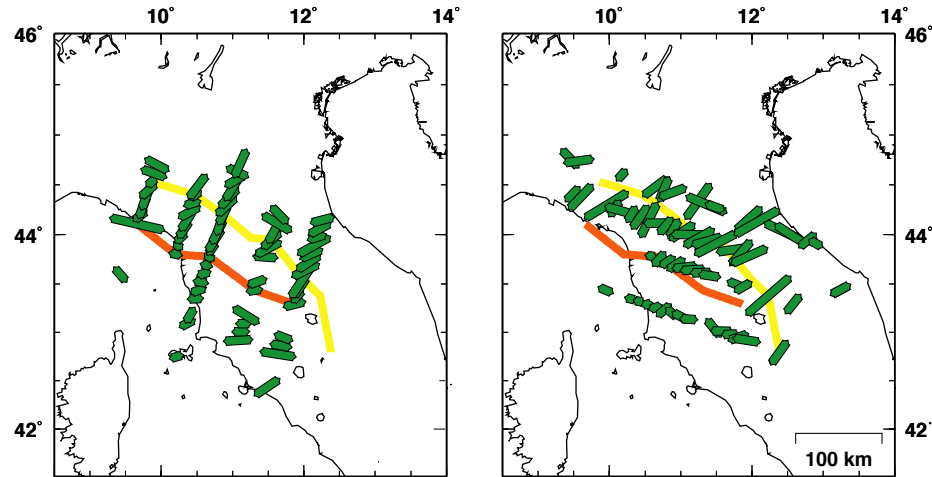


Figure 3.12: Maps displaying the symmetry directions (green sticks as green arrow in figure 3.5) obtained along the profiles; on left side for profiles normal to the Apennines orogen, on right side for profiles subparallel to the Apennines. Yellow line represents the easternmost boundary of the Tyrrhenian Moho; orange line represents the westernmost boundary of the Adriatic Moho achieved by Figures 3.6-3.10.

we notice that in the Overlapping zone anisotropy axes have almost the same direction. In particular the portion of this zone in which the horizontal distance between the two Mohos is larger, symmetry directions are consistent and display a NNE general trend. Where two Mohos are closer (SE portion of the area) symmetry directions are less uniform. Along the Tyrrhenian sea symmetry axis are relatively shorter than close to the mountains. Their direction pattern is towards SE. On the Adriatic side, symmetry axes do not display a unique orientation. They twist towards NW in the northern part and towards NE and seldom SE in the southern part of the area, describing a fan-like pattern.

### 3.3.3 Modeling

All observations drawn in the previous section need to be integrated in a model of the seismic structure across the study area, which can be discussed and compared to structures found in previous studies, or hypothesized by geodynamic models. Thanks to the observations on the data-set we are able to define three models, each corresponding to the three illustrated zones (Figure 3.13). Computed synthetics (Figure 3.14) give a good representation of the observed RF traces. The main features are shown by the cartoon in Figure 3.13: (a) a flat shallow Moho in the Tyrrhenian side, (b) a dipping and deeper Moho in the

Mapping seismic anisotropy using harmonic decomposition of 52 Receiver Functions: an application to Northern Apennines, Italy.

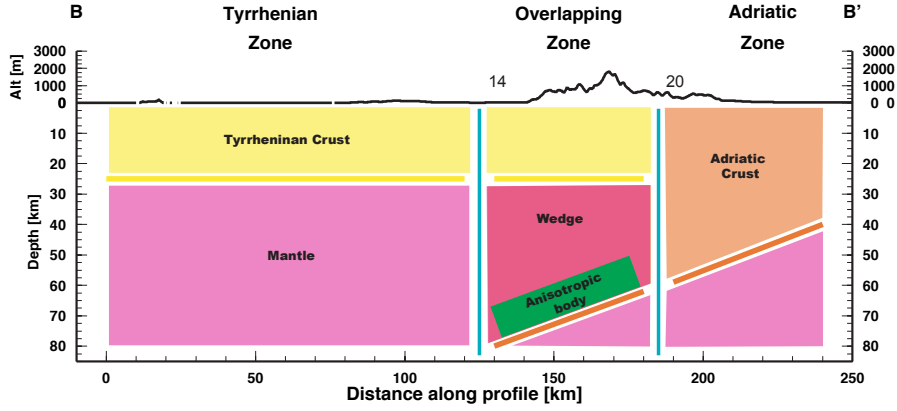


Figure 3.13: A 2D schematic representation of the structures inferred along profile  $BB'$ . The profile is divided into the three zones which boundaries are represented by spots 14 and 20.

Table 3.1: Seismic velocity (km/s) for models in Figure 3.14

Tyrrhenian			Overlapping			Adriatic		
Type	Thick (km)	Vs	Type	Thick (km)	Vs	Type	Thick (km)	Vs
Crust	25	3.4	Crust	25	3.4	Crust	58-40	3.4
Mantle	Halfspace	4.1	Wedge	38-21	3.8	Mantle	Halfspace	4.1
			Anisotropic Layer	15	3.8			
			Mantle	Halfspace	4.2			

Adriatic side and (c) a shallow and a deeper Mohos, both present, together with an anisotropic layer above the deeper discontinuity, in the overlapping area. Velocities used to compute RF traces in Figure 3.14 are presented in Table 5.1. The anisotropic layer in the overlapping zone is modeled using hexagonally anisotropy with a dipping symmetry axis. The axis displays a  $N32^\circ E$  trend and plunges by  $20^\circ$  from the horizontal. The layer has 4% P and S anisotropy. In the overlapping and Adriatic zones, the deepest interface is dipping  $20^\circ$  toward SSW, representing the dipping Moho of the Adriatic plate.

### 3.4 Discussion

In this work, we implemented a new method to image the northern Apennines subduction zone. We investigated teleseismic receiver functions using a CCP

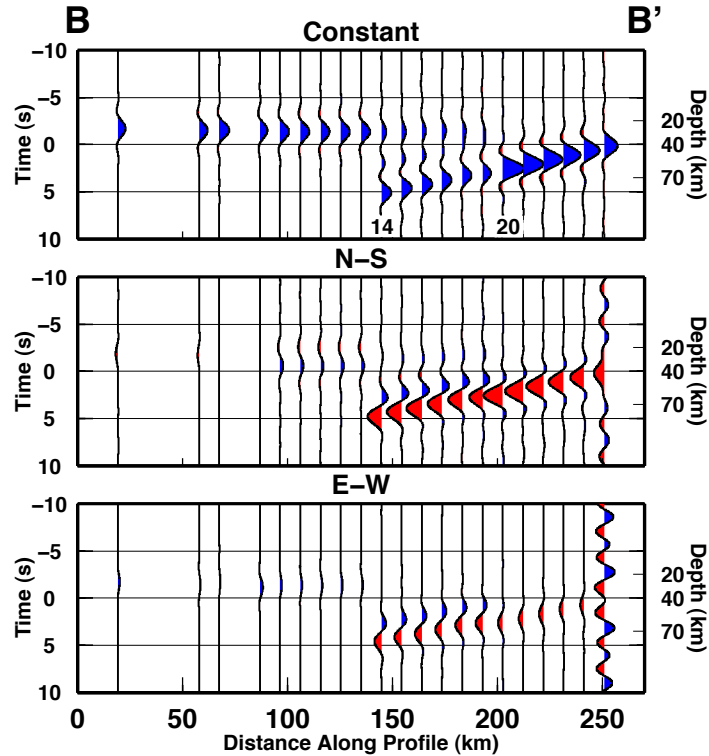


Figure 3.14: As in Figure 3.6, but for synthetic RF data computed from the models illustrated in Figure 3.13.

procedure with the aim of creating 2D profiles of the subsurface structure. The recovered radial and transverse receiver functions are used to create three back-azimuth harmonics for each profile representing both isotropic and anisotropic structures. We divide the northern Apennines into three zones, Tyrrhenian, Adriatic, and Overlapping, on the basis of their seismic characterization, and to resolve the anisotropic features. We model the three zones with simple velocity structures to represent the main features highlighted in the RF gathers. The three models together delineate a realistic explanation of subsurface structures and produce a synthetic data-set similar to the observed (Figure 3.13).

Our results for the Tyrrhenian side show a simple layer-over-half-space structure, where the main features of our data-set confirms the presence of a flat horizontal discontinuity at about 25 km depth, possibly associated to the Moho discontinuity; also this feature slightly deepens towards the foreland, and this is the same attitude highlighted by active seismic studies (e.g. *Franco et al.*, 1998; *Barchi et al.*, 1998). Our simple modeling approach does not allow us to investigate the strength of the seismic velocity jump associated with this discontinuity, and our migrated sections do not demand strong anisotropy in the uppermost mantle beneath this shallow interface. For the Adriatic side, the application of

## Mapping seismic anisotropy using harmonic decomposition of 54 Receiver Functions: an application to Northern Apennines, Italy.

our method gives new important insights to the subsurface seismic structure. A clear picture of the downgoing Adriatic Moho is retrieved. Classical RF analysis involving only the RRF data-set did not clearly image this discontinuity (*Piana Agostinetti et al.*, 008a). Single station analysis suggests the presence of dipping boundaries beneath the foreland of NA subduction (*Piana Agostinetti & Amato*, 2009), but differences arise for the Moho depth along the Adriatic coast (*Piana Agostinetti et al.*, 2002; *Levin et al.*, 002a), while some similarities come from the comparison with the thermo-mechanical model from (*Pauselli & Federico*, 2002). Many of the previous studies were deployed along the CROP03 profile, which is located at the southern end of the area investigated in this chapter, giving anyway a similar picture of these two interfaces' geometry (*Barchi et al.*, 2006, and references therein).

The main finding of this analysis is the evidence and the clear definition of the Overlapping domain, i.e. where both Tyrrhenian and Adriatic Mohos are present. Moho doubling in the study area has been suggested in (*Ponziani et al.*, 1995) for a limited part of the NA chain, but clear evidences of such structure were lacking. Our analysis allows us to localize the overlapping area in detail, both its lateral extension and the separation between the two interfaces. More, our harmonic decomposition points out the presence of an anisotropic body trapped in between the two Mohos and the symmetry axis analysis allow us to confirm the coherence of anisotropic directions in the surrounding rock masses. The anisotropic body is characterized by significant anisotropy and regionally coherent orientation. In the Overlapping zone, the anisotropy directions show coherent NNE trend (i.e. almost trench normal), rotating toward SW-NE further south in the orogen and suggesting a relationship between the anisotropic direction and the stress field in the downgoing crust. On the other hand, in the NE side of the orogen, the anisotropic axes display a fan-like pattern probably indicating a SW-directed flow, while on Tyrrhenian side anisotropy directions form a less coherent pattern.

The nature of the anisotropic body is not completely revealed from our simple analysis and modelling, but a comparison with other studies helps to identify promising hypotheses. Shear-wave birefringence in the region (*Plomerova et al.*, 2006; *Salimbeni et al.*, 2007, 2008) shows a spatial pattern of anisotropic fast axes for SKS waves that disagrees with the symmetry-axis orientations we infer at the top of the subducting Apennines lithosphere but that show backazimuthal dependence for Tyrrhenian and Adriatic domain; moreover the observed variations of fast axis directions with backazimuth in the Adriatic domain lead to the hypothesis of a multilayered anisotropy (*Salimbeni et al.*, 2008, 2009). Receiver functions and shear birefringence are sensitive to different spatial scales of the anisotropy, so a discrepancy does not imply conflicting interpretations. Rather, it highlights the complexity of deformation beneath the northern Apennines and opens the possibility of the presence of at least two anisotropic layers. The anisotropic signals we observe with receiver functions are generated by sharp contrasts in rock texture, typically within 5 – 20 km layers, and would lead to small ( $< 0.5$  s) birefringence time delays. Because birefringence time delays  $\delta t \simeq 1$  s accumulate as shear phases travel upwards through a substantial thickness of deformed rock, the northward twist in fast-axis orientation beneath the

Apennines from orogen-parallel to nearly orogen-normal has been attributed to either a pre-existing mantle-lithosphere fabric (*Plomerova et al.*, 2006) or sub-slab asthenospheric flow associated with incipient slab detachment (*Salimbeni et al.*, 2007; *Levin et al.*, 2007). The orientation of the symmetry axis in the portion of our cross-Apennines RF transect where anisotropy appears strongest (from the Apennines crest to central Tuscany) is roughly north-south, and lies within a region where the birefringence fast axes are trending NW to WNW from stations at the Apennines crest to stations in Tuscany.

Disagreement between the anisotropic orientations inferred from shear-wave birefringence and teleseismic receiver functions was reported in Tibet (*Levin et al.*, 2008), in Cascadia (*Park et al.*, 2004; *Nikulin et al.*, 2009), and in Kamchatka (*Peyton et al.*, 2001; *Levin et al.*, 2002b). Better agreement with RF anisotropy is found for the birefringence of slab events in Kamchatka, which are insensitive to deeper deformation within and beneath the slab (*Levin et al.*, 2004).

The degree of anisotropy in our models is greatest between 40 and 80 km depth, in a thin layer at the inferred top of the downgoing Apennines slab. The geometry suggests that this depth interval is where the slab first encounters supraslab mantle, near the so-called mantle nose, where stresses in simple corner-flow models are infinite. We note that strong slabtop anisotropy has been inferred at roughly 40-km depth in other subduction-zone locales: Cascadia (*Nikulin et al.*, 2009) and the Kii Peninsula, Japan (*Shiomi & Park*, 2008). For both locales Ps converted-wave amplitude appears weaker or absent for the slab interface at depths much greater than 40 km, in contrast to the Apennines slab in this study. A difference in anisotropic character may indicate a distinct Apennines subduction dynamic or a distinct slab-top lithology. The coincidence of high slab-top anisotropy and non-volcanic tremor in Cascadia and southern Japan suggests dehydration of a hydrous lithology, which in Cascadia may include the antigorite polymorph of serpentine (*Nikulin et al.*, 2009). In the northern Apennines, our data analysis does not demand the lower  $V_P$  and higher  $V_P/V_S$  ratio of a serpentinite layer, so other factors should be considered.

It is simplest to associate anisotropy at the slab top with shear-coupling between the slab and the overlying mantle, but recent compilation of subduction-zone studies argue against simple corner-flow models (*Long & Silver*, 2008). *Katayama & Karato* (2006) argue that many puzzling aspects of anisotropy in subduction zones can be related to factors that influence crystallographic transitions between modes of olivine deformation. *Kneller et al.* (2005) argued from geodynamics modelling that subduction zones should exhibit a partial decoupling from the mantle nose to the depth beneath the line of arc volcanoes. *Abt et al.* (2009) argue that such decoupling is necessary for the maintenance of along-trench flow consistent with trench-parallel birefringence fast-axes in Costa Rica. *Pinero-Feliciangelia & Kendall* (2008) detect weak supraslab birefringence at many locations in the Caribbean, consistent with the partially-decoupled *Kneller et al.* (2005)'s hypothesis. (*Kawakatsu & Watada*, 2007) attribute a weakening in Ps converted-wave amplitude at roughly 50 km depth in Japan to slab dehydration and mineralogical transitions. Strong slabtop anisotropy in the northern Apennines persists to 80 km depth, which suggests

## Mapping seismic anisotropy using harmonic decomposition of 56 Receiver Functions: an application to Northern Apennines, Italy.

that its expression of anisotropy differs from typical subduction zones.

Geodetic observations for the northern Apennines (*Serpelloni et al.*, 2005) indicate that ongoing compression at the Po-Valley thrust front is weak, and net convergence across the Apennines orogen is cancelled by extension in the "back-arc" region of Tuscany. Absent or weak convergence across a nominal subduction zone opens the possibility for a post-subduction delamination (e.g. *Gogus & Pysklywec*, 2008) to explain the synconvergent extension and uplift of central Italy. In this context the slab-top anisotropic layer that we detect could be associated with a boundary layer of highly deformed peridotite induced by the extreme stresses associated with lithospheric detachment. More speculatively, the layer could be the precursor of a ultra-high pressure (UHP) unit of metamorphosed crustal rocks or partially serpentinized mantle rocks, caught in the subduction channel, but buoyantly rising toward the surface. Geodynamic models for this process are consistent with the UHP rocks forming a deformed layer atop the downgoing slab during a continental collision (*Warren et al.*, 008a,b). Within our field area, the Alpi Apuane marbles were subjected to lower-crustal metamorphism (15 – 30 km at 20 Ma) and have been exhumed from 9 km depth since 10 – 13 Ma (*Fellin et al.*, 2007). The Apennine orogen is relatively young; deeper exhumation is found nearby in the Alps (*Skemer et al.*, 2006; *Federico et al.*, 2007; *Jung*, 2009), an older zone of continental collision. Further study of this deep anisotropic feature will be necessary to determine if it indeed represents a future exhumed terrane.

### 3.5 Conclusion

In this chapter, we present a new methodology for the analysis of RF data-sets and we test it on a large teleseismic data-set collected across the northern Apennines orogen (Italy). The method successfully exploits the information contained in both radial and transverse receiver functions giving better constraints on the subsurface seismic structure than classical receiver function analysis. The harmonic decomposition is used to retrieve the isotropic structure under the seismic stations and to focus on buried anisotropic bodies. Using a CCP approach, we are able to image the lateral continuity of such anisotropic bodies at depth and to map the anisotropic axis directions across the whole study area.

The application of this new technique to the RETREAT data-set improves the knowledge of the uppermost mantle structure in the Northern Apennines area. The new analysis of the RF data-set defines an area along the Apennines chain where the Adriatic and Tyrrhenian Moho discontinuities appear to overlap. An anisotropic body is found trapped between these two discontinuities. The anisotropic axis of this body is trench-normal oriented, so that we identified a rotation of the axis from NNE to NE as the Apennines strike turns toward South. The layer could be subducted crust, but the depth extent of its apparent anisotropy is greater than other subduction zones, suggesting that a more complex origin has to be considered. Here, we hypothesize that the anisotropic body is the remnant of the delamination of the Adriatic microplate lower crust, which follows the complete subduction of the oceanic lithosphere.

## 3.6 Supporting material

### 3.6.1 Migration

To construct 2D profiles and highlight the main features of the subsurface structure we developed a procedure based on migration and stacking, at a common conversion depth (CCD), of the vertical-shear (Q) and transverse-shear (T) receiver functions (RF). Figure S1 describes an example of the migration technique for three RFs, and displays how the migration helps to focus wave energy to a desired depth. In panel (a) the delay time is referenced to the direct-P wave arrival, so that  $t = 0$  corresponds to the arrival direct- $P$  itself. The strongest later signals arrive a roughly  $t = 5$  s delay time, after which the RF becomes smoother. The CCD on which we focus lies at 40-km depth, germane to lower-crust/upper-mantle interaction, and because at this depth we find a strong signal on the Q+iT component. As we show on Figure S1, panel (b), the P waves are hypothetically converted into S waves at an interface located at 40 km depth. Rays coming from different epicentral distances are adjusted to be stacked together without modelling the time delay for the Ps phase at different conversion points along the interface. In Panel (c) we show the  $V_p$  and  $V_s$  models that we used to determine CCDs. These velocity models are obtained from the average crustal velocity model of *Christensen & Mooney (1995)*, grafted with the mantle from the PREM velocity model (*Dziewonski & Anderson, 1981*). Velocity jumps in the model crust occur every 10-km depth, with Moho at 30 km to match the average for the Italian peninsula. Mantle velocities increment by small steps every 10 km as well. Panel (d) shows the result of migration. The starting QRFs are now referenced to 40-km depth, so that  $t = 0$  s delay time targets a Ps converted wave from this level. Comparing panel (a) containing RFs before migration, and panel (d) with RFs after migration, some differences in the phase amplitudes are evident. In fact the targeted Ps pulse in the data-set is higher after CCD stacking. Also, the timing of adjacent pulses are better defined with respect to targeted Ps conversion, and show a higher amplitude, indicating that CCD stacking highlights the deeper structure. In this study we show RFs migrated at 80 km depth for BB' profile on Figure 11, the  $V_p$  and  $V_s$  model used for migration is the same in Figure S1. The analysis of it shows that the main 3D features of the data-set are confined above 80 km depth.

### 3.6.2 Decomposition of the seismic signal

In this section we describe how the energy of the seismic signal is organized after the harmonic decomposition with back-azimuth  $\phi$ . The harmonic components are estimated by numerical regression of QRFs and TRFs in a way to isolate the effects of isotropic and anisotropic seismic structures. The back-azimuth pattern of RF amplitude from both anisotropic and dipping subsurface structures is similar with this technique, but distinct from RF signals from flat-layered isotropic structure (*Maupin & Park, 2007*). It is possible to estimate the dip angle from the small  $\phi$ -dependent moveout associated with a dipping interface (*Shiomi &*

## Mapping seismic anisotropy using harmonic decomposition of 58 Receiver Functions: an application to Northern Apennines, Italy.

*Park*, 2008). We have not incorporated this secondary moveout effect, because interface dip is apparent from the migrated RF transects. Three-dimensional features beneath central Italy influence our data-set in different ways that depend on the back azimuth  $\phi$  of the arriving  $P$  wave. The decomposed seismic signal is displayed for three components of the harmonic decomposition in  $\phi$ : (1) the term constant with back-azimuth  $\phi$ , (2) the  $\cos\phi$  term, in which maximum RF amplitude occurs for N-S back azimuth and RF amplitude vanishes at E-W back azimuth, and (3) the  $\sin\phi$  term, in which maximum RF amplitude occurs for E-W back azimuth and RF amplitude vanishes at N-S back azimuth. Harmonics expansion in back azimuth  $\phi$  can discriminate the orientation of the structures near the target depths of the migrated RFs (in most cases, here, the target is 40-km depth).

As described in *Shiomi & Park* (2008), stacking of the Q-RF and T-RF with  $\phi/2$  shift in back-azimuth enhances the back-azimuth dependance of the  $Ps$  pulses. here, linear regression of the Q-RF and T-RF is computed as follow. Given  $N$  couples of Q- and T-RF, for each time  $t$ , the coefficients of the  $\cos k\phi$  and  $\sin k\phi$ , with  $k = 0, 1, 2$ , terms is computed solving the linear system:

$$\begin{pmatrix} Q_1(t) \\ \dots \\ Q_N(t) \\ T_1(t) \\ \dots \\ T_N(t) \end{pmatrix} = \begin{pmatrix} 1 & \cos \phi_1 & \sin \phi_1 & \cos 2\phi_1 & \sin 2\phi_1 \\ \dots & \dots & \dots & \dots & \dots \\ 1 & \cos \phi_N & \sin \phi_N & \cos 2\phi_N & \sin 2\phi_N \\ 0 & \cos \phi_1 + \pi/2 & \sin \phi_1 + \pi/2 & \cos 2\phi_1 + \pi/4 & \sin 2\phi_1 + \pi/4 \\ \dots & \dots & \dots & \dots & \dots \\ 0 & \cos \phi_N + \pi/2 & \sin \phi_N + \pi/2 & \cos 2\phi_N + \pi/4 & \sin 2\phi_N + \pi/4 \end{pmatrix} \begin{pmatrix} A(t) \\ B(t) \\ C(t) \\ D(t) \\ E(t) \end{pmatrix},$$

where  $\phi_i$  is the back-azimuth of the  $i$ -th couple of Q- and T- RF.  $A(t)$  represents the Constant part of the RF data-set, while  $B(t)$  and  $C(t)$  are the  $\cos \phi$  and  $\sin \phi$  terms analysed in this study. The coefficients  $D(t)$  and  $E(t)$  are the  $k = 2$  harmonics.

Figure S2 displays examples of harmonics decomposition for different 3D models: An isotropic model with one interface at 40 km depth (first column): the signal is on the constant component, while N-S and E-W harmonic components are flat, as we expected for an isotropic structure. An isotropic model with one dipping interface at 40 km depth (second column): the constant component displays less amplitude than for the model in the first column, because some of the converted-wave energy is expressed on both the Q and T horizontal components, rather than only the Q component (the SV receiver function). Model with one anisotropic layer at depth, with a fast symmetry axis and oriented N30°E plunging 20° (third column): Energy distributes among all three harmonic terms, larger on the  $\cos\phi$  expansion term (max RF amplitude at N-S back azimuth) than on the  $\sin\phi$  expansion term (max RF amplitude at E-W back azimuth) because the symmetry axis aligns closer to the NS direction. Model with one anisotropic layer at depth, with a slow symmetry axis trending N210°E with plunge 70° (fourth column): this model geometry resembles closely the fast-axis model above. In fact, the main difference between the anisotropies is the fast or slow nature of the intermediate axis, which lies in the horizontal plane normal to both the fast and slow symmetry axes. The correspondence

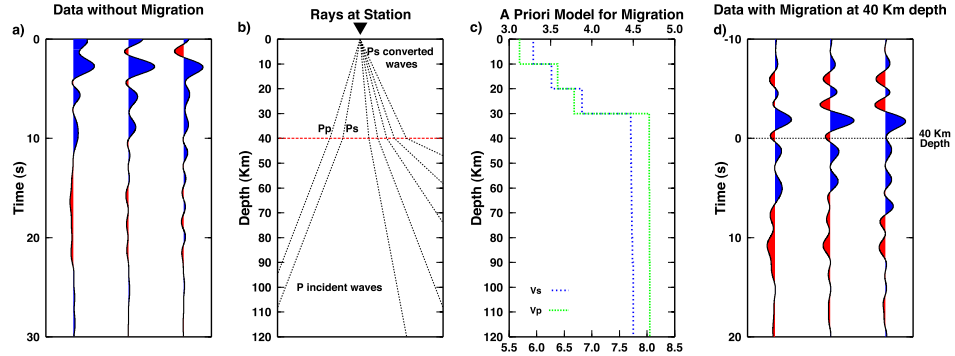


Figure 3.15: (a) Three example RRFs before migration. (b)  $P$  waves incident on an interface at 40 km depth and converted into  $S$  waves. (c) A-priori model used to migrate the RRFs. (d) Data migrated. The 40-km depth correspond to 0 s time.

between the computed RRFs for fast and slow anisotropy axes for this matched set of opposite trend directions and complementary plunges, highlights the ambiguity of discriminating the two types of anisotropy. Based on the first-order back-azimuth variation of RRFs in a typical data set, there are often two valid interpretations of the anisotropy, one with a fast axis and one with a slow axis, but at right angle to each other. Given this ambiguity, the researcher must add information, such as the likely lithology and style of deformation, to constrain the exact anisotropic geometry. Model with one anisotropic layer at depth with horizontal symmetry axis (fifth column): the RRF amplitude is on mainly expressed on the constant component, while  $\cos\phi$  and  $\sin\phi$  expansion terms have weak amplitude. In contrast to the phenomenon of shear-wave birefringence, anisotropy with a horizontal symmetry axis has relatively weak expression in receiver functions.

Mapping seismic anisotropy using harmonic decomposition of 60 Receiver Functions: an application to Northern Apennines, Italy.

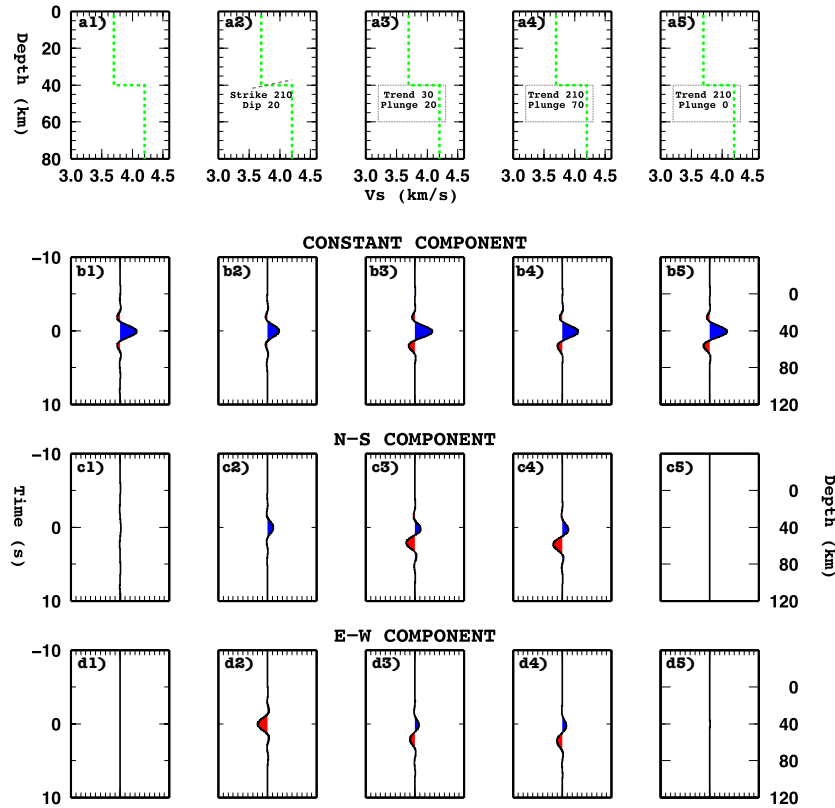


Figure 3.16: Harmonic decomposition for 5 different 3D models: (1) Isotropic Model with one interface at 40 km depth. (2) Model with one dipping interface at depth, with N210°E dip direction. (3) Model with one anisotropic layer at depth, with fast symmetry axis trending N30°E and plunging 20°. (4) Model with one anisotropic layer at depth with slow symmetry axis trending N210°E and plunging 70°. (5) Model with one anisotropic layer at depth with a horizontal symmetry axis. (a1-5) Velocity models for the 5 examples (b1-5) Constant component of harmonic expansion in  $f$  for the respective models. (c1-5)  $\cos\phi$  harmonic component (max RF amplitude at N-S back-azimuth) for the respective models. (d1-5)  $\sin\phi$  harmonic component (max RF amplitude at E-W back-azimuth) for the respective models.

## Crustal thickness variations and seismic anisotropy in Southern Apennines (Italy) from receiver functions.

We investigate crustal structure of the southern Apennines (Italy), through the use of receiver function (RF) data. We analyze a set of about 2300 RF computed using teleseismic events recorded at 14 broadband seismic stations. The study region is characterized by crustal complexities and intense tectonic activity and has been theatre of large and destructive earthquakes. These complexities are reflected in the computed receiver functions. However the large data-set analyzed and the technique adopted for the analysis allowed us to reconstruct the structure of the crust to some degree of detail. At shallow depth our analysis, accordingly with previous studies, reveals a crustal structure formed by basin sequences and flysch units overriding limestone of platform origin. From the crustal thickness determined beneath each station we can reconstruct the Moho geometry in the region. Major finding of this study, is the presence of a strong anisotropic (up to 10 – 12%) layer in the middle crust, as most of the computed RFs show clear polarity reversal with azimuth at 3 – 4 s, corresponding to a depth of about 20 km. Anisotropy axes in this layer display almost uniform SW-trending plunges beneath the Apennines belt, coherent with the plate motion, but for few stations it veers off. We interpret this layer as the transition between the lower and the upper crust. We infer that its strong anisotropic signature is due to the texture acquired by the rocks behaving plastically under the rigid movements of limestones platforms during the Plio-Pleistocene collisional phase which lead to the growth of the Apennines.

### 4.1 Introduction

To determine the depth, the nature and the structural properties of the transition between Earth's upper and lower crust is a difficult target for seismological investigations. Local seismicity is generally confined above this transition and not directly illuminates it, while waves from teleseismic events have limited resolution power on small scale crustal features because of their longer wavelength,

furthermore they also carry information from the deeper Earth. A seismological quantity, which can be diagnostic of the rocks texture, hence of their compositional attributes and of the past (inherited) and present tectonic loads, is the seismic anisotropy. At shallow crustal depths seismic anisotropy is possibly caused by the presence of stress-aligned micro-cracks or stress-opened fluid filled cracks and fractures within the rocks (*Crampin, 1978*). At deeper levels, the most likely cause of seismic anisotropy is the presence of preferential alignments of anisotropic minerals (*Rabbel & Mooney, 1996*). The most common tool for inferring the presence of seismic anisotropy along a seismic ray path is the measurement of the shear wave splitting, a similar phenomenon to the optical birefringence. However, for the above reasons, is difficult to distinguish the contribute of the lower crust to seismic anisotropy from that of the Earth's mantle by means of teleseismic shear waves splitting observations. In this study we apply a technique, which allows to detect and constrain the presence and the properties of anisotropic levels through the whole crustal thickness, by the use of Receiver Functions (RF) data. We apply this technique to a data set of about 2300 RF computed at 14 broadband seismic stations located in southern Apennines. The crustal structure of southern Apennines is well known down to 4 – 6 km depth thanks to the intense hydrocarbon exploration (i.e. *Mostardini & Merlini, 1986*). Southern Apennines are made up of a series of structural units resulting from the deformation of the Apulian margin and progressively overthrust and piled up towards the Adriatic in the Tortonian-Upper Pliocene time. The geologic structure of the southern Apennines is controlled by the geometric relationship of different paleo-geographic domains. These are: 1) the Latium-Abruzzi domain made of carbonatic platform depositional sequences; 2) the Molise domain characterized by platform, transition and basin deposits and messinain flyshes; 3) the Sannio Domain, made of basin units owing to the Lagonegro unit (see *Lentini, 1979*). The regional structural style is determined by a thrusts system characterized by internal units overriding the Adriatic foreland. From paleomagnetic analyses the differential rotations of structural rigid blocks has been individuated as the principal deformation mechanism in this area (*Mattei et al., 1993*, and references therein). A 3D P-wave velocity model of the upper crust beneath the Sannio area has been presented by (*Chiarabba & Amato, 1997*), showing strong velocity anomalies in the shallow crust related to lithological heterogeneities between limestone's of carbonate platform and basinal sequences, which characterize the Southern Apennines. Also the Moho depth has been detected by the application of several direct and indirect methods (*Scarascia, 1982; Piana Agostinetti & Amato, 2009*), while the middle and lower crust have been poorly investigated. In this study we perform a structural model of the crust from its shallow part to the mantle transition, paying major attention to the middle crust characteristics.

## 4.2 Data and method

We use teleseismic data collected during the 2005 – 2008 years by 14 seismic stations belonging to the Italian National Network (INGV). Digital seismic sta-

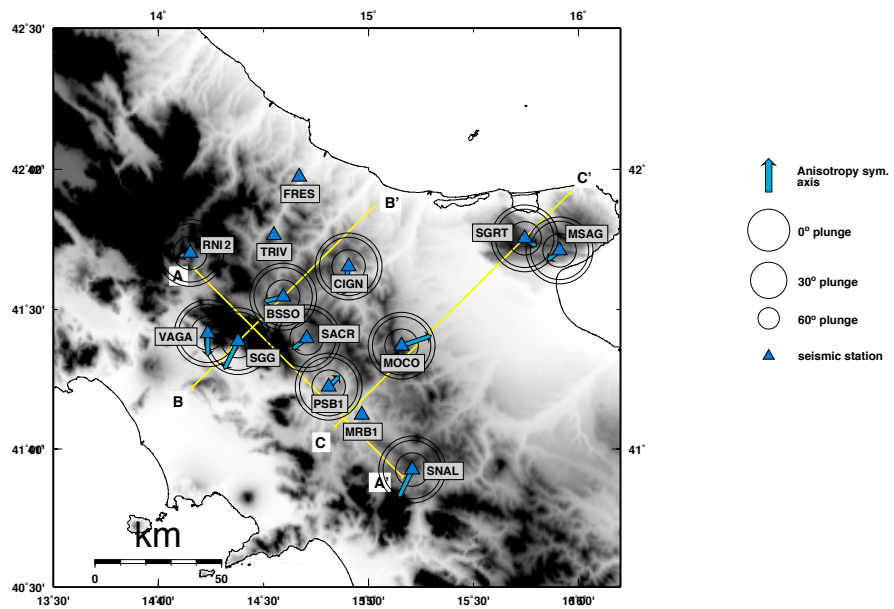


Figure 4.1: Map of the study area displaying the location of the seismic stations. In this map the profiles traces (in yellow), and the retrieved anisotropy axes (blue arrows) are shown. Circles represent the dip angle of the anisotropy axes.

tions were continuously recording and equipped with Lennartz 5s and Trillium 120s sensors. In this analysis, we used  $M_w \geq 5.5$  teleseismic events with epicentral distance between  $30^\circ$  and  $105^\circ$ . We obtained RFs deconvolving the vertical from the radial (R) and transverse (T) horizontal components (see *Langston, 1979*). RFs are calculated through a frequency domain deconvolution (*Di Bona, 1998*) using a Gaussian filter ( $\alpha=4$ ) to limit the final frequency band at about 2 Hz. A better signal-to-noise ratio is achieved by stacking the RFs coming from the same backazimuth direction ( $\Phi$ ) and epicentral distance ( $\Delta$ ). We performed the harmonic analysis in the same way we did for the Colli Albani example. We used an azimuthal filtering to isolate out the different periodicity of  $P_s$  converted phases (i.e. *Girardin & Farra, 1998*; *Bianchi et al., 2008*). The k0 harmonic (or stacked Radial) is the sum of all the RRFs and contains information on the isotropic structure underneath the station; the k1 harmonics reveal those features that have a periodicity equal to  $2\pi$ . Since a preliminary analysis of our data set revealed that the energy on the T component is considerable, we investigated the amplitude variations of the converted  $P_s$  phases on the R and T component with respect to  $\Phi$  variation, applying an azimuthal filter to our RF data-set, for both k0 and k1 harmonics, to eliminate the effects of noise and point out the presence of hexagonally anisotropy and dipping planar discontinuities. We extracted the k1 harmonics from the R (and T) data-set by summation of the components of individual RFs, and stacked the R and T distribution (R+T) to amplify the signal, in case of similarity between the two components (*Vinnik et al., 2007*). The analysis of R+T diagram is useful to highlight the axis of three-dimensional features. Among the 14 stations we face some different dataset which origin is due to both the recording time but also the quality of the recordings. In fact if some stations display good backazimuthal coverage, other show a poor coverage with lack of data for large gaps. In the first case the harmonics analysis and the recover of a 3D model is possible but it is not for the second case, for which we perform a 1D model.

### 4.3 Forward modeling

To detect into the space under the 14 stations we started a forward search made of two steps, and used similar inversion criteria for the whole area. A first search has been finalized to the definition of the shallow structures to 5–8 km depth, to recognise pulses included into first 2 seconds of the waveform, using a parameter space defined looking at geological sections published in *Mostardini & Merlini (1986)*. For all stations, polarity flips of pulses on both components, where interpreted as produced by dipping interfaces because of the noticeable presence, on the above mentioned sections, of dipping faults and thrusts involving the area and separating different domains, and because of a too big percentage of anisotropy (exceeding the maximum values reported in literature) should be recalled to match the direct P polarity inversion (*Lucente et al., 2005*). Then, velocity values where confined to find the carbonatic platform under one or two layers of allocthonous sediments, we focused in finding the top of the apulian platform by giving it S-velocity values included between 3.1 and 3.5 km/s,

with a  $V_p/V_s$  ranging into 1.85 and 1.95 values. In the following searches, we added, to these first defined strata, other levels to model the entire crust until the Moho. The apulian platform, which thickness varies between 6 and 12 km (respectively the known thickness, and doubled thickness), was not always considered as a unique homogeneous level but also involved into the thrust system or divided into smaller layers showing an internal gradient. Beneath this carbonatic body we needed to model a couple of pulses visible in each station dataset, between 3 and 4 s. An anisotropic layer can fit in a better way these two pulses than a dipping interface (reminding the ambiguous interpretation within receiver functions of the effects produced by them) (*Levin & Park, 1997, 1998; Savage, 1998; Bianchi et al., 2008*). To decide the quality of the symmetry axis we looked at some previous works as (*Sherrington et al., 2004; Leidig & Zandt, 2003; Levin & Park, 1997*), showing how symmetry effects brought by anisotropy are almost identical for negative or positive axis or at least hard to distinguish if not holding a complete backazimuthal coverage. We looked for the slow axis to understand the alignment of minerals. It is also unlikely that a region would contain one type of anisotropy, P or S, but not the other (*Levin & Park, 1998*), so we looked for an identical percent of P and S anisotropy. At the end, to define crust thickness we added a last interface to fit Moho pulse on R component, being at around 5 seconds of the waveforms.

## 4.4 Data-analysis and Results.

Among the 14 stations we face different data set, depending mainly on the location of the station. The bulk of the station is located in the central part of the area, where the thrusting system is very developed, affecting the structure and consequently the waveforms, making them highly noisy. A good example is given by SGRT, this station is located on Gragano (see Figure 4.1 for the location and Figure 4.2 for data-set), considered as flat foreland, out of the thrusting system. Moreover this station displays a complete back-azimuthal coverage and high data quality, allowing good results in the harmonics analysis. Another remarkable station, located on the central part of the area, is BSSO this has complete backazimuthal coverage too, but the complicated crustal structure reflects in its data-set making it less clear than SGRT's, anyway the 3D structure can be recovered. Stations like MRB1 instead have a bad data-set because of the shallow structure present very strong impedance contrasts that affect the entire waveform, because of this, we recovered just the 1D structure for these stations.

Here we show the results station by station. We start from a description of the 1D retrieved models and then will analyze the 3D models. Values for depths, velocities and 3D features are listed in Appendix A, synthetic and observed data-sets are in Figure 4.4 and Figure 4.5.

FRES: This station has strong monochromatic reverberations since it is located on a gypsum outcrop, although geographically is located on the eastern part of the Apennines chain. Under the gypsum we expect to find a simply shallow structure than in the other stations installed directly on the centre of

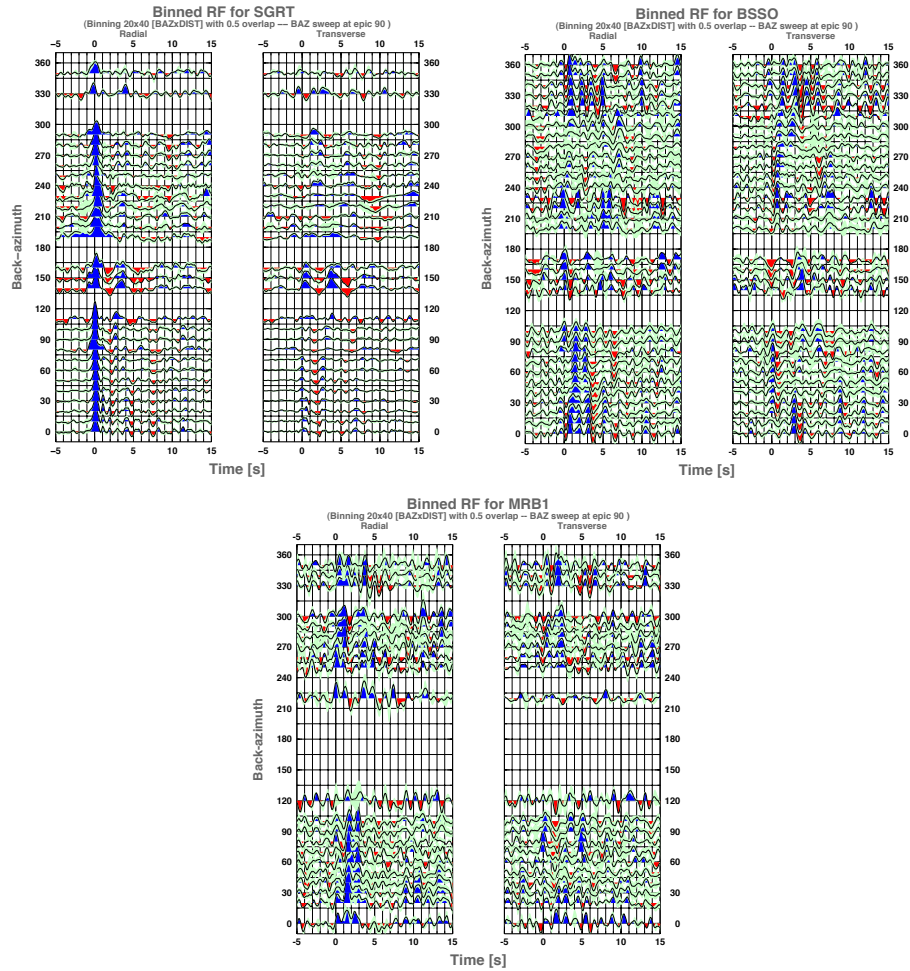


Figure 4.2: The complete data-set for three representative stations is shown. SGRT has a good backazimuthal coverage and good data quality. BSSO has good backazimuthal coverage but the RFs have high standard deviation (green color in the plot). MRB1 has low backazimuthal coverage and high standard deviation.

the chain. The reverberations do not allow the analysis of the T component, and we perform just the 1D structure for this site. The main positive pulses are located at about 0.5, 2 and 3 s, a negative phase is between 2 and 3 s. The recovered structure presents a strong impedance contrast at about 1.5 km depth, as bottom of the gypsum layer and top of the carbonates. Another positive jump is found at 2.5 km depth; a small decrease in the velocities is found at 7.5 km depth to the Moho, which is located at about 20 km depth.

TRIV: This station is located next to FRES, and shares with it the monochromatic signal. The position of the pulses and retrieved Vs model are similar to those of FRES too.

MRB1: This data-set shows a low P direct pulse, followed by a positive phase at 1.5 s and by a series of small positive pulses. The shallow velocity is very low because of the almost flat P direct pulse, a sedimentary layer is found below, while S velocities typical of limestones are found at about 3 km depth for 6 km thickness. Later Vs increases slightly, and also the Moho is not certainly defined.

Stations with 3D features.

Station BSSO was chosen as representative among the 3D stations, due to its large number of data covering almost the whole backazimuth directions and showing clear polarity flip between 3 and 4 s, and because it is one station with the simplest shallow structure. The initial parameter space for the very shallow crust is related to the geological section n° 10 of (*Mostardini & Merlini, 1986*), and data taken by Campobasso well; we knew a priori the existence of two layers upon the apulian platform. The first layer is made of the upper sequence of Lagonegro unit and Apennine's platform sediments, very low velocities and high  $V_p/V_s$  are required to it; the second one is made of the lower sequence of Lagonegro unit, its velocity is around 2.6 km/s, with high  $V_p/V_s$  values because of low compactness of sediments (*Improta et al., 2000*). From geological sections we know the existence of the apulian carbonate platform at about 8 km depth. For the next layers we had no more geological constraint, and filled the parameter space with three layers of upper, middle and lower crust using values of velocity, and density taken by (*Christensen & Mooney, 1995*); an average upper crust should have  $V_s$  values around 3.4 km/s, while for the middle crust values are around 3.7 km/. Energy on R+T defines the strong 3D crustal structure. There is a double phase in the first second and a double phase at 3 – 4 s. The first observation seems to point toward a shallow dipping layer model for the upper crustal structure, while the second is the anisotropy effect in middle crust. Summering, we need just one shallow dipping interface, dividing two sediments layers standing on Apulian carbonates to fit pulses into the first second. Between 3 and 4 s, is clear the effect of the anisotropic layer. Moho is at 32 km depth. (4.3).

RNI2: On Radial component P direct pulse is really low, and the most important feature is a positive pulse at about 1 s, while the correspondent on T comp shows a two lobed disposition for the same arrival times. We need two shallow dipping interfaces to fit P direct pulse polarity flip on R component, and pulses into first 2 s of the waveform on both R and T components. This dataset also shows a phase, on Radial and Transverse component, at 3 s, modelled with

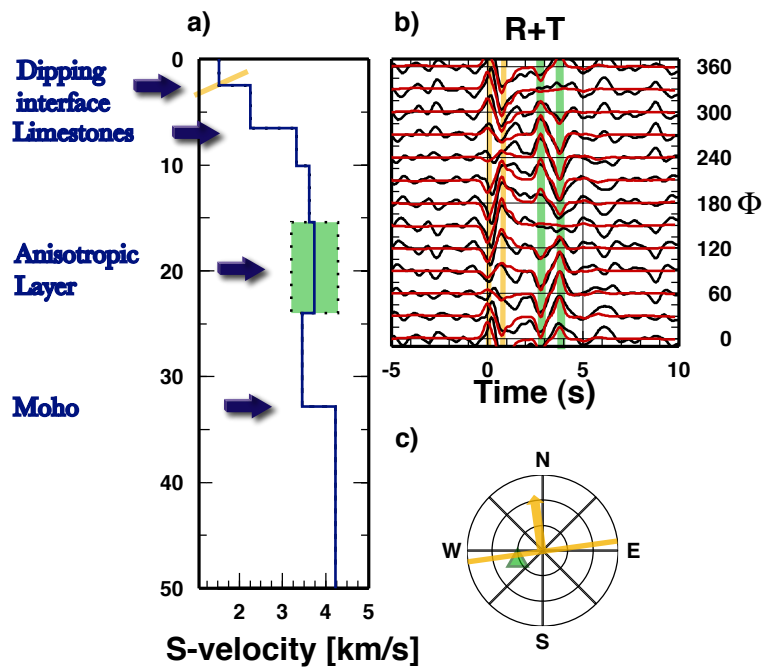


Figure 4.3: Station BSSO. (a) S-velocity model, displaying the location of the dipping layer (yellow line) and of the anisotropic layer (green rectangle). (b) Observed (black) vs synthetic (red) receiver functions, pulses given by the dipping layer and by the anisotropic layer are shown by yellow and green lines respectively. (c) Orientation of the dipping layer and of the anisotropic layer.

an anisotropic layer. The pulse at 6 s is the Moho interface located at 43 km depth.

VAGA: This station has two shallow dipping interfaces, and comparing results with geological sections we associate the first layers with Apennines' platform sediments in tectonic contact with Lagonegro sediments directly over Apulia platform carbonates; therefore the two dipping interfaces are interpreted as tectonic discontinuities among this three sediments layers. An anisotropic layer also in here fits those pulses on transverse component between 3 and 4 s. Moho depth is about 41 km.

SGG: There is a strong the 3D structure under this station. Pulses on the first second on T component can be the expression of dipping interfaces as seen in the geological sections. This station is near to VAGA, and in the same way, we used two shallow dipping interfaces to resolve the first second of the RFs, and an anisotropic layer fits pulses on 3 and 4 s. Moho depth is 39 km.

CIGN: This station displays a large double phase in the first 2 s, and some lower phases next in arrival times. Its Vs model has two dipping interfaces in the shallow crust and an anisotropic layer at about 12 km depth. Moho is at 34 km depth.

PSB1: A Ps converted phase is present around 1 s, another visible pulse is at 4 s, probably corresponding to the Moho discontinuity. From harmonics angular analysis we can define four pulses to interpret between 1 and 4 s in the data-set. Parameter space is, as for the other stations, defined to find the carbonates platform under two sediment layers, also in this case the two interfaces are inclined to model pulses into the first second; we find an anisotropic layer at 14 km depth. Moho is at 28 km depth.

MOCO: This station displays clear positive pulses at 2, 2.5 and 4.5 s, and a negative phase at 3 s. Again two shallow dipping planes are useful to interpret the shallow crust and an anisotropic layer is found at about 16 km depth. The Moho is at 36 km depth.

SACR: On R comp there is no P direct pulse, a positive feature is displayed at 1, 2.5 and 4.5 s. Energy on R+T plot gives confirmation of a 3D structure. Just one dipping interface satisfies the RFs in the first second. The anisotropic layer is found at 17 km depth. Moho depth is 24 km.

SNAL: The flat P direct in the stacked Radial component witness slow velocities in the upper structure, and the lack of clear phases on the waveform reflects the absence of strong flat interfaces, while there is some signal in the R+T plot. Two dipping interfaces reproduce the features in the first 2 s; an anisotropic layer at 20 km depth gives the feature at 3 – 4 s delay time. Moho depth is about 39 km.

MSAG: Geologic constraints and the cognizance of the near wells stratigraphy helped us in finding structures for the first layers. Foresta Umbra1 well is the nearest one and drills 3 km of neritic limestones and dolomites (J), and find the evaporitic formation of Burano Anhydrites (TR) until the bottom at 6 km (*Martinis & Pavan, 1967*). Sonic and stratigraphic logs from Gargano1 well witness a similar stratigraphy finding 2 km of limestones and about 2 km of anhydrites over the basement made of Verrucano formation and corresponding to a drop in  $V_p$  values (*Improta et al., 2000*). From deep seismic refraction

profile n° 10 from (Cassinis *et al.*, 2003), we have some suggestions about the whole crustal structure; in Gargano zone they find 3 layers in which  $V_p$  velocities are 6.8 km/s for the first 7.5 km, 6.7 km/s until 15 km, 6.3 km/s until 25 km depth, and then they find mantle velocities. The station is on the outcropping (cretaceous, neritic) carbonates, standing on a few km of triassic dolomites and anhydrites, which in our model are anisotropic. The anisotropic, middle-crust layer is found at 10 km depth. The Moho interface is at 30 km depth.

SGRT: This station is located on the Gargano, next to MSAG, and a simply structure is expected, since just the P direct pulse and the Moho pulse are present on its stacked Radial data-set. Some energy is found on R+T plot at 2 and 3 s, due to the anisotropic layer at 13 km depth. Moho is at 27 km depth.

## 4.5 Discussions

Our results confirm the previous studies for the detection of the top of the Apula carbonatic platform. It is in fact located from 1 to 8 km depth at the different stations deepening towards the higher crests according to the depths found in (Nicolai & Gambini, 2007). These depths are also justified by the intense thrusting of the units over the platform limestones. The main finding of this study is the clear Moho updoming in the center of the area, under the stations BSSO, CIGN, SACR and PSB1 (see appendix A and Figure 4.6. This shallow Moho has been detected previously in Piana Agostinetti & Amato (2009) and Di Stefano *et al.* (2010) at 25 – 30 km depth, where not a clear Adriatic Moho is subducting below the belt, and also this area is located over the slab window of central and southern Apennines. The common feature that we found for the stations in this area, is the anisotropic layer, located in the middle crust, at average 20 km depth. The anisotropic axes are mainly *SW* directed, differently inclined, and looking at the map-projection of the symmetry axes (Figure 4.1) some of them display a discordant orientation, but looking at the profiles in Figure 4.6, the symmetry axes display a clearer pattern. The slow symmetry axis, as we used in the models, are perpendicular to the foliation of the rocks. In the profiles in 4.6, the foliation suggested by the symmetry axes is drawn, and a Moho-like pattern of the anisotropic layer is clearly displayed. This anisotropic deformation is continuous underneath the seismic stations and is consistent with the dome-like crustal structure, probably working as decollement level between upper and lower crusts, a weak level noticed also in (Regenauer-Lieb *et al.*, 2006) able to accommodate the differential movements between the upper and lower crust. The geometry of the Moho and of the anisotropic layer suggest a geodynamic process active in which the Moho upraises probably pushed by the underlying mantle and by the slab detachment largely documented in this area (Lucente *et al.*, 1999). Meanwhile the differently oriented symmetry axes can be the expression of the differential block-rotation of the upper crust as seen in (Mattei *et al.*, 1993).

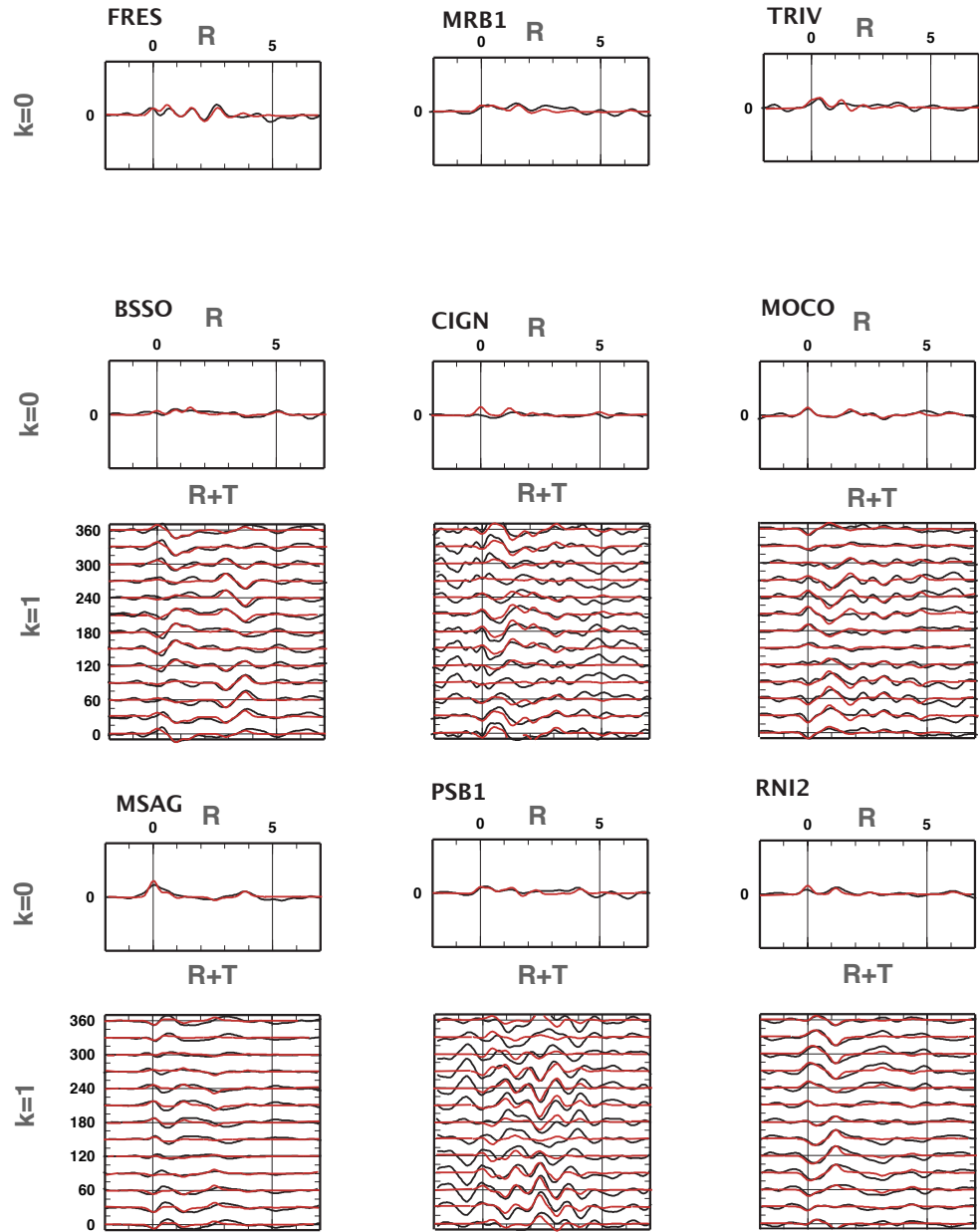


Figure 4.4: Observed (black) vs synthetic (red) receiver functions for the stations. K0 harmonics for stations FRES, MRB1 and TRIV. K0 and K1 harmonics for BSSO, CIGN, MOCO, MSAG, PSB1 and RNI2.

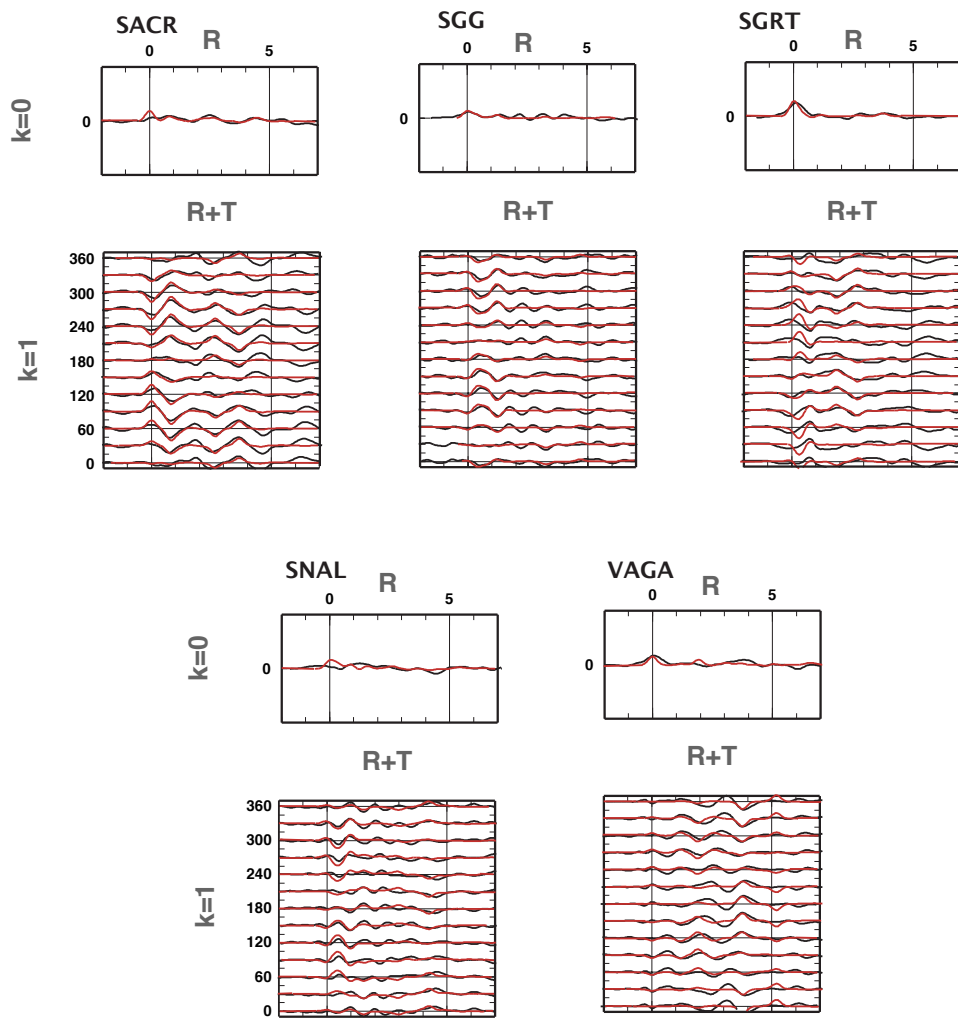


Figure 4.5:  $K_0$  and  $K_1$  harmonics for SACR, SGG, SGRT, SNAL and VAGA. Observed (black) vs synthetic (red) receiver functions.

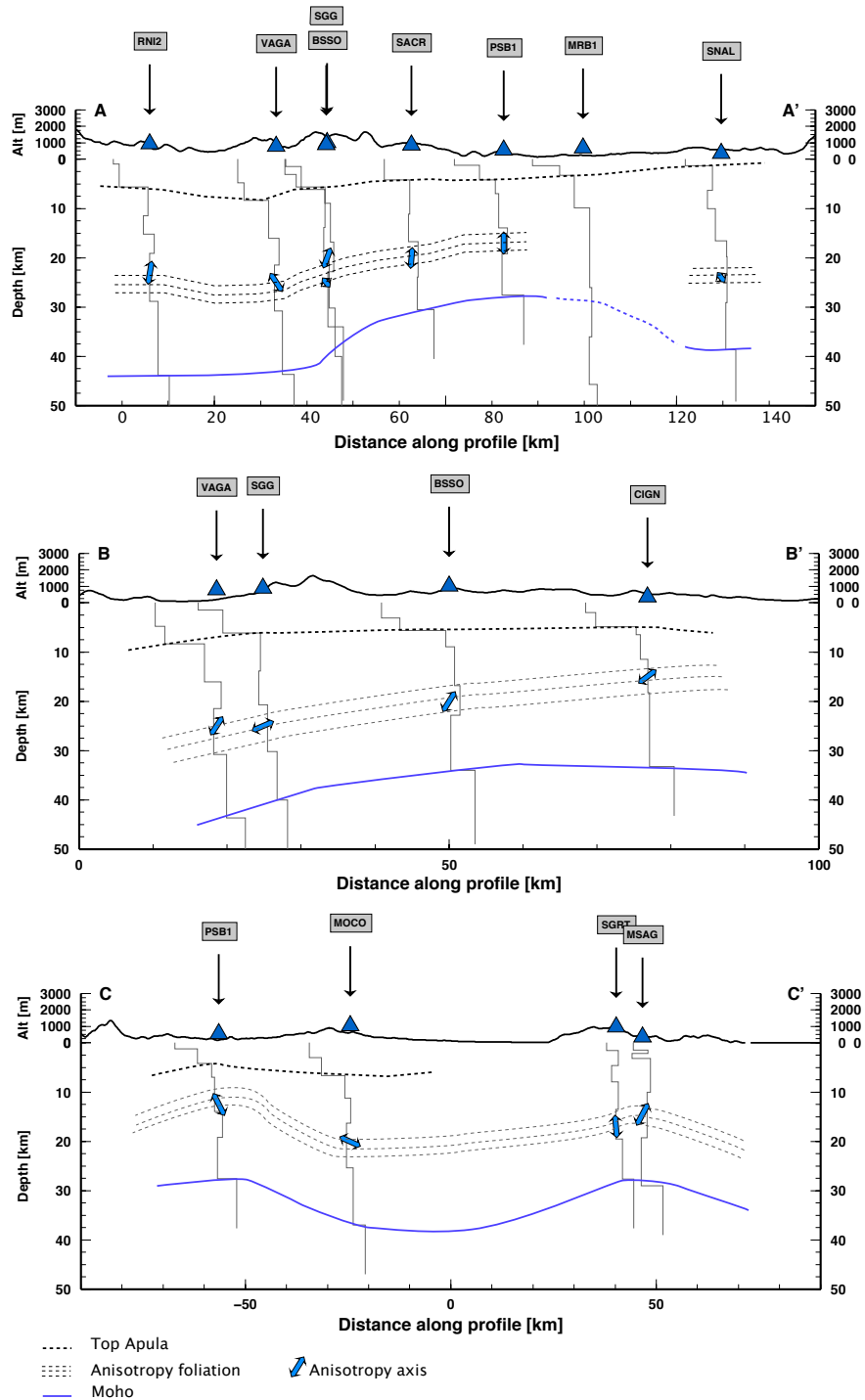


Figure 4.6: Along (AA') and across (BB' and CC') Apennines profiles; the Vs model for the seismic stations and the retrieved anisotropic axes are projected along profiles. Top of the Apulian platform is shown in thick dashed line, the foliation of anisotropic layer is displayed by light dashed lines. Moho depth is evidenced by the blue line.

## 4.6 Conclusions

In this chapter the Receiver Functions for 14 stations in the Southern Apennines have been analyzed with the aim of finding the crustal structure and the main crustal features in this area. Although noise and reverberations given by the very shallow and strong impedance contrasts affect the data set, the applied methodology allows us to achieve satisfactory results in the reconstruction of the main structural features of the crust. Detailed S-velocity models at depth have been found for the ensemble of the stations. In the retrieved models the presence of inclined structures and seismically anisotropic layers has been taken into account for a complete interpretation of the data. In most of the cases the location of the shallow discontinuities is in agreement with the presence of thrusts and faults found in previous studies. One of the main result of this study is the determination of the Moho geometry, which displays a dome-like trend, as it is shallow (28 km) in the central part of the study area, whereas it deepens peripherally (down to 45 km). A common feature has been found underneath the stations, consisting of an anisotropic layer at about 20 km depth, and displaying a *SW* general trend of its slow symmetry axes. We interpret the anisotropy found at this depth as caused by the foliation inside the layer separating lower and upper crust. This area of southern Apennines is located over a window of the slab running along the Apennines belt, and the crustal geometries revealed by this study could have implications on the geodynamics and on the tectonics of this region. We infer that here, because the slab has detached from its uppermost portion, the mantle relaxes upward possibly generating the dome-like geometry. The middle crust accommodates the differential movement between the lower crust and the rigid upper crust by flowing and deforming itself following the shaping of the Moho.

## Appendix A

**Custal thickness variations and seismic anisotropy in Southern  
Apennines (Italy) from receiver functions.**

Thick (km)	Vs km/s	Aniso %	Trend	Plunge	Strike	Dip
<b>BSSO</b>						
3	1.7	0	0	0	0	0
2.6	2.1	0	0	0	0	258
3	3.4	0	0	0	0	0
8	3.7	0	0	0	0	0
6	3.8	-14.3	256	54	0	0
11	3.5	0	0	0	0	0
Halfspace	4.2	0	0	0	0	0
<b>CIGN</b>						
2	1.8	0	0	0	0	0
3	2	0	0	0	0	84
1.5	3.2	0	0	0	0	262
5	3.3	0	0	0	0	0
7	3.5	-8.2	191	32	0	0
15	3.6	0	0	0	0	0
Halfspace	4.2	0	0	0	0	0
<b>FRES</b>						
1.6	1.5	0	0	0	0	0
1	3.1	0	0	0	0	0
5	3.8	0	0	0	0	0
4	3.6	0	0	0	0	0
8	3.4	0	0	0	0	0
Halfspace	4.4	0	0	0	0	0
<b>MOCO</b>						
3	1.5	0	0	0	0	0
3.7	2.1	0	0	0	0	146
4.5	3.2	0	0	0	0	355
5	3.5	0	0	0	0	0
9	3.3	-13.7	71	22	0	0
11.6	3.6	0	0	0	0	0
Halfspace	4.2	0	0	0	0	0
<b>MRB1</b>						
1.3	1.3	0	0	0	0	0
2	2.5	0	0	0	0	0
6.6	3.1	0	0	0	0	0
7	3.8	0	0	0	0	0
9	3.8	0	0	0	0	0
10	3.9	0	0	0	0	0
9	3.8	0	0	0	0	0
Halfspace	4.1	0	0	0	0	0
<b>MSAG</b>						
1.5	3	0	0	0	0	0
700	3.7	-13	166	29	0	0
1	2.9	0	0	0	0	0
7	3.9	0	0	0	0	0
9	3.7	-10.2	231	62	0	0
9.7	3.4	0	0	0	0	0
Halfspace	4.4	0	0	0	0	0
<b>PSB1</b>						
1.2	1.4	0	0	0	0	0
3	2.4	0	0	0	0	21
2.8	3.1	0	0	0	0	273
7	3.3	0	0	0	0	0
5	3.7	-13.6	45	63	0	0
8.4	3.4	0	0	0	0	0
Halfspace	4.4	0	0	0	0	0

Thick (km)	Vs km/s	Aniso %	Trend	Plunge	Strike	Dip	
<b>RNI2</b>							
900	1.9	0	0	0	0	0	0
4.7	2.1	0	0	0	0	47	29
5.8	3.4	0	0	0	0	206	27
3.7	3.2	0	0	0	0	0	0
4	3.7	0	0	0	0	0	0
9.8	3.5	-8.5	252	70	0	0	0
15	3.9	0	0	0	0	0	0
Halfspace	4.3	0	0	0	0	0	0
<b>SACR</b>							
4	2.3	0	0	0	0	0	0
7	3.4	0	0	0	0	-5	34
5.5	3.4	0	0	0	0	0	0
7	3.7	-15	233	58	0	0	0
6.6	3.8	0	0	0	0	0	0
halfspace	4.4	0	0	0	0	0	0
<b>SGG</b>							
1.5	1.7	0	0	0	0	0	0
4.7	2.4	0	0	0	0	220	22
7.6	3.4	0	0	0	0	12	8
7	3.4	0	0	0	0	0	0
9.5	3.6	-10.7	206	22	0	0	0
9.8	3.9	0	0	0	0	0	0
Halfspace	4.2	0	0	0	0	0	0
<b>SGRT</b>							
1.6	3	0	0	0	0	0	0
3	3.6	0	0	0	0	315	22
3.3	3.2	0	0	0	0	23	17
5.6	3.6	0	0	0	0	0	0
6	3.5	-7.8	124	65	0	0	0
8	3.8	0	0	0	0	0	0
Halfspace	4.3	0	0	0	0	0	0
<b>SNAL</b>							
1.3	1.9	0	0	0	0	0	0
5	3.1	0	0	0	0	193	14
3.8	2.9	0	0	0	0	0	0
6.4	3.2	0	0	0	0	304	35
3.2	3.7	0	0	0	0	0	0
9.3	3.7	-11.1	206	23	0	0	0
9.5	3.7	0	0	0	0	0	0
Halfspace	4.1	0	0	0	0	0	0
<b>TRIV</b>							
1.2	1.5	0	0	0	0	0	0
1	3.2	0	0	0	0	0	0
9	3.5	0	0	0	0	0	0
8	3.8	0	0	0	0	0	0
8	3.9	0	0	0	0	0	0
Halfspace	4.4	0	0	0	0	0	0
<b>VAGA</b>							
4.8	1.8	0	0	0	0	0	0
3.5	2.1	0	0	0	0	10	19
7.7	3.2	0	0	0	0	192	17
5.5	3.6	0	0	0	0	0	0
9.2	3.4	-13.3	180	47	0	0	0
12.8	3.8	0	0	0	0	0	0
Halfspace	4.3	0	0	0	0	0	0



The 2009 L'Aquila (central Italy) earthquake rupture  
controlled by a high  $V_s$  barrier: a Receiver Function  
application

High-frequency receiver functions (RF) analyzed at two permanent broadband seismic stations operating in the epicentral area of the  $M_w$ 6.3, 2009 L'Aquila earthquake (central Italy) yield insight on crustal structure along the fault rupture. Harmonics analysis of RF highlights a strongly heterogeneous structure, for which we model the isotropic and anisotropic features using two recently developed Monte Carlo methods. The retrieved models display a common depth structure, between 10 and 40 km depth, consistent with the under-thrusting of the Adria lithosphere underneath the Apennines belt. Along the fault, in the uppermost crust, the S-wave velocity structure is laterally heterogeneous. Right above the hypocenter, we find a 4 – 6 km thick, very high S-wave velocity body ( $V_s$  as high as 4.2 km/s) that is absent in the SE portion of the fault, where the earthquake propagated. The high  $V_s$  body is coincident with the area of few aftershocks and is anti-correlated with the maximum slip patches of the earthquake, as modeled by DinSAR and strong motion data. We interpret this high  $V_s$  body as a barrier responsible for the strong localization of damages in the L'Aquila city and surroundings. Whatever the nature of this body, speculative since the exceptionality of such velocity for the upper crust, it played a role in controlling the rupture evolution during the L'Aquila earthquake.

## 5.1 Introduction

On April 6<sup>th</sup> 2009, a strong earthquake ( $M_w$ 6.3) shocked a densely populated region of the central Apennines, Italy, creating vast damage and loss of cultural sites. Although the central Apennines is a site of large destructive earthquakes (*Gruppo di lavoro CPTI*, 2004), the L'Aquila event ( Figure 5.1) developed on and poorly known fault, previously identified but thought to be a minor element in accommodating the active extension (*Boncio et al.*, 2004). Seismologic and geodetic data clearly show that the rupture originated on a blind, SW-dipping

normal fault (*Atzori et al.*, 2009; *Cheloni et al.*, 2009; *Chiarabba et al.*, 009a; *Scognamiglio et al.*, 2009). According to geodetic data, the amount of slip at the surface was small, while some evidence of surface breaks are found, mostly on top of the central portion of the fault (*Emergeo Working Group*, 2009).

Preliminary results from macroseismic surveys show that the damage was severe and concentrated in the L'Aquila city and in villages located on the hanging wall of the central portion of the fault. Strong motion records show high Peak Ground Acceleration (PGA) values at L'Aquila city and a very rapid increase of the energy release (*Ameri et al.*, 2009; *Çelebi et al.*, 2009). Aftershock locations clearly describe the geometry of the fault, but their distribution is not-homogeneous, with a large central portion of the fault where aftershocks are few or absent (Figure 5.1) (*Chiarabba et al.*, 009a). The rupture process highlights an initial slow phase, while the more energetic release occurred seconds later (*Cirella et al.*, 2009).

The presence of two permanent broad band stations, named AQU and FAGN, located in hanging wall of the fault, as in Figure 5.1, give us the opportunity to define a pseudo-3D  $V_s$  model of the fault with the high frequency Receiver Function (RF) (*Ammon*, 1991) analysis imaging S-wave velocity variations along the fault that are able to explain peculiarities in the rupture evolution and useful for source modeling. The main advantage of this technique is its direct dependence to the S-wave velocity, fundamental parameter for the kinematic, or dynamic, modeling of the seismic source (*Walters et al.*, 2009). The RF are time series that isolate the Ps converted phases generated by velocity contrasts present at depth (*Ammon*, 1991), separating the effects of the structure under the observation point from the source function and the near source velocity structure (*Langston*, 1979). The interpretation of the data-set allows us to discriminate the presence of dipping interfaces (*Lucente et al.*, 2005) and anisotropic layers at depth (i.e. *Levin & Park*, 1998; *Maupin & Park*, 2007; *Bianchi et al.*, 2008).

In this study, RF are obtained by using a 2Hz pass filter via *Di Bona* (1998) method and analyzed by an harmonic decomposition (*Farra & Vinnik*, 2000; *Girardin & Farra*, 1998) of the signal, separating the constant component from the first order harmonic. We inverted firstly the constant component using a stochastic method (*Piana Agostinetti & Malinverno*, 2009) with the aim of finding a 1D model, and later inverted the first harmonic using a Monte Carlo sampling technique (*Sambridge*, 1999) method, for the 3D velocity model.

## 5.2 Data & Method

We used teleseismic events from epicentral distances  $25^\circ$ - $105^\circ$  and Magnitude  $\geq 5.5$  recorded at AQU and FAGN stations. The AQU station (Figure 5.1) belongs to the Mediterranean Network (MedNET) and has been recording since February 1990. Remarkably enough, the station continued operating perfectly during the sequence, although located in the basement of the L'Aquila castle, which was severely damaged by the event; the station FAGN is located about 15 km to the SE of AQU and its recording period started on October 2004 (Figure

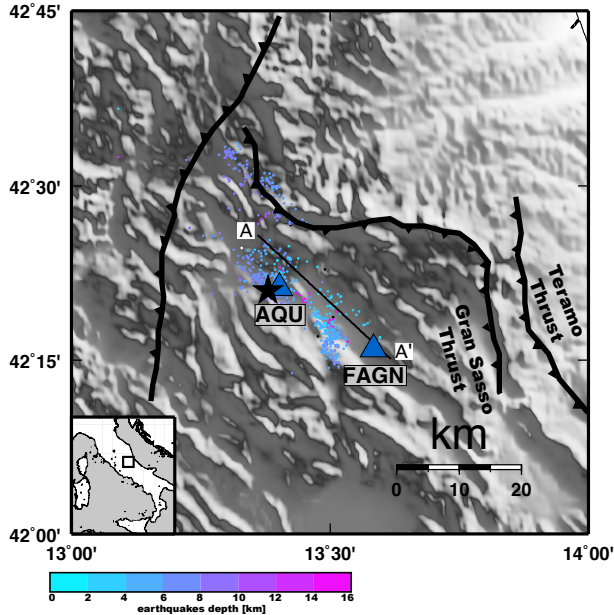


Figure 5.1: Map of the study area, blue triangles show the location of the stations, the black star represents the epicenter of the L'Aquila earthquake while dots are the aftershocks, colors refer to the depth. The line segment is the hypothesized superficial emergency of the seismogenic fault.

5.1).

The two stations yield a large data-set of very high quality RFs, 461 and 201 for AQU and FAGN respectively, that cover the whole backazimuthal directions (Figure 5.2). The RF data-sets were obtained by deconvolution of the vertical from the horizontal recordings into the radial, transverse, vertical (RTZ) coordinate system, where the radial (R) is computed along the great circle path between the epicenter and the station, positive away from the source, and the transverse (T) direction is calculated  $90^\circ$  clockwise from Radial. The deconvolution was performed in the frequency-domain following the approach proposed by *Di Bona* (1998). We applied a gaussian filter ( $\alpha=4$ ) to limit the frequency band below about 2Hz (*Langston*, 1979). The two data-sets are displayed in Figure 5.2 as backazimuthal sweeps of RFs binned over  $20^\circ$  of backazimuth angle and  $40^\circ$  epicentral distance centered at  $90^\circ$  of epicentral distance; with 50% overlapping area between adjacent bins. The good back-azimuthal coverage makes the 3D structure modeling beneath the two stations possible from both the radial RF (RRF) and transverse RF (TRF) data-set (Figure 5.2).

We introduced the harmonic angular stacking (*Girardin & Farra*, 1998) to isolate the isotropic structure from the 3D features. We compute the  $k=0$  harmonic (simple stacking) as the sum of all the RRF. The  $k=0$  harmonics

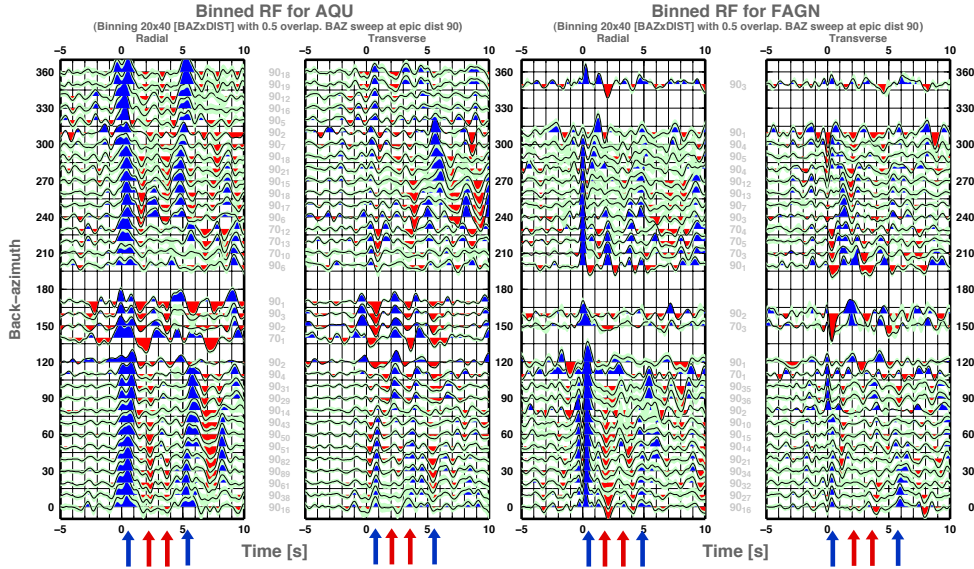


Figure 5.2: Data-set for AQU (left) and FAGN (right) as function of the back-azimuth and centered at epicentral distance of  $90^\circ$ . Arrows indicate the pulses described in the main text.

contain information about the isotropic structure underneath the station (Figure 5.3). We also calculated the  $k = 1$  harmonics, which can be used to reveal features with a periodicity equal to  $2\pi$ , such as Ps conversions generated from dipping interfaces or anisotropic layers with a dipping symmetry axis (*Bianchi et al.*, 2008). Both RRF and TRF are used to extract the  $k = 1$  harmonics, as they generally display a phase shift of  $\pi/2$  in back-azimuth, so that the summation of the  $k = 1$  harmonic of the two components enhances the periodic signal (*Shiomi & Park*, 2008).

The shear-velocity model beneath the two stations is investigated through a two-step procedure. First, the  $k = 0$  harmonics are used to extract the *a posteriori* probability density function of the  $V_s$  at depth following the approach developed in *Piana Agostinetti & Malinverno* (2009). In the second step, we used the recovered isotropic structure to address the search of the 3D features such as dipping interfaces or anisotropic layers, which give a satisfactory fit of the  $k = 1$  harmonics. The 3D model is retrieved using the Neighbourhood Algorithm search (*Sambridge*, 1999).

The RRF inverse problem roughly consists of giving inferences about the subsurface seismic structure using the RRF time-series as observed data. Such inferences can be given in different forms, e.g., a best-fitting seismic model or a probability distribution for some parameters at depth. Single model solution usually fails to catch the obvious non-uniqueness characteristic of the RRF inverse problem (*Ammon et al.*, 1990). Different techniques have been applied

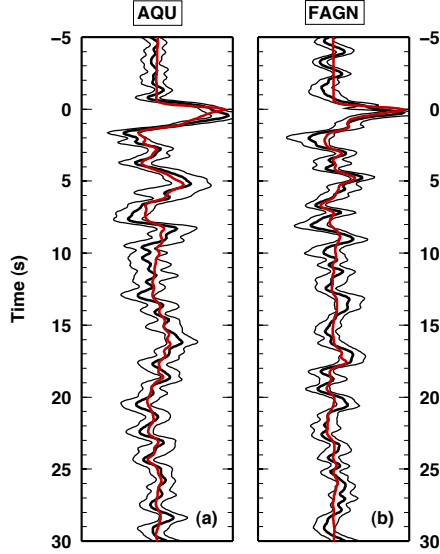


Figure 5.3: Results from the RjMCMC inversion. Black thick and thin lines show observed RF and  $\pm 2\sigma$  deviation. Red line plots the mean synthetic RF. (a) AQU data-set. (b) FAGN data-set.

to overcome this problem (e.g. *Lodge & Helffrich, 2009*). Here, we adopt a method recently developed by *Piana Agostinetti & Malinverno (2009)*, where a Reversible jump Markov chain Monte Carlo (RjMCMC) is used to sample the  $V_s$  parameter space and to retrieve the *a posteriori* probability density of the shear-velocity beneath a seismic station. The RjMCMC does allow to impose very loose *a priori* information, such that both the S-velocity and the number of seismic discontinuities at depth are considered as unknowns. A posteriori probability distribution (PPD) of the depth of the seismic interfaces beneath the station is computed. Such distribution broadly indicates how many isotropic layers compose the seismic structure beneath the station, and their most probable depths. The *a posteriori* probability distribution of the S-velocity at depth can be used to compute a mean  $V_s$  model and give a measure of the associated errors. We used the  $k = 0$  harmonics and the associated standard deviation, as observed data for the RjMCMC. Prior information about the seismic velocity structure are set as follow. The *a priori* probability distributions of the S-velocity and  $V_p/V_s$  is considered gaussian. For these normal distribution, mean and standard deviation ( $\sigma$ ) values are kept constant for the  $V_p/V_s$ , while they vary with depth for the  $V_s$  to account for large S-velocity variations expected in the shallow crust, where very different lithologies are present, e.g. sediments and carbonates. The number of interfaces can vary between 1 and 30, and the maximum is given by the resolution of the RF data-set. Between two interfaces,  $V_s$  can display a gradient, while  $V_p/V_s$  is constant. After a burn-in phase of

about 25000 models, which are discarded, the RjMCMC sampled about 175000 models from which we compute the posteriori probability distributions. We run 95 parallel RjMCMC on a linux cluster and obtain an ensemble of about  $16 \times 10^6$  models. The total CPU time is about 10 hours for each station.

The RjMCMC search gives out two main results: the PPD of the S-velocity at depth, and the distribution of the interface depth sampled during the chain. We used this information to build a parameter space for the following 3D  $V_s$  modeling, that uses additional information from TRF component. The mean  $V_s$  model from the RjMCMC search has been discretized with reference to the number and depth of the interfaces showed in the histograms of Figure 5.4. The  $V_s$  models have been divided into layers with uniform velocity, and 3D values have been given to perform the Neighbourhood Algorithm search following (*Sambridge, 1999*). This technique uses the properties of Voronoi cells to drive the search into a multidimensional parameter space, with the aim of finding an ensemble of models with acceptable data-fit. We generated 1000 initial random samples inside the parameter space, and the 4 cells with the lowest misfit are resampled to produce 20 new samples. This process was iterated for 500 times, for a total 11000 models explored for each station. The best fit model is interpreted as representative of the ensemble. Synthetics are calculated using the RAYSUM code (*Frederiksen & Bostock, 2000*) that models the propagation of a plane wave in dipping and anisotropic structures. Anisotropy is modeled as hexagonal with a unique axis of symmetry, since this is the most common fabric of rocks easily reproduceable (*Levin & Park, 1998*). P and S anisotropy parameters are set equal to reduce the non-uniqueness of the calculation. Dipping interfaces and anisotropic layers produce similar signals that can be hardly distinguished (*Savage, 1998; Bianchi et al., 2008*). Thus, we use dipping interfaces to reproduce 3D features in the very shallow crust, since a small dip of the discontinuity can be generated by the Apennines faults and bended structures (*Lucente et al., 2005, see also*). Conversely, we prefer to use anisotropic layers at greater depths, since high dipping, sharp structures are rare in the middle and lower crust (*Sherrington et al., 2004*).

## 5.3 Results

### 5.3.1 AQU

The AQU data-set shows the arrival of several phases in the first 5 s, generated by crustal heterogeneity (Figure 5.2). The first pulse in the radial gather is 1 s wide and has an amplitude as high as the direct P, with a clear southward move-out. The associated transverse signal is small, but displays a southward changing of a double phase polarity. The deeper features consist of two negative pulses centered at 2 and 3.5 s, associated with energy in the Transverse component. An extremely strong positive pulse at 5–5.5 s on the Radial gather is associated with a double pulse reversing at about  $180^\circ$  direction on the T component. The R and T RFs present comparable amplitudes, suggesting the presence of 3D features as dipping interfaces and anisotropic layers in the crust.

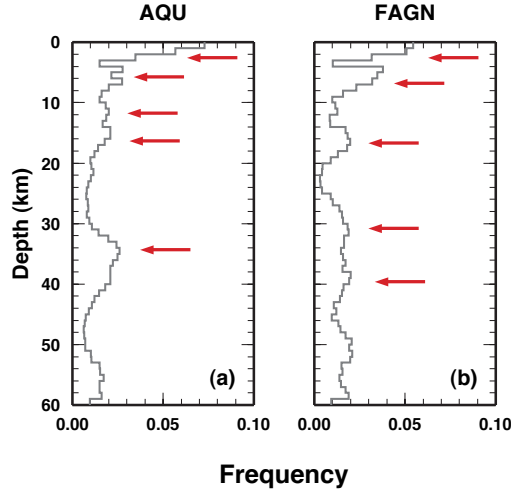


Figure 5.4: Results from the RjMCMC inversion. Histograms of the interface depth sampled during the Markov chain. (a) AQU data-set. (b) FAGN data-set.

In the velocity model recovered by the RjMCMC inversion, the  $V_s$  abruptly reaches very high values (more than 4 km/s) at depth shallower than 10 km (Figure 5.5). In the middle crust, a low  $V_s$  layer is present ( $V_s$  about 3.1 km/s). At greater depth, the  $V_s$  continuously grows up to mantle characteristic velocities reached at about 41 km depth. The observed and synthetic data are shown in Figure 5.3(a). The presence of the isotropic interfaces is highlighted by the histogram in Figure 5.4(a).

We identify at least two shallow discontinuities in the first 2 km depth, and other interfaces located at about 5, 11, 15, and 35 km depth. The 3D information visible in the  $k = 1$  data-set (Figure 5.6) led us to introduce more layers in the parameter space for the NA search, since four phases are localized in the first second, at 1.5 – 2.5 s and 3.5 – 5.5 s. The parameter space for AQU station is constructed grouping together the described information deduced from both the  $k = 0$  and  $k = 1$  data-sets: six isotropic discontinuities, two of which coincident with the anisotropic signal, and one additional anisotropic feature (at 3.5 s). Two further interfaces are added to reproduce the large Moho pulse observed at 5.5 s in the  $k = 0$  diagram (Figure 5.6) that suggest a layered structure for the lower crust. The parameter space has a total of 10 layers.

Figure 5.6 shows the best-fit model of the NA search, parameters of the best fit model are reported in Table 1.

In the upper crust (0 – 10 km depth), we find three features that consist of:

- a shallow, 1 km thick, low  $V_s$  layer ( $V_s = 1.5$  km/s), interpreted as sediments of the L'Aquila basin,

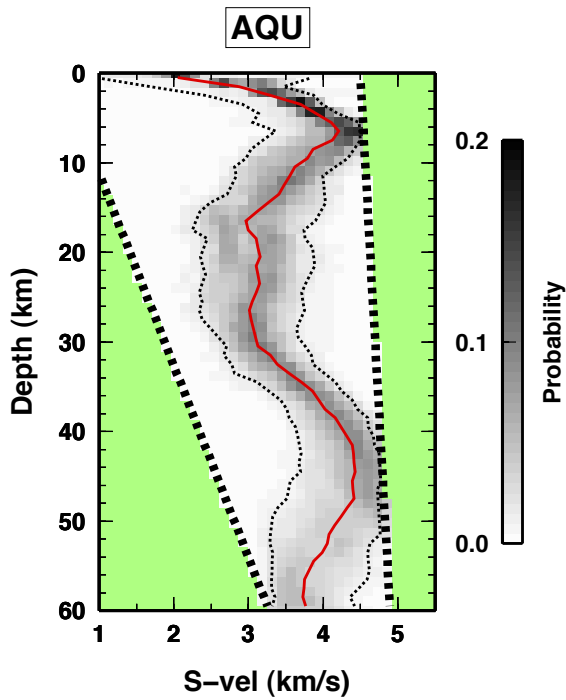


Figure 5.5: Results from the RjMCMC inversion, for AQU station. Posterior sampling of the  $V_s$  parameter at depth. Grey scale represents the posterior probability density at different depth levels for the S-velocity. Thick dotted lines indicate the boundaries of the parameter space for S-velocity parameter. The mean value of the  $V_s$  at each depth level is shown as a red line. Thin dotted lines is the  $\pm 2\sigma$  deviation for  $V_s$  parameter.

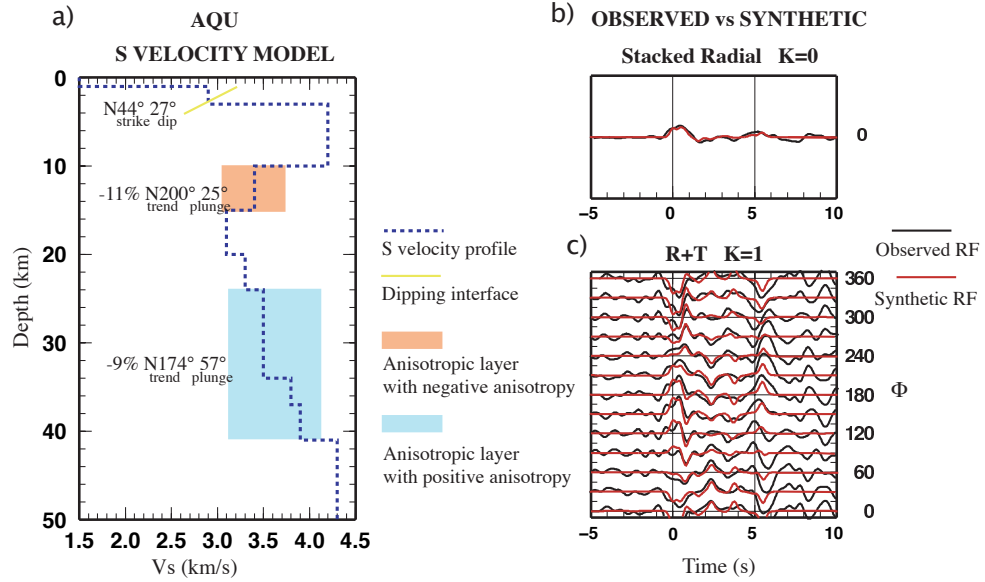


Figure 5.6: (a) S-Velocity model and observed (black lines) vs synthetic (red lines) RF for AQU station.

- a 2 km thick,  $V_s = 2.9$  km/s layer, interpreted as a layer of Meso-Cenozoic limestones.

- a 7 km thick, very high velocity layer ( $V_s$  reaching about 4.2 km/s) whose top is inclined towards SE. The nature of this layer is not easily explainable, because the overall thickness and velocities are excessive for carbonate or dolomitic rocks. We favor the hypothesis that a combination of dolomitic rocks and high speed basement, exhumed deep crust/mantle rocks, concur in forming this layer.

In the Middle crust, we find two main layers:

- a 5 km thick anisotropic layer with  $V_s = 3.4$  km/s and an anisotropy slow axis that trends N200°E and plunges 25°. We interpret this layer as due to limestone rocks.

- a 5 km thick low velocity layer ( $V_s$  about 3.1 km/s), probably weak material, where the thrusts take place.

In the lower crust, we find a unit that can be associated to the underthrusting Adria lithosphere:

- a layer at depth between 20 and 24 km, interpretable as limestone rocks ( $V_s=3.4$  km/s).

- a 17 km thick layered and anisotropic lower crust in which about 9% anisotropy is present with a symmetry axis trending N174°E of 57°. Velocities increase and reach mantle values at 41 km depth. We interpreted this feature as due to the Adria layered lower crust under-thrusting the belt.

Table 5.1: Velocities model for AQU as in Figure 5.6

Depth (km)	$V_s$ (km/s)	%P and S aniso	Trend	Plunge	Strike	Dip
1	1.5					
3	2.9					
10	4.2				44	27
15	3.4	-11	200	25		
20	3.1					
24	3.3					
34	3.5	9	174	57		
37	3.8	9	174	57		
41	3.9	9	174	57		
Halfspace	4.3					

### 5.3.2 FAGN

In the FAGN data-set, the first pulse is very sharp and picked at about 0.5 s, displaying a moveout with maximum delay time towards NE (Figure 5.2). The deeper feature consist of two negative pulses at 2 and 3.5 s and a positive pulse at 5 s on the R gather, while the T gather shows, in the first 0.5 s, a phase reversing at NE direction, some energy clustered around 2 s reversing towards South, and a double pulse reversing on S direction and located at 3.5 and 5.5 s (Figure 5.2). The R and T RFs present comparable amplitudes highlighting the presence of strong 3D features as dipping interfaces and anisotropic layers inside the crust. In the shallow structure recovered by the RjMCMC inversion (Figure 5.7), the  $V_s$  values slightly increase keeping average shallow crust values. At about 15 km depth a low  $V_s$  layer ( $V_s$  of about 3.0 km/s) is found. At greater depth, FAGN shows a slight and constant increase up to mantle velocities, reached at about 40 km depth. The observed and synthetic data-sets are shown in Figure 5.3(b).

We parameterize the model for the NA search including both isotropic interfaces located at about 2, 6, 10, 16, 30, 40 km depth (Figure 5.4(b)), and the 3D features used to model the signals at 0.5 s 1.5 – 2 s and 3.5 – 5.5 s, visible in the  $k = 1$  gather. The recovered S-velocity model (Figure 5.8) is the best-fit model of the search, and its parameters are resumed in Table 2.

The upper crust (0 – 8 km depth) consists of:

- a slow  $V_s$  (1.7 km/s) shallow layer of sediments,
- an inclined interface striking N334° and plunging 20°,
- two layers with relatively high  $V_s$  velocity ( $V_s < 3.7$  km/s), interpreted as limestone and dolomitic rocks of the Meso-Cenozoic cover.

Underneath FAGN,  $V_s$  as high as 4.1 km/s are not found, the higher values being 3.7 km/s.

The middle crust is composed by two layers that are comparable with those modeled at station AQU.

- a high  $V_s$  (3.6 km/s), 5 km thick, anisotropic layer, with –13% P and S anisotropy which symmetry axis trends N207°, with 46° plunge, interpretable

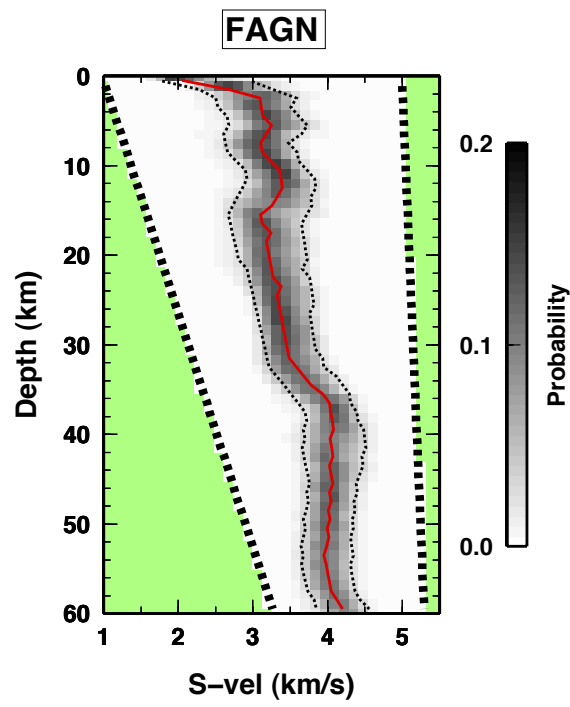


Figure 5.7: Results from the RjMCMC inversion. Same as in Figure 5.5, but for FAGN station.

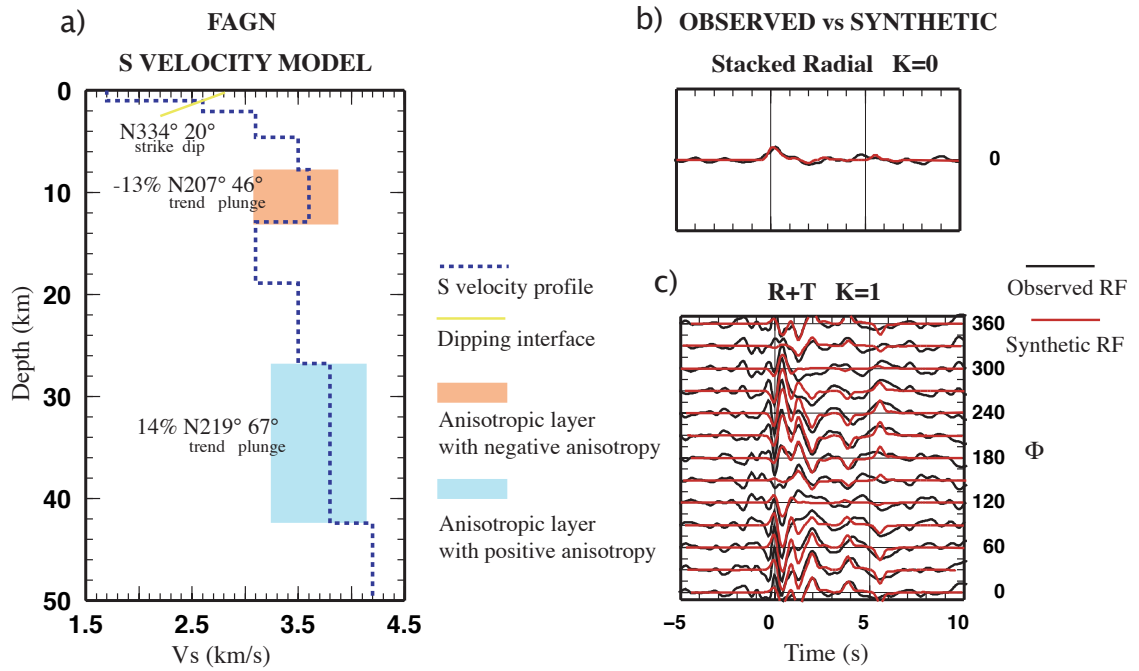


Figure 5.8: (a) S-Velocity model and observed (black lines) vs synthetic (red lines) RF for FAGN station.

Table 5.2: Velocities model for FAGN as in Figure 5.8

Depth (km)	$V_s$ (km/s)	%P and S aniso	Trend	Plunge	Strike	Dip
1	1.7					
2	2.6				334	20
5	3.1					
8	3.5					
13	3.6	-13	207	46		
19	3.1					
27	3.5					
42	3.8	14	219	67		
Halfspace	4.2					

as limestone and dolomitic rocks.

- a slow  $V_s$  (3.0 km/s), 6 km thick, layer, which bottom is at about 18 km depth, probably weak material, base of the thrusts.

In the lower crust, the deep unit associated with the under-thrusting Adria has two main features:

- a relatively high  $V_s$  (3.5 km/s), 8 km thick, isotropic layer down to 26 km depth,

- an anisotropic 16 km thick layer that lays above a Moho modeled at 42 km depth. It shows strong anisotropy (14%  $\Delta V_s$ ), with a fast symmetry axis oriented N219° plunging 67°. The S-wave velocity is equal to 3.8 km/s and does not show jumps, such as those found in station AQU. We interpret this layer as the lower crust of Adria.

## 5.4 Discussions

The geology and structure of central Apennines were intensively studied with surface data (*Galli et al.*, 2002) and, to some extent, by seismic explorations (*Mostardini & Merlini*, 1986; *Scisciani & Montefalcone*, 2006; *Patacca et al.*, 2008). Anyway, the deep structure and the overall architecture of the belt is still a matter of debate. The central Apennines has the higher elevation of the entire belt and displays a great difference between the regional divide and the culmination of topography, suggesting a dynamic support to the topography (*D'Agostino & Mckenzie*, 2000). Tomographic images reveal a large area in the lower crust and uppermost mantle with very low P-wave velocities (*Di Stefano et al.*, 2009; *Chiarabba et al.*, 2009b), interpreted as a window of the Apennines slab. Recent RFs studies, computed with mostly temporary, short-lived seismic stations (*Mele et al.*, 2006; *Di Bona et al.*, 2008; *Di Luzio et al.*, 2008), commonly identify the presence of a thick crust (more than 40 km), but results leave open quite different interpretations and geodynamic models. All previous RF studies modeled only the simple 1D structure, neglecting all the energy present in the T component and the clear move-out of converted pulses observable in the R

component (see Figure 5.2). In this study, we have analyzed the most complete data set for AQU and FAGN stations, almost 20 and 5 years of data, modeling the complete 3D structure with a good fit of both R and T components. The simultaneous modeling of 1D and 3D features is a key to obtain reliable features in complex areas, while neglecting 3D features may lead to local minima of the solution (*Bianchi et al.*, 2008). The 3D models for the two close stations reveal strong difference for the shallow crust, whereas deep features are similar. The difference of the AQU and FAGN models in the upper crust implies that the emplaced Apenninic wedge, thrust over the west-dipping Adria lithosphere, is strongly heterogeneous.

#### **5.4.1 Regional structure of the crust**

The similarity in the deeper part of the  $V_s$  models indicates a common regional structure, upon which the thrust nappes developed. For both stations, the structure of the eastward thrusts and the underlying Adria lithosphere is consistent and well defined. The deep unit (ADRIA in Figure 5.9) has a total crust thickness of about 20 – 25 km that agrees with the crust thickness observed at stations OFFI, FRES and TRTR, located in the external area, before the flexing of Adria (*Piana Agostinetti & Amato*, 2009). On top of the under-thrusting Adria, probably two thrust units forming the Apenninic wedge were stacked, involving both the limestone Meso-Cenozoic cover and part of the underlying basement. The shallowest thrust is reasonably coincident with the Gran Sasso structure (Figure 5.1), while the deeper can be associated to the Teramo thrust (*Bigi et al.*, 1999); the rocks outcropping are those of the sedimentary cover, while the eventually involved basement rocks remain buried and not visible in the field. The decollement levels are tentatively located between the anisotropic shallow layer and the negative  $V_s$  gradients between approximately 10 and 18 km depth, suggestive of weak materials or fluid filled zone, and the location of the intense thrusting (*Chiarabba et al.*, 2009b) (Figure 5.9). The SSW-dipping observed anisotropy, agrees with the geometry of the thrust and fold Apennines belt, where the deformations are caused by cracks and micro-cracks (*Kaneshima et al.*, 1988) formed during the emplacement of the thrust unit.

#### **5.4.2 Seismogenetic layer**

The upper structure recovered for the two stations is considerably different, suggesting that the units emplaced in thrusts have strong lateral variations caused by either the complex geometry of the thrust system or lateral variations of the Pre-Mesozoic basement. Underneath AQU,  $V_s$  abruptly reach very high values ( $V_s > 4$  km/s, Figure 5.6) while the  $V_s$  values at FAGN are smaller and within limits usually observed for carbonate rocks (Figure 5.8).

The presence of this extremely localized and laterally discontinuous high  $V_s$  body in the upper crust may have significantly influenced the generation and propagation of the 2009 L'Aquila earthquake rupture. The body is in fact located along the fault, surrounded by the maximum slip patches observed in (*Cirella et al.*, 2009). In Figure 5.10, we compare the location of the high  $V_s$  body

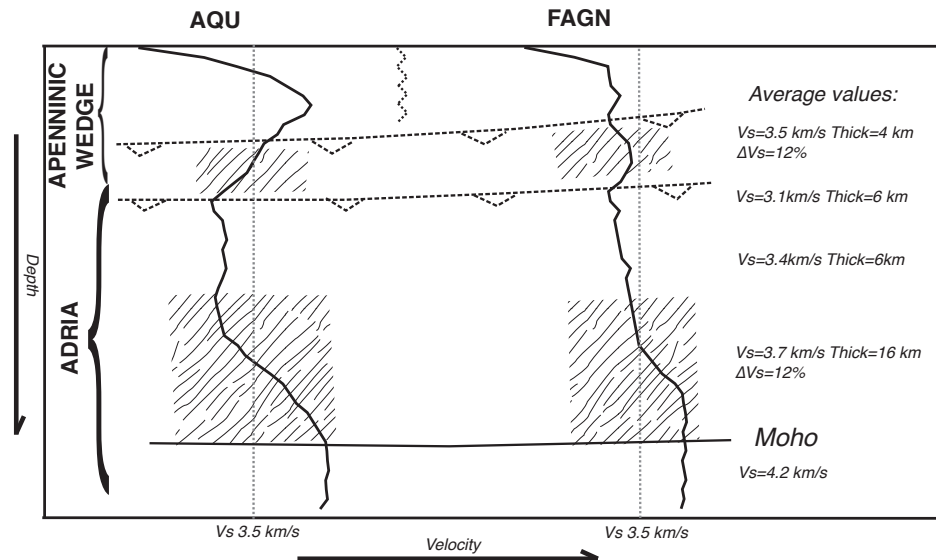


Figure 5.9: Correlation of the common features of the models obtained for AQU and FAGN. The lined boxes represent the anisotropic portions of the crust, as recovered by the 3D inversions. The shallow anisotropic layer delineates the bottom of the Apenninic wedge speculatively bounded by the two main thrust of the area. On the right the average values for Vs and anisotropy percent coming from the 3D models are shown.

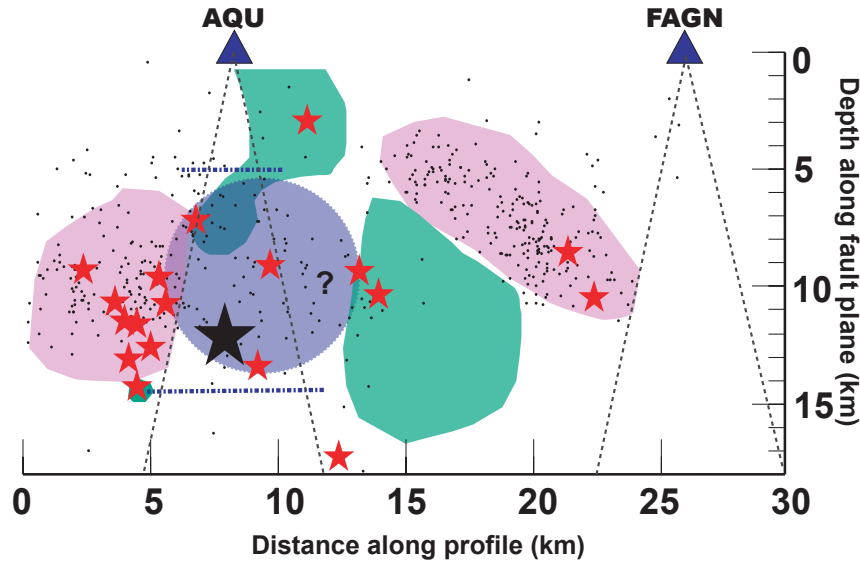


Figure 5.10: Fault plane showing the location of the  $V_s$  barrier (violet area), the maximum slip patches (green area, as retrieved in (Cirella *et al.*, 2009)) and the compliant area (pink area, from the aftershocks distribution located by (Chiarabba *et al.*, 009a)). Black star is the main shock, red stars are the  $M > 4$  aftershocks, black dots are the smaller aftershocks, projected on the fault plane. Triangles represent the projection of the seismic station on the fault trace, and the dotted grey lines delimitate their illumination area. Dotted blue lines represent the top and the bottom of the high  $V_s$  body detected under AQU station.

with the slip on the fault plane, which emersion is line AA' in Figure 5.1, and the aftershocks occurred during the first two months (Chiarabba *et al.*, 009a). The mainshock rupture started at the base of the high  $V_s$  body and propagated through the body. We computed synthetic tests trying to model the conversion as due to a thin high  $V_s$  layer coincident with the fault (high strength material that clogs the fault), finding patterns on the R and T components different from those observed. Although the resolution of teleseismic waveforms is somehow limited, hundreds to thousands of meters, we hypothesize that the high  $V_s$  material is present in both sides of the fault.

The mainshock signal during the first seconds, as observed by both close and distant stations (Chiarabba *et al.*, 009a), is emergent. After about 1 second, the high energy pulse occurred, suggesting a rapid acceleration of the rupture. The high frequency irradiation of the source was short, with respect to a  $M_w$  6.3 event, and very high peak ground acceleration are observed in L'Aquila (PGA  $\gg 0.35$  g) (Ameri *et al.*, 2009; Çelebi *et al.*, 2009). The initial slow rupture, which hypocenter is at about 10 km depth (Chiarabba *et al.*, 009a), probably

originated within the high  $V_s$  body. The lateral extent of this body to the south, presumably small since it is absent beneath the FAGN station, is anti-mirroring the area with the largest coseismic slip as modeled by DinSAR (*Atzori et al.*, 2009) and strong motion data (*Cirella et al.*, 2009). We interpret the high  $V_s$  body as a strong fault section acting as a high strength barrier (*Dunham et al.*, 2003), not slipping, during the event. The majority of aftershocks originated outside this high  $V_s$  zone, delineating the compliant region around the main asperity. Its localization may account for the repetition of similar earthquakes, in agreement with the similar damages observed by macroseismic studies for the 2009 and the 1461 earthquakes (*Gruppo di lavoro CPTI*, 2004). Finally, the very low  $V_s$  shallowest layer found underneath AQU and FAGN stations indicates that Quaternary sediments are very thick (around 1 km) beneath the Aquila basin and may account for the local amplification of ground motion during the earthquake.

## 5.5 Conclusions

We find an exceptionally high velocity body ( $V_s > 4.0$  km/s) along the fault ruptured during the 2009 L'Aquila earthquake. This body is laterally not continuous and its extent is anti-correlated with the area of maximum slip and rare aftershocks, as observed by geodetic and seismologic data. The nature of this body is speculative since such extreme velocities are consistent with deep crust or upper mantle rocks, while are over the limit of carbonate rocks ( $V_s < 3.7$  km/s). Independent geophysical data are required to fully assess which type of rocks forms the lower part of the thrust unit. Whatever the rock type, we interpret the high  $V_s$  as a strong portion of the fault with insignificant slip during the event. This high strength barrier concentrated energy and produced the strong pulse observed at the stations located around L'Aquila. The presence of such high velocities should be taken into account while modeling the kinematic or dynamic of the L'Aquila seismic source. Moreover its presence probably affected the displacement of the Gran Sasso thrust which is partially E-W oriented while the surrounding structures display the NW-SE Apenninic characteristic vergence. Future directions will be the analysis of RF from the temporary stations installed in the epicentral region to better confine the extent of the high  $V_s$  body.



## Acknowledgments

Vorrei ringraziare Francesco Pio Lucente, che ha seguito con me tutto il lavoro contenuto in questa tesi di Dottorato, che ha sempre saputo darmi buoni consigli grazie alle sue qualità sia umane che di ricercatore. Ringrazio Claudio Chiarabba che cinque anni fa mi ha introdotto nel mondo della Geofisica e Nicola Piana Agostinetti con cui ho lavorato spalla a spalla. Ringrazio Jeffrey Park che ha reso possibile il mio periodo di studio presso la Yale University, e Vadim Levin con cui abbiamo discusso in maniera produttiva i risultati di alcune osservazioni. Grazie alla pazienza che hanno avuto con me i miei diretti superiori all'INGV di Roma, Raffaele Di Stefano, Lucia Margheriti e Giulio Selvaggi, che sono stati comprensivi lasciandomi tutto il tempo necessario per dedicarmi al Dottorato di ricerca. Ringrazio tutti coloro che hanno condiviso come me, in modi differenti questi tre anni. I colleghi di corso del XXII cilo di Dottorato, Irene e Francesca per la loro presenza, Mario e Mauro che non sono mai stati avari della loro allegria, e tutti i ragazzi del Pollaio, con cui ho diviso le lunghe giornate di lavoro. Grazie ai miei genitori che mi supportano in tutte le scelte.

Chapter 2 of this Thesis has been published as: *Deep structure of the Colli Albani Volcanic District (central Italy) from Receiver Function analysis*. Bianchi, I., N. Piana Agostinetti, P. De Gori, C. Chiarabba. *Journal of Geophysical Research* doi:10.1029/2007JB005548.

Chapter 3 of this Thesis have been submitted to *Journal of Geophysical Research* as: *Mapping seismic anisotropy using harmonic decomposition of Receiver Functions: an application to Northern Apennines, Italy*. I. Bianchi, J. J. Park, N. Piana Agostinetti, V. Levin.

Chapter 5 of this Thesis has been submitted to *Journal of Geophysical Research* as: *The 2009 L'Aquila (central Italy) earthquake rupture controlled by a high Vs barrier: a Receiver Function application*. I. Bianchi, C. Chiarabba, N. Piana Agostinetti.



## BIBLIOGRAPHY

- Abt, D. L., Fischer, K. M., Abers, G. A., Strauch, W., Protti, J. M., & Gonzalez, V. Shear wave anisotropy beneath Nicaragua and Costa Rica: Implications for flow in the mantle wedge. *Geochem. Geophys. Geosyst.*, 10, Q05S15, 2009, doi:10.1029/2009GC002375.
- Amato, A., Alessandrini, B., Cimini, G. B., Frepoli, A., & Selvaggi, G. Active and remnant subducted slabs beneath Italy: evidence from seismic tomography and seismicity. *Ann. Geofis.*, 36, 2, 201–221, 1993.
- Amato, A., Chiarabba, C., Cocco, M., Bona, M. D., & Selvaggi, G. The 1989–1990 seismic swarm in the Alban Hills volcanic area, central Italy. *Journal of Volcanology and Geothermal Research*, 61, 3-4, 225–237, 1994.
- Amato, A. & Chiarabba, C. Recent uplift of the Alban Hill volcano (Italy): evidence for magmatic inflation? *Geophys. Res. Lett.*, 22, 15, 1985–1988, 1995.
- Amato, A. & Valensise, G. Il Basamento sedimentario dell'area albana: risultati di uno studio degli "ejecta" dei crateri idromagmatici di Albano e Nemi. *Mem. Soc. geol. It.*, 35, 761–767, 1986.
- Ameri, G., Mass, M., Bindi, D., D'Alema, E., Gorini, A., Luzi, L., Marzorati, S., Pacor, F., Paolucci, R., Puglia, R., & Smerzini, C. The 6 april 2009  $M_w$  6.3 aquila (central Italy) earthquake: Strong-motion Observations. *Seismol. Res. Lett.*, 80, 6, 951–966, 2009, doi:10.1785/gssrl.80.6.951.
- Ammon, C. The isolation of receiver effects from teleseismic  $p$  waveforms. *Bull. Seismol. Soc. Am.*, 81, 2504–2510, 1991.
- Ammon, C., Randall, G. E., & Zandt, G. On the non-uniqueness of receiver function inversions. *J. Geophys. Res.*, 95, 15303–15318, 1990.
- Argus, D., Gordon, R. G., Demets, C., & Stein, S. Closure of the Africa-Eurasia-North America Plate Motion Circuit and Tectonics of the Gloria Fault. *J. Geophys. Res.*, 94, B5, 55855602, 1989.

- Atzori, S., Hunstad, I., Chini, M., Salvi, S., Tolomei, C., Bignami, C., Stramondo, S., Trasatti, E., Antonioli, A., & Boschi, E. Finite fault inversion of DInSAR coseismic displacement of the 2009 L'Aquila earthquake (Central Italy). *Geophys. Res. Lett.*, 36, L15305, 2009, doi:10.1029/2009GL039293.
- Bannister, S., Reyners, M., Stuart, G., & Savage, M. Imaging the Hikurangi subduction zone, New Zealand, using teleseismic receiver functions: crustal fluids above the forearc mantle wedge. *Geophys. J. Int.*, 169, 2, 602–616, 2007.
- Bannister, S., Yu, J., Leitner, B., & Kennett, B. L. N. Variations in crustal structure across the transition from West to East Antarctica, Southern Victoria Land. *Geophys. J. Int.*, 155, 3, 870–880, 2004.
- Barchi, M. R., Minelli, G., & Pialli, G. The crop 03 profile: a synthesis of results on deep structures of the Northern Apennines. *Mem. Soc. Geol. It.*, 52, 383–400, 1998.
- Barchi, M. R., Pauselli, C., Chiarabba, C., Di Stefano, R., Federico, C., & Minelli, G. Crustal structure, tectonic evolution and seismogenesis in the Northern Apennines (Italy). *Boll. Geof. Teor. Appl.*, 0006-6729, 47, 249–270, 2006.
- Becker, T. W., Chevrot, S., Pelkum, V. S., & Blackman, D. K. Statistical properties of seismic anisotropy predicted by upper mantle geodynamic models. *Journal of Geophysical Research*, 167, 2, 943–957, 2006.
- Bianchi, I., Piana Agostinetti, N., De Gori, P., & Chiarabba, C. Deep structure of the Colli Albani volcanic district (central Italy) from receiver functions analysis. *J. Geophys. Res.*, 113, B09313, 2008, doi:10.1029/2007JB005548.
- Bigi, S., Calamita, F., Cello, G., Centamore, E., Deiana, G., Paltrinieri, W., Pietrantonio, P., & Ridolfi, M. Tectonics and Sedimentation within a Messinian foredeep in the Central Apennines, Italy. *J. Petr. Geol.*, 22, 1, 5–18, 1999.
- Blackman, D. K. & Kendall, J.-M. Seismic anisotropy in the upper mantle 2. predictions for current plate boundary flow models. *Geochem. Geophys. Geosyst.*, 4, 2002, doi:10.1029/2001GC000247.
- Boncio, P., Lavecchia, G., & Pace, B. Defining a model of 3D seismogenic sources for Seismic Hazard Assessment applications: The case of central Apennines (Italy). *J. Seismol.*, 8, 407–425, 2004.
- Burdick, L. J. & Langston, C. A. Modeling crustal structure through the use of converted phases in teleseismic body waveforms. *Bull. Seismol. Soc. Am.*, 67, 677–691, 1977.
- Cassinis, R., Scarascia, S., & Lozej, A. The deep crustal structure of Italy and surrounding areas from seismic refraction data. A new synthesis. *Boll. Soc. Geol. It.*, 122, 365–376, 2003.

- Çelebi, M., Bazzurro, P., Chiaraluce, L., Clemente, P., Decanini, L., Sortis, A. D., Ellsworth, W., Gorini, A., Kalkan, E., Marcucci, S., Milana, G., Molaioli, F., Olivieri, M., and A. Rovelli, D. R., Sabetta, F., & Stephens, C. Recorded Motions of the Mw 6.3 April 6, 2009 L'Aquila Earthquake and Implications for Building Structural Damage, Earthquake Spectra. *submitted*, 2009.
- Cheloni, D., D' Agostino, N., D' Anastasio, E., Avallone, A., Mantenuto, S., Giuliani, R., Mattone, M., Calcaterra, S., Gambino, P., Dominici, D., Radicioni, F., & Fastellini, F. Coseismic and initial postseismic slip of the 2009 Mw 6.3 L'Aquila earthquake, Italy from GPS measurement. *Geophys. J. Int.*, 2009.
- Chiarabba, C. & Amato, A. Upper crustal structure of the Benevento Area (southern Italy): fault heterogeneities and potential for large earthquakes. *Geophys. J. Int.*, 130, 229–239, 1997.
- Chiarabba, C., Amato, A., & Delaney, P. Crustal structure, evolution, and volcanic unrest of the Alban Hills, central Italy. *Bull. Volcanol.*, 59, 161–170, 1997.
- Chiarabba, C., De Gori, P., & Patané, D. The Mt. Etna plumbing system; the contribution of seismic tomography. in Bonaccorso, A., Calvari, S., Coltelli, M., Negro, C. D., & Falsaperla, S., editors, *Mt. Etna: Volcano Laboratory*, volume 143, pp. 191–204. American Geophysical Union, 2004.
- Chiarabba, C., De Gori, P., & Speranza, F. Deep geometry and rheology of an orogenic wedge developing above a continental subduction zone: Seismological evidence from the northern-central Apennines (Italy). *Lithosphere*, 1, 2, 95–104, 2009b.
- Chiarabba, C. et al. The 2009 L'Aquila (central Italy) Mw 6.3 earthquake: mainshock and aftershock. *Geoph. Res. Lett.*, 36, L18308, 2009a, doi:10.1029/2009GL039627.
- Chiarabba, C., Malagnini, L., & Amato, A. Three-Dimensional Velocity Structure and Earthquakes Relocation in the Alban Hills Volcano, Central Italy. *Bull. Seism. Soc. Am.*, 84, 2, 295–306, 1994.
- Christensen, N. Serpentinites, peridotites, and seismology. *Int. Geol. Rev.*, 46, 795–816, 2004.
- Christensen, N. I. & Mooney, W. D. Seismic velocity structure and composition of the continental crust: a global view. *J. Geophys. Res.*, 100, B7, 9761–9788, 1995.
- Cimini, G. B., Chiarabba, C., Amato, A., & Iyer, H. M. Large teleseismic P-wave residuals observed at the Alban Hills volcano, Central Italy. *Annali di Geofisica*, 37, 5, 969–988, 1994.

- Cirella, A., Pitanesi, A., Tinti, E., Scognamiglio, L., Michelini, A., Lomax, A., & Boschi, E. Rupture History of the 2009 L'Aquila earthquake from non-linear joint inversion of strong motion and GPS data. *Geophys. Res. Lett.*, 36, L19304, 2009, doi:10.1029/2009GL039795.
- Conticelli, S. & Peccerillo, A. Petrology and geochemistry of potassic and ultrapotassic volcanism in central Italy; petrogenesis and inferences on the evolution of the mantle sources. *Lithos*, 28, 3-6, 221-240, 1992.
- Crampin, S. Seismic wave propagation through a cracked solid: polarization as a possible dilatancy diagnostic. *LGophys. J. R. Astr. Soc.*, 53, 467-496, 1978.
- D' Agostino, N. & McKenzie, D. Convective support of long-wavelength topography in the Apennines. *Terra Nova*, 11, 234-238, 2000.
- De Luca, G., Cattaneo, M., Monachesi, G., & Amato, A. Seismicity in central and northern Apennines integrating the Italian national and regional networks. *Tectonophysics*, 2009, doi:10.1016/j.tecto.2008.11.032.
- De Rita, D., Faccenna, C., & Rosa, C. Stratigraphy and volcano tectonics. in Trigila, R., editor, *The Volcano of the Alban Hills: Roma.*, II, pp. 33-71. Tipografia, S.G.S., Rome, 1995.
- De Rita, D., Funicello, R., & Parotto, M. *Carta Geologica del Complesso Vulcanico dei Colli Albani (scala 1:50.000). Progetto Finalizzato Geodinamica.* CNR, Rome, 1988.
- Dewey, J. K., Helman, M. L., Hutton, D. H. W., & Knot, S. D. Kinematics of the western Mediterranean. *Geol. Soc. Sp. Pub.*, 45, 265-283, 1989.
- Di Bona, M. Variance estimate in frequency-domain deconvolution for teleseismic receiver function computation. *Geophys. J. Int.*, 134, 634-646, 1998.
- Di Bona, M., Lucente, F. P., & Piana Agostinetti, N. Crustal structure and Moho depth profile crossing the central Apennines (Italy) along the N°42 parallel. *J. Geophys. Res.*, 113, B12306, 2008, doi:10.1029/2008JB005625.
- Di Filippo, M. & Toro, B. Analisi gravimetrica delle strutture geologiche del Lazio Meridionale. Gravimetric analysis of the geologic structure of southern Latium. *Geologica Romana*, 19, 285-294, 1980.
- Di Luzio, E., Mele, G., Tiberti, M. M., & Cavinato, G. P. Moho deepening and shallow upper crustal delamination beneath the central Apennines. *Earth Planet. Sci. Lett.*, 2008, doi:10.1016/j.epsl.2008.09.018.
- Di Stefano, R., Kissling, E., Chiarabba, C., Amato, A., & Giardini, D. Shallow subduction beneath Italy: three-dimensional images of the Adriatic-European-Tyrrhenian lithosphere system based on high-quality P wave arrival times. *J. Geophys. Res.*, 2009, doi:10.1029/2008JB005641.

- Di Stefano, R., Kissling, E., Chiarabba, C., Bianchi, I., Ciaccio, M., & Carrara, M. Crustal thickness and 3d moho geometry in Italy: new constraints for geodynamics and tectonics, 2010, In Preparation.
- Doglioni, C. A proposal of kinematic modelling for W-dipping subductions possible applications to the Tyrrhenian-Apennines system. *Terra Nova*, 3, 423–434, 1991.
- Dueker, K. G. & Sheehan, A. F. Mantle discontinuity structure beneath the Colorado Rocky Mountains and High Plains. *J. Geophys. Res.*, 103, B4, 7153–7169, 1998.
- Dunham, E. M., Favreau, P., & Carlson, J. M. A Supershear Transition Mechanism of Cracks. *Science*, 299, 2003.
- Dziewonski, A. & Anderson, D. L. Preliminary Reference Earth Model (PREM). *Phys. Earth planet. Inter.*, 25, 297–356, 1981.
- Emergeo Working Group. Rilievi geologici di terreno effettuati nell'area epicentrale della sequenza sismica dell'Aquilano del 6 aprile 2009. <http://portale.ingv.it/primo-piano/archivio-primo-piano/notizie-2009/terremoto-6-aprile/>, 2009.
- Faccenna, C., Becker, T. W., Lucente, F. P., Jolivet, L., & Rossetti, F. History of subduction and back-arc extension in the Central Mediterranean. *Geoph. J. Int.*, 145, 809–820, 2001.
- Faccenna, C., Funiciello, R., & Mattei, M. Late Pleistocene N-S shear zones along the Latium Tyrrhenian margin; structural characters and volcanological implications. *Bollettino di Geofisica Teorica ed Applicata*, 36, 141–144, 507–522, 1994.
- Faccenna, C., Mattei, M., Funiciello, R., & Jolivet, L. Styles of back-arc extension in the Central Mediterranean. *Terra Nova*, 9, 3, 126–130, 1997.
- Faccenna, C., Piromallo, C., Crespo-Blanc, A., Jolivet, L., & Rossetti, F. Lateral slab deformation and the origin of the Western Mediterranean arcs. *Tectonics*, 23, doi:10.1029/2002TC001488, 2004.
- Farra, V. & Vinnik, L. Upper mantle stratification by P and S receiver functions. *Geophysical Journal International*, 141, 3, 699–712, 2000.
- Federico, L., Crispini, L., Scambelluri, M., & Capponi, G. Ophiolite melange zone records exhumation in a fossil subduction channel. *Geology*, 35, 499–502, 2007, doi: 10.1130/G23190A.1.
- Fellin, M. G., Reiners, P. W., Brandon, M. T., Wuthrich, E., Balestrieri, M. L., & Molli, G. Thermochronologic evidence for the exhumational history of the Alpi Apuane metamorphic core complex, northern Apennines, Italy. *Tectonics*, 26, TC6015, 2007, doi:10.1029/2006TC002085.

- Ferris, A., Abers, G. A., Christensen, D. H., & Veenstra, E. High resolution image of the subducted Pacific (?) plate beneath central Alaska. *Earth Planet. Sci. Lett.*, 214, 3-4, 575–588, 2003.
- Feuillet, N., Nostro, C., Chiarabba, C., & Cocco, M. Coupling between earthquakes swarms and volcanic unrest at the Alban Hills volcano (central Italy) modeled through elastic stress transfer. *J. Geophys. Res.*, 109, 2004.
- Fornaseri, M. Geochronology of volcanic rocks from Latium (Italy). *Rend. Soc. It. Miner. Petr.*, 40, 73–106, 1985.
- Fouch, M. J. & Rondenay, S. Seismic anisotropy beneath stable continental interiors. *Phys. Earth Planet. Inter.*, 158, 292320, 2006, doi:10.1016/j.pepi.2006.03.024.
- Franco, R. D., Ponziani, F., Biella, G., Boniolo, G., Caielli, G., Corsi, A., Maistrello, M., & Morrone, A. DSS-WAR experiment in support of the CROP-03 project. *Mem. Soc. Geo. It.*, 52, 67–90, 1998.
- Frederiksen, A. W. & Bostock, M. G. Modeling teleseismic waves in dipping anisotropic structures. *Geophys. J. Int.*, 141, 401–412, 2000.
- Frederiksen, A. W., Folsom, H., & Zandt, G. Neighbourhood inversion of teleseismic *ps* conversions for anisotropy and layer dip. *Geophys. J. Int.*, 155, 200–212, 2003.
- Frepoli, A. & Amato, A. Contemporaneous extension and compression in the northern apennines from earthquake fault-plane solutions. *Geophys. J. Int.*, 129, 1997.
- Funiciello, R. & Parotto, M. The sedimentary substratum in the Alban Hills region; geodynamic and paleogeographic considerations on the Tyrrhenian margin of the central Apennines. *Geologica Romana*, 17, 233–287, 1978.
- Galli, P., Galadini, F., M.Moro, & Giraudi, C. New paleoseismological data from the Gran Sasso d'Italia area (central Apennines). *Geophys. Res. Lett.*, 7, 2002.
- Giordano, G., Benedetti, A. A. D., Diana, A., Diano, G., Gaudioso, F., Marasco, F., Miceli, M., Mollo, S., Cas, R. A. F., & Funiciello, R. The Colli Albani mafic caldera (Roma, Italy): Stratigraphy, structure and petrology. *J. Vol. Geot. Res.*, 155, 49–80, 2006.
- Girardin, N. & Farra, V. Azimuthal anisotropy in the upper mantle from observation of P-to-S converted phases: application to southeast Australia. *Geophys. J. Int.*, 133, 615–629, 1998.
- Gogus, O. H. & Pysklywec, R. N. Mantle lithosphere delamination driving plateau uplift and synconvergent extension in eastern Anatolia. *Geology*, 36, 723–726, 2008.

- Gruppo di lavoro CPTI. Catalogo Parametrico dei Terremoti Italiani, INGV, Bologna. <http://emidius.mi.ingv.it/CPTI04/>, 2004.
- Gueguen, E., Doglioni, C., & Fernandez, M. On the post 25 Ma geodynamic evolution of the western Mediterranean. *Tectonophysics*, 298, 259–269, 1998.
- Improta, L., Iannaccone, G., Capuano, P., Zollo, A., & Scandone, P. Inferences on the upper crustal structure of Southern Apennines (Italy) from seismic refraction investigations and subsurface data. *Tectonophysics*, 317, 273–297, 2000.
- Jung, H. Deformation fabrics of olivine in Val Malenco peridotite found in Italy and implications for the seismic anisotropy in the upper mantle. *Lithos*, 109, 341–349, 2009.
- Kaneshima, S., Ando, M., & Kimura, S. Evidence from shear-waves splitting for the restriction of seismic anisotropy to the upper crust. *Nature*, 335, 627–629, 1988.
- Katayama, I. & Karato, S.-I. Effect of temperature on the B- to C-type olivine fabric transition and implication for flow pattern in subduction zones. *Phys. Earth Planet. Int.*, 157, 33–45, 2006.
- Kawakatsu, H. & Watada, S. Seismic evidence for deep-water transportation in the mantle. *Science*, 306, 1468, 2007.
- Kern, H. P and S-wave velocities in crustal and mantle rocks under the simultaneous action of high confining pressure and high temperature and the effect of the rock. in Schireyer, W., editor, *High-Pressure Research in Geoscience*, pp. 15–45. Schweizebart'sche Verlagsbuchhandlung, Stuttgart, 1982.
- Kneller, E. A., van Keken, P. E., Karato, S.-I., & Park, J. B-type fabric in the mantle wedge: Insights from high-resolution non-Newtonian subduction zone models. *Earth Planet. Sci. Letts.*, 237, 781–797, 2005.
- Langston, C. A. Structure under Mount Rainier, Washington, inferred from teleseismic body waves. *J. Geophys. Res.*, 84, B9, 4749–4762, 1979.
- Lees, J. M. The magma system of Mount St. Helens: Non linear high resolution P-wave tomography. *J. Volcanol. Geot. Res.*, 53, 103–116, 1992.
- Leidig, M. & Zandt, G. Modeling of highly anisotropic crust and application to the altiplano-puna volcanic complex of the central andes. *J. Geophys. Res.*, 108, 2003.
- Lentini, F. Le unita' sicilidi della valle d'agri (appennino lucano). *Geol. Romana*, 18, 1979.
- Levin, V., Droznin, D., Park, J., & Gordeev, E. Mantle wedge anisotropy beneath southeastern Kamchatka from local-S birefringence. *Geophys. J. Int.*, 158, 1009–1023, 2004.

- Levin, V., Margheriti, L., Park, J., & Amato, A. Anisotropic seismic structure of the lithosphere beneath the Adriatic coast of Italy constrained with mode-converted body waves. *Geophys. Res. Lett.*, pag. doi:10.1029/2002GL015438, 2002a.
- Levin, V. & Park, J. P-SH conversions in a flat-layered medium with anisotropy of arbitrary orientation. *Geophys. J. Int.*, 131, 2, 253–266, 1997.
- Levin, V. & Park, J. P-SH conversions in layered media with hexagonally symmetric anisotropy: a cookbook. *Pure appl. Geophys.*, 151, 2–4, 669–697, 1998.
- Levin, V. & Park, J. Seismic velocity structure beneath northern Tyrrhenian Sea constrained with mode-converted body waves. *submitted to Geophys. Res. Lett.*, 2009.
- Levin, V., Park, J., Brandon, M., Lees, J., Peyton, V., Gordeev, E., & Ozerovb, A. Crust and upper mantle of Kamchatka from teleseismic receiver functions. *Tectonophys.*, pp. 233–265, 2002b.
- Levin, V., Park, J., Lucente, F. P., Margheriti, L., & Pondrelli, S. End of subduction in Northern Apennines confirmed by observations of quasi-Love waves from the great 2004 Sumatra-Andaman earthquake. *Geophys Res. Lett.*, 34, L04304, 2007, doi:10.1029/2006GL028860.
- Levin, V., Roecker, S., Graham, P., & Hosseini, A. Seismic anisotropy indicators in Western Tibet: Shear wave splitting and receiver function analysis. *Tectonophysics*, 462, 99–108, 2008.
- Lodge, A. & Helffrich, G. Grid-search Inversion of Teleseismic Receiver Functions. *Geophys. J. Int.*, 178, 513–523, 2009.
- Long, M. D. & Silver, P. G. The subduction zone flow field from seismic anisotropy: A global view. *Science*, 319, 315–318, 2008.
- Lucente, F. P., Chiarabba, C., Cimini, G. B., & Giardini, D. Tomographic constraints on the geodynamic evolution of the Italian region. *J. Geophys. Res.*, 104, 20307–20327, 1999.
- Lucente, F. P., Piana Agostinetti, N., Moro, M., Selvaggi, G., & Di Bona, M. Possible fault plane in a seismic gap area of the Southern Apennines (Italy) revealed by receiver functions analysis. *J. Geophys. Res.*, 110, B4, 2005, 10.1029/2004JB003187.
- Malinverno, A. & Ryan, W. B. F. Extension in the Tyrrhenian sea and shortening in the Apennines as results of arc migration driven by sinking of the lithosphere. *Tectonics*, 5, 227–245, 1986.
- Margheriti, L., Pondrelli, S., Piccinini, D., Piana Agostinetti, N., Lucente, F. P., Amato, A., Baccheschi, P., Giovani, L., Salimbeni, S., Park, J., Brandon, M. T., Levin, V., Plomerova, J., Jedlicka, P., Vecsey, L., Babuska, V., Fiaschi,

- A., Carpani, B., & Ulbrich, P. RETREAT seismic deployment in the northern Apennines. *Annali di Geofisica*, 49, 4/5, 2006.
- Martinis, B. & Pavan, G. Note illustrative della carta geologica d'Italia, scala 1:100.000, foglio 157 Monte S. Angelo. *Servizio Geologico D'Italia*, 1967.
- Mattei, M., Funicello, R., Kissel, C., & Laj, C. Neogene tectonic evolution of the Central Apennines (Italy) revealed by paleomagnetic and magnetic fabric analysis. *Geophys. Res. Lett.*, 29, 24, doi:10.1029/2002GL015192, 1993.
- Maupin, V. & Park, J. Theory and observations: Wave propagation in anisotropic media. in Romanowicz, B. & Dziewonski, A., editors, *Treatise on Geophysics*, volume 1 of *Seismology and Structure of the Earth*, pp. 289–321. Elsevier, 2007.
- Mavko, G. M. Velocity and attenuation in partially molten rocks. *J. Geophys. Res.*, 85, 5173–5189, 1980.
- Meissner, R., Rabbal, W., & Kern, H. Seismic lamination and anisotropy of the Lower Continental Crust. *Tectonophysics*, 416, 81–99, 2006.
- Mele, G., Sandvol, E., & Cavinato, G. P. Evidence of crustal thickening beneath the central Apennines (Italy) from teleseismic receiver functions. *Earth Planet. Sci. Lett.*, 249, 425–435, 2006.
- Mercier, J.-P., Bostock, M. G., Audet, P., Gaherty, J. B., Garnero, E. J., & Revenaugh, J. The teleseismic signature of fossil subduction: Northwestern Canada. *J. Geophys. Res.*, 113, B04308, 2008, doi:10.1029/2007JB005127.
- Mori, J., Philips, D. E., & Harlow, D. Three dimensional velocity structure at Mount Pinatubo: Resolving magma bodies and earthquake hypocentres. in Newhall, C. G. & Punoungbayan, R. S., editors, *Fire and Mud, Eruptions and Lahars of Mount Pinatubo, Philippines*, pp. 371–382. Univ. of Washington Press, Seattle, 1996.
- Mostardini, E. & Merlini, S. Appennino centro-meridionale. Sezioni geologiche e proposta di modello strutturale. *Mem. Soc. Geol. It.*, 35, 177–202, 1986.
- Nakamichi, H., Tanaka, S., & Hamaguchi, H. Fine S wave velocity structure beneath Iwate volcano, northeastern Japan, as derived from receiver functions and travel times. *J. Volcanol. Geotherm. Res.*, 116, 235–255, 2002.
- Nicholson, T., Bostock, M., & Cassidy, J. F. New constraints on subduction zone structure in northern Cascadia. *Geophys. J. Int.*, 161, 3, 849–859, 2005.
- Nicolai, C. & Gambini, R. Structural architecture of the Adria platform-and-basin system. *Boll. Soc. Geol. It.*, SPECIALE 7, 21–37, 2007.
- Nikulin, A., Levin, V., & Park, J. Receiver function study of the Cascadia megathrust: evidence for localized serpentinization. *Geochem., Geophys., Geosys.*, 10, Q07004, 2009, doi:10.1029/2009GC002376.

- O'Connell, R. J. & Budiansky, B. Viscoelastic properties of fluid-saturated cracked solids. *J. Geophys. Res.*, 82, 5719-5736, 1977.
- Okubo, P. G., Benz, H. M., & Chouet. Imaging the crustal magma sources beneath Mauna Loa and Kilauea volcanoes, Hawaii. *Geology*, 25, 867-870, 1997.
- Ozacar, A. A. & Zandt, G. Crustal seismic anisotropy in central Tibet: Implication for deformational style and flow in the crust. *Geophys. Res. Lett.*, 41, 2004.
- Park, J. J. & Levin, V. Receiver functions from multiple-taper spectral correlation estimates. *Bull. Seismo. Soc. Amer.*, 90, 1507-1520, 2000.
- Park, J. J., Yuan, H., & Levin, V. Subduction zone anisotropy beneath Corvallis, Oregon: A serpentinite skid mark of trench-parallel terrane migration? *J. Geophys. Res.*, 109, B10306, 2004, doi:10.1029/2003JB002718.
- Patacca, E. & Scandone, P. Post-tortonian mountain building in the apennines. the role of the passive sinking of a relic lithospheric slab. in *The lithosphere in Italy. Advances in Earth Science Research. IT.NAT.COMM.INT.LITH.PROGR., MID-TERM CONF. (ROME, 5-6 MAY 1987), ATTI CONV.LINCEI*, volume 80, pp. 157-176, 1989.
- Patacca, E., Scandone, P., Di Luzio, E., Cavinato, G. P., & Parotto, M. Structural architecture of the central Apennines: interpretation of the CROP 11 seismic profile from the Adriatic coast to the orographic divide. *Tectonics*, 27, TC3006, 2008, doi:10.1029/2005TC001917.
- Pauselli, C., Barchi, M.-R., Federico, C., Magnani, M. B., & Minelli, G. The crustal structure of the Northern Apennines (central Italy): an insight by the CROP03 seismic line. *Am. J. Sci.*, 306, 428-450, 2006.
- Pauselli, C. & Federico, C. The brittle/ductile transition along the crop03 seismic profile: relationship with the geological feature. *Boll. Soc. Geol. It.*, Spec. 1, 25-35, 2002.
- Peyton, V., Levin, V., Park, J., Brandon, M. T., Lees, J., Gordeev, E., & Ozerov, A. Mantle flow at a slab edge: Seismic anisotropy in the Kamchatka region. *Geophys. Res. Lett.*, 28, 379-382, 2001.
- Pialli, G., Barchi, M., & Minelli, G. Results of the CROP 03 deep seismic reflection profile. *Mem. Soc. Geol. It.*, 52, 647, 1998.
- Piana Agostinetti, N. & Amato, A. Moho depth and  $v_p/v_s$  ratio in peninsular Italy from teleseismic receiver functions. *J. Geophys. Res.*, 114, B06303, 2009, doi:10.1029/2008JB005899.
- Piana Agostinetti, N., Levin, V., & Park, J. Crustal structure above a retreating trench: receiver function study of the northern Apennines orogen. *Earth Planet. Sci. Lett.*, 275, 3-4, 211-220, 2008a, doi:10.1016/j.epsl.2008.06.022.

- Piana Agostinetti, N., Lucente, F. P., Selvaggi, G., & Di Bona, M. Crustal structure and Moho geometry beneath the Northern Apennines (Italy). *Geophys. Res. Lett.*, 29, 20, doi:10.1029/2002GL015109, 2002.
- Piana Agostinetti, N. & Malinverno, A. Receiver Function inversion by trans-dimensional Monte Carlo sampling. *Geophys. J. Int.*, 2009, submitted.
- Piana Agostinetti, N., Park, J. J., & Lucente, F. P. Mantle wedge anisotropy in Southern Tyrrhenian subduction zone (Italy), from receiver function analysis. *Tectonophysics*, 462, 1-4, 35-48, 2008c, doi:10.1016/j.tecto.2008.03.020.
- Piana Agostinetti, N., Steckler, M., & Lucente, F. P. Imaging the subducted slab under the Calabrian Arc, Italy, from receiver function analysis. *Lithosphere*, 1, 3, 131-138, 2009, doi:10.1130/L49.1.
- Picotti, V. & Pazzaglia, F. J. A new active tectonic model for the construction of the Northern Apennines mountain front near Bologna (Italy). *J. Geophys. Res.*, 113, B08412, 2008, doi:10.1029/2007JB005307.
- Pinero-Feliciangelia, L. T. & Kendall, J.-M. Sub-slab mantle flow parallel to the Caribbean plate boundaries: Inferences from SKS splitting. *Tectonophysics*, 462, 22-34, 2008, doi:10.1016/j.tecto.2008.01.022.
- Plomerova, J., Margheriti, L., Park, J., Babuska, V., Pondrelli, S., Vecsey, L., Piccinini, D., Levin, V., Baccheschi, P., & Salimbeni, S. Seismic anisotropy beneath the Northern Apennines (Italy): Mantle flow or lithosphere fabric? *Earth Planet. Sci. Lett.*, 247, 157-170, 2006.
- Ponziani, F., Franco, R. D., Minelli, G., Biella, G., Federico, C., & Piali, G. Crustal shortening and duplication of the Moho in the Northern Apennines: a view from seismic refraction data. *Tectonophysics*, 252, 391-418., 1995.
- Quattrocchi, F. & Calcara, M. Emanazioni gassose nell'area di Ciampino (2/11/95) ed evento sismico nei Colli Albani (3/11/95). Relazione d'intervento, Ist. Naz. Geof., 1995, Gruppo geochimica fluidi.
- Rabbal, W. & Mooney, W. D. Seismic anisotropy of the crystalline crust: What does it tell us? *Terra Nova*, 8, 16-21, 1996.
- Regenauer-Lieb, K., Weinberg, R. F., & Rosenbaum, G. The effect of energy feedbacks on continental strength. *Nature*, 6, 2006.
- Roselli, P., Lucente, F. P., & Piana Agostinetti, N. Crustal structure at colliding plates boundary from receiver functions analysis: A close look beneath the northern Apennines (Italy). *Geophys. Res. Lett.*, 35, L12304, 2008, doi:10.1029/2008GL034055.
- Roselli, P., Piana Agostinetti, N., & Braun, T. Shear-velocity and anisotropy structure of a retreating extensional forearc (Tuscany, Italy) from receiver functions inversion. *Geophys. J. Int.*, 2010.

- Royden, L. E., Patacca, E., & Scandone, P. Segmentation and configuration of subducted lithosphere in Italy: an important control on thrust-belt and foredeep-basin evolution. *Geology*, 15, 714–717, 1987.
- Salimbeni, S., Levin, V., Pondrelli, S., Margheriti, L., & Park, J. Distribution of seismic anisotropy beneath central Italy and geodynamic implications for Northern Apennines. in *AGU Fall Meeting 2009*, pp. DI13A–1673, 2009.
- Salimbeni, S., Pondrelli, S., Margheriti, L., Levin, V., Park, J., Plomerova, J., & Babuska, V. Abrupt change in mantle fabric across Northern Apennines detected using seismic anisotropy. *Geophys. Res. Lett.*, 34, L07308, doi:10.1029/2007GL029302, 2007.
- Salimbeni, S., Pondrelli, S., Margheriti, L., Park, J., & Levin, V. SKS splitting measurements beneath the Northern Apennines region: a case of oblique trench retreat. *Tectonophysics*, 462, 1-4, 68–82, 2008.
- Sambridge, M. Geophysical inversion with a neighbourhood algorithm – I. Searching a parameter space. *Geophys. J. Int.*, 138, 479–494, 1999.
- Sambridge, M. Geophysical inversion with a neighbourhood algorithm – II. appraising the ensemble. *Geophys. J. Int.*, 138, 727–746, 1999b.
- Sartori, R. The main results of ODP Leg 107 in the frame of Neogene to Recent geology of Perityrrhenian areas. in *Proceedings of the Ocean Drilling Program, Scientific Results*, volume 107, pp. 715–730, 1990.
- Sato, H., Sacks, I. S., & Murase, T. The use of laboratory velocity data for estimating temperature and partial melt fraction in the low-velocity zone: Comparison with heat flow and electrical conductivity studies. *J. Geophys. Res.*, 94, 5689–5704, 1989.
- Savage, M. Lower crustal anisotropy or dipping boundaries? Effects on receiver functions and a case of study in New Zealand. *J. Geophys. Res.*, 103, 15, 69–87, 1998.
- Savage, M. Seismic anisotropy and mantle deformation: what have we learned from shear wave splitting? *Rev. Geophys.*, 37, 165–206, 1999.
- Savage, M., Park, J., & Todd, H. Velocity and anisotropy structure at the Hikurangi subduction margin, New Zealand from receiver functions. *Geophys. J. Int.*, 168, 1034–1050, 2007.
- Scarascia, S. Crustal Structure in the Southern Apennines region from DSS data. in *Proc EGS-EGC Meeting, Leeds.*, 1982.
- Scisciani, V. & Montefalcone, R. Coexistence of thin- and thick-skinned tectonics: An example for the Central Apennines, Italy. *Geol. Soc. of Am. Special Paper*, 414, 33–54, 2006.

- Scognamiglio, L., Tinti, E., Michelini, A., Dreger, D., Cirella, A., Cocco, M., Mazza, S., & Pitanesi, A. Fast Determination of Moment Tensors and Rupture History: Application to the April 6th 2009, L'Aquila Earthquake. *submitted to Bull. Seismo. Soc. of Am.*, 2009.
- Selvaggi, G. & Amato, A. Subcrustal earthquakes in the Northern Apennines (Italy): evidence for a still active subduction? *Geoph. Res. Lett.*, 19, 2127–2130, 1992.
- Serpelloni, E., Anzidei, M., Baldi, P., Casula, G., & Galvani, A. Crustal velocity and strain-rate fields in Italy and surrounding regions: new results from the analysis of permanent and non-permanent GPS networks. *Geophys. J. Int.*, 161, 3, 861–880, 2005.
- Sherrington, H. F., Zandt, G., & Frederiksen, A. Crustal fabric in the Tibetan Plateau based on waveform inversion for seismic anisotropy parameters. *J. Geophys. Res.*, 109, B02312, 2004, doi:10.1029/2002JB002345.
- Shiomi, K. & Park, J. Structural features of the subducting slab beneath the Kii Peninsula, central Japan: Seismic evidence of slab segmentation, dehydration, and anisotropy. *J. Geophys. Res.*, 113, B10318, doi:10.1029/2007JB005535, 2008.
- Skemer, P., Katayama, I., & Karato, S.-I. Deformation fabrics of the Cima di Gagnone peridotite massif, Central Alps, Switzerland: Evidence of deformation at low temperatures in the presence of water. *Contrib. Mineral Petrol.*, 152, 43–51, 2006, doi 10.1007/s00410-006-0093-4.
- Steckler, M. S., Piana Agostinetti, N., Wilson, C. K., Roselli, P., Seeber, L., A. Amato, & Lerner Lam, A. Crustal structure in the southern apennines from teleseismic receiver functions. *Geology*, 36, 2, 155–158, 2008.
- Tibi, R., Wiens, D. A., & Yuan, X. Seismic evidence for widespread serpentinized forearc mantle along the Mariana convergence margin. *Geophys. Res. Lett.*, 35, L13303, 2008, doi:10.1029/2008GL034163.
- Tommasi, A., Tikoff, B., & Vauchez, A. Upper mantle tectonics: three-dimensional deformation, olivine crystallographic fabrics and seismic properties. *Earth Planet. Sci. Lett.*, 168, 173–186, 1999.
- Tonegawa, T., Hirahara, K., Shibutani, T., Iwamori, H., Kanamori, H., & Shiomi, K. Water flow to the mantle transition zone inferred from a receiver function image of the Pacific slab. *Earth Planet. Sci. Lett.*, 274, doi:10.1016/j.epsl.2008.07.046, 346–354, 2008.
- Toro, B. Residual gravity anomalies and deep structure in the volcanic region of northern Latium. *Geologica Romana*, 17, 35–44, 1978.
- Vinnik, L. P. Detection of waves converted from P to SV in the mantle. *Earth planet. Inter.*, 15, 39–45, 1977.

- Vinnik, L. P., Aleshin, I. M., Kiselev, S. G., Kosarev, G. L., & Makeyeva, L. I. Depth localized azimuthal anisotropy from SKS and P receiver functions; the Tien Shan. *Geophysical Journal International*, 169, 3, 1289–1299, 2007.
- Vinnik, L. P., Reigber, C., Aleshin, I. M., Kosarev, G. L., Kaban, M. K., Oreshin, S. I., & Roecker, S. W. Receiver function tomography of the central Tien Shan. *Earth Planet. Sci. Lett.*, 255, 1-2, 131–146, 2004.
- Walters, R. J., Elliott, J. R., D’Agostino, N., England, P. C., Hunstad, I., Jackson, J. A., Parsons, B., Phillips, R. J., & Roberts, G. The 2009 L’Aquila earthquake (central Italy): A source mechanism and implications for seismic hazard. *Geophys. Res. Lett.*, 36, 17, 2009.
- Warren, C. J., Beaumont, C., & Jamieson, R. A. Formation and exhumation of ultra-high-pressure rocks during continental collision: Role of detachment in the subduction channel. *Geochem. Geophys. Geosyst.*, 9, Q04019, 2008a, doi:10.1029/2007GC001839.
- Warren, C. J., Beaumont, C., & Jamieson, R. A. Modelling tectonic styles and ultra-high pressure (UHP) rock exhumation during the transition from oceanic subduction to continental collision. *Earth Planet. Sci. Letts.*, 267, 129–145, 2008b.
- Wilson, C. K., Jones, C. H., Molnar, P., Sheehan, A. F., & Boyd, O. S. Distributed deformation in the lower crust and upper mantle beneath a continental strike-slip fault zone: Marlborough fault system, South Island, New Zealand. *Geology*, 32, 837–84, 2004, doi: 10.1130/G20657.1.
- Wilson, C. K., Pazzaglia, F. J., & Anastasio, D. J. A fluvial record of active fault-propagation folding, Salsomaggiore anticline, northern Apennines, Italy. *J. Geophys. Res.*, 114, B08403, 2009, doi:10.1029/2008JB005984.